



Title	Polymerized Ionic Liquids : Relationship between Physical Properties and Chemical Structures
Author(s)	松本, 篤
Citation	大阪大学, 2017, 博士論文
Version Type	VoR
URL	<a href="https://doi.org/10.18910/61474">https://doi.org/10.18910/61474</a>
rights	
Note	

*The University of Osaka Institutional Knowledge Archive : OUKA*

<https://ir.library.osaka-u.ac.jp/>

The University of Osaka

Polymerized Ionic Liquids: Relationship between  
Physical Properties and Chemical Structures

A Doctoral Thesis

by

Atsushi Matsumoto

Submitted to the Graduate School of Science

Osaka University

February 2017

---

## Acknowledgements

---

Firstly, I would like to thank my adviser, Prof. Tadashi Inoue, for giving me the opportunity, guidance, and freedom to explore various fields in polymer science. I would also like to thank lecturer Osamu Urakawa, Assistant Prof. Takuya Katashima, and Prof. Toshiyuki Shikata (at Tokyo University of Agriculture and Technology) and Dr. Kenji Nakamura for their guidance and helpful discussions. I would like to thank the other Inoue group members for helpful discussions and share the precious times going on journeys, hanging out to drink, and so on. I would like to thank wonderful friends who helped me learn new and attractive topics and encouraged each other, especially Suzuka Matsumoto, Saki Matsumoto, Toshihiko Aiba, Yuta Maki.

I would also like to thank Prof. James Runt at Penn State for giving me the opportunity to study abroad and to learn the essentials of dielectric relaxation spectroscopy. I would also like to thank the other Runt group members for helpful discussions and support my life in the United States, especially Dr. Ciprian Iacob and Dr. Joshua Bartels. I would also like to acknowledge Assistant Prof. Joshua Sangoro at University of Tennessee for a use of dielectric apparatus. I want to thank Dr. Rohit Khanna for helping me live life outside of the lab in the U.S.

Chapters 3 and 4 were carried out in collaboration with Prof. James Runt group supported by the Osaka University Scholarship for Overseas Research Activities 2014. The results of dielectric relaxation spectroscopy and wide-angle X-ray scattering were provided. I would like to thank Dr. Satoshi Maji for small-angle X-ray scattering work. I would like to thank Professors Takahiro Sato and Ken Terao for helpful discussions over the whole chapters.

Finally, I would like to thank my family; my mother and father for supporting my life in Osaka and for believing in me far away from my hometown. I would also like to thank my

dearest wife, Miho for supporting my daily life without complaining. I want to thank my dearest daughter, Rio for giving me healing.

February 2017

---

Atsushi Matsumoto

---

# Table of Contents

---

## **CHAPTER 1 General Introduction**

- 1-1 Background
- 1-2 Historical Survey of Studies on Polymerized Ionic Liquids
  - 1-2-1 Ionic Conductivity
  - 1-2-2 Linear Viscoelasticity
- 1-3 Rheo-Optical Studies for Analysis of Polymer Dynamics
  - 1-3-1 Stress-Optical Rule (SOR)
  - 1-3-2 Modified Stress-Optical Rule (MSOR)
- 1-4 Scope of This Thesis
- 1-5 References

## **CHAPTER 2 Rheo-Optical Studies on Dynamics of Polymerized Ionic Liquids with Various Counter Anions**

- 2-1 Introduction
- 2-2 Experimental Methods
- 2-3 Results and Discussion
  - 2-3-1 Overview of Modulus and Strain-Optical Coefficient
  - 2-3-2 MSOR Analysis
  - 2-3-3 Viscoelastic Segment Size
  - 2-3-4 Molecular Origin of the L Component
- 2-4 Conclusion
- 2-5 References

## **CHAPTER 3 Counter Ion-Induced Ordered Structure of a Polymerized Ionic Liquid in Bulk**

- 3-1 Introduction
- 3-2 Experimental Methods
- 3-3 Results and Discussion
  - 3-3-1 Micrographs
  - 3-3-2 Thermal Characterization
  - 3-3-3 Birefringence and Extinction Angle
  - 3-3-4 X-ray Scattering
  - 3-3-5 Linear Viscoelasticity
  - 3-3-6 MSOR Analysis
- 3-4 Conclusion
- 3-5 References

## **CHAPTER 4 Ionic Transport Mechanism of Polymerized Ionic Liquids with a Correlation of Nanoscale Morphology**

- 4-1 Introduction
- 4-2 Experimental Methods
- 4-3 Results and Discussion
  - 4-3-1 Linear Viscoelastic Response
  - 4-3-2 Dielectric Response
  - 4-3-3 Comparison between  $\tau_m$  and  $\tau_{HN}$
  - 4-3-4 Ionic Conductivity
  - 4-3-5 Electrode Polarization Analysis
  - 4-3-6 Nanoscale Morphology
  - 4-3-7 Decoupling of Ionic Transport from Segmental Dynamics

4-4 Conclusion

4-5 References

## **CHAPTER 5 Viscoelastic Properties and Local Dynamics of Polyelectrolyte/Ionic Liquid Solutions**

5-1 Introduction

5-2 Experimental Methods

5-3 Results and Discussion

5-3-1 Thermal Characterization

5-3-2 Overview of Modulus and Strain-Optical Coefficient for TFSI-1

5-3-3 Overview of Modulus and Strain-Optical Coefficient for TFSI-50

5-3-4 Estimation of the Rouse Segment Size

5-3-5 Stress-Optical Coefficient for Polymer Component

5-3-6 Rouse Segment Size and Its Concentration Dependence

5-3-7 Local Motion of a Chain in Solution

5-3-8 Estimation of  $G_L^*$  and Its Molecular Origin

5-3-9 MSOR Analysis for TFSI-50

5-4 Conclusion

5-5 References

## **CHAPTER 6 Summary**

### **List of Publications**

---

# CHAPTER 1

## General Introduction

---

### 1-1 Background

Ionic liquids (ILs) are a diverse group of salts having a melting point below 100°C. Figure 1-1 shows the representative chemical structures of cations and anions which form ILs. The ions are larger than those in ordinary salts such as sodium chloride and the charges are well delocalized, resulting that melting points of ILs decrease due to the lower lattice energy to form ionic crystals. ILs have been attracting significant attention because of their highly advantageous properties such as low flammability, negligible vapor pressure, and high ionic conductivity.<sup>1-4</sup> These properties lead to many applications such as stable electrolytes and powerful solvents. A common shortcoming of ILs for electrolyte applications is a concern about leakage. Therefore, solidified ILs may be useful.

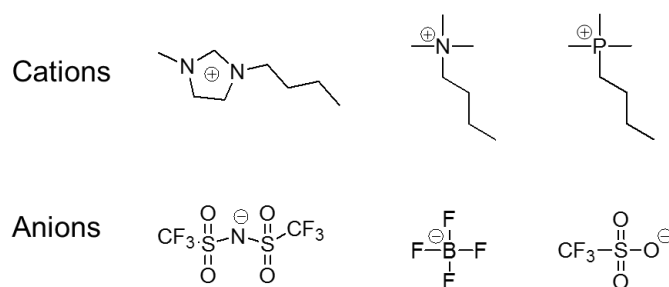


Figure 1-1. Chemical structures of the representative cations and anions.

Polymerized Ionic Liquids (PILs) have attracted research interests in the last two decades, and several reviews about PILs have recently been published.<sup>5-8</sup> PILs can be chemically described as polymers having constituents of ILs on their repeating units.<sup>9-12</sup> One of the advantages of PILs is that they show enhanced mechanical properties resulting from

polymerization. However, PILs inevitably sacrifice high ionic conductivity inherent in ILs because the mobility of either cations or anions is restricted by polymerization. Therefore, a number of research groups have attempted to clarify the relationship between chemical structure, morphology, and mechanical properties of PILs.<sup>11, 13-18</sup> These studies will enable us to design PILs having our desirable material properties.

## **1-2 Historical Survey of Studies on Polymerized Ionic Liquids**

### **1-2-1 Ionic Conductivity**

The relationship between morphology and ionic conductivity was studied by Long et al.<sup>13, 14</sup> with a use of PILs having different alkyl chain lengths substituted to side chains and having various counter anions. The glass transition temperature and ionic conductivity decrease with increasing ionic sizes of counter anions. They also reported that the backbone-to-backbone scattering peak in WAXS profile is related to ionic conductivities of PILs.

The decoupling between segmental motion (structural relaxation) and ionic conductivity (ion diffusion) is one of the characteristics of PILs.<sup>15</sup> Nakamura<sup>16</sup> and Colby<sup>17</sup> studied the dynamics of PILs having various counter anion species using viscoelastic and dielectric measurements. They showed the coupling between the ion pair motion (the lifetime of ion pair) and ionic conductivity. The Vogel-Fulcher-Tannann (VFT) type temperature dependence of ion pair motion and ionic conductivity changes into the Arrhenius type dependence below the glass transition temperature. In contrast, the temperature dependence of segmental motion follows the VFT equation. They also showed that the ion pair motion is faster than the segmental motion. This is opposite to the behavior in ordinary ionomers.<sup>19</sup>

In order to correlate the decoupling behavior of PILs with their chemical structures, Sokolov et al.<sup>18</sup> proposed two parameters: One is the decoupling ratio defined as the characteristic time ratio of structural relaxation to conductivity at the glass transition temperature. The other is the decoupling exponent estimated using a Walden plot in which ionic

conductivity is plotted as a function of inverse of viscosity. They concluded that the packing frustration in PILs affects the degree of decoupling. When the polymer segments are loosely packed, ions can diffuse easily and hence high ionic conductivity is achieved.

Although a lot of efforts to clarify the relationship between morphology, ion or polymer dynamics, and ionic conductivities of PILs has been made so far, the comprehensive understanding is not achieved. This is because most of researchers are focusing on the effect of either chemical structures of polyions or those of counter ions on ionic conductivities. Therefore, it is inevitably required to consider both effects at the same time through tuning the chemical structures of polyions and counter ions, systematically.

### **1-2-2 Linear Viscoelasticity**

PILs can be classified as a sort of ionomers like sodium polystyrene sulfonate because they consist of electrolyte monomer units. Therefore, PILs can be regarded as model systems of molten ionomers. Nakamura et al.<sup>16,20</sup> have firstly studied the viscoelastic responses of PILs over a wide frequency range covering from the glassy zone to the terminal flow.

According to their results, the glassy modulus of PILs is smaller than that of polystyrene, which may be regarded as the representative of ordinary amorphous polymers. The values slightly depend on ionic sizes of counter ions and molecular weights of PILs. In the glass-to-rubber transition zone, PILs showed broadening of the relaxation spectra with increasing ionic sizes of counter anions, indicating the existence of a new relaxation mechanism around the  $T_g$ . They proposed two molecular origins for this relaxation mechanism. One is the rotational motions of ion pair, and the other is the local motion of the polymer chain.

Above the glass transition temperature, Nakamura et al.<sup>16,20</sup> showed the distinguished linear viscoelastic behavior for poly(1-ethyl-3-vinylimidazolium bis(trifluoromethanesulfonyl)imide) (PC<sub>2</sub>-TFSI) from that for poly(1-butyl-3-vinylimidazolium bis(trifluoromethanesulfonyl)imide) (PC<sub>4</sub>-TFSI) having butyl groups instead

of ethyl groups even though they have the similar molecular weight each other. For PC<sub>2</sub>-TFSI, the time temperature superposition (TTS) does not hold in the rubbery zone while for PC<sub>4</sub>-TFSI the TTS hold over the whole frequency range from the glassy to the terminal flow region. This result suggests the structural changes in PC<sub>2</sub>-TFSI. Based on the linear viscoelastic spectra, they proposed the presence of ionic aggregates in the PC<sub>2</sub>-TFSI system.

Among several characteristics concerning molecular structure of repeating units, the ratio of ionic sizes of cations and anions might be mostly related to the mechanical response of PILs. Figure 1–2 shows the chemical structure of repeating units for PC<sub>2</sub>-TFSI. Imidazolium cations can be divided into two parts: One is polar groups composed of imidazolium rings. The other is apolar groups composed of alkyl chains. It is considered that apolar groups hinder ions from forming ionic aggregates. For PC<sub>2</sub>-TFSI, the ionic sizes of cations are smaller than those of anions while for PC<sub>4</sub>-TFSI the ionic sizes of cations are larger than those of anions. Thus, the ionic aggregates could be formed due to the weak steric hindrance resulting from the shorter alkyl chains.

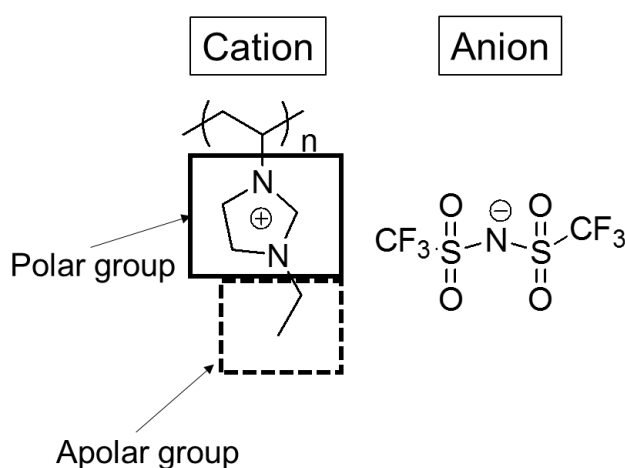


Figure 1–2. Chemical structure of poly(1-ethyl-3-vinylimidazolium bis(trifluoromethanesulfonyl)imide), PC<sub>2</sub>-TFSI.

### 1-3 Rheo-Optical Studies for Analysis of Polymer Dynamics

#### 1-3-1 Stress-Optical Rule (SOR)

As we have seen in the previous sections, PILs shows unique viscoelastic relaxations. In order to elucidate the molecular origin of viscoelastic relaxations, the rheo-optical method, i.e. the simultaneous measurement of stress and strain-induced birefringence, is a useful technique. This is because the birefringence has a strong correlation with the stress. This correlation is called as the stress-optical rule (SOR). In this section, the principle of the rheo-optical method is briefly reviewed.

The SOR says the deviatoric part of stress tensor  $\boldsymbol{\sigma}$  is proportional to the deviatoric part of polarizability tensor,  $\boldsymbol{\alpha}$ , as<sup>21</sup>

$$\boldsymbol{\alpha} = P\boldsymbol{\sigma} \quad (1-1)$$

Here,  $P$  is the proportionality factor.

Following the paper of Watanabe et al.,<sup>22</sup> let us consider a polymeric system where the number density of polymer chains is  $\nu$  and the polymer chain is composed of  $N$  subchains as illustrated in Figure 1-2.

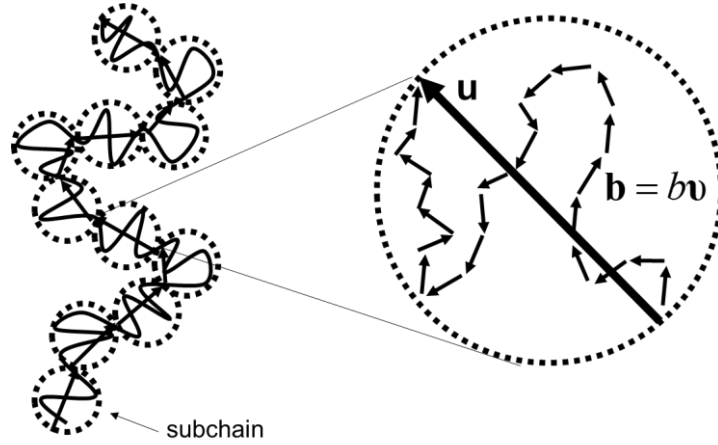


Figure 1–3. Schematic illustration of a chain and subchains. The short arrows represent the end-to-end vector of viscoelastic segments with length  $b$ .

In this case, the deviatoric part of stress tensor can be described in terms of the end-to-end vector,  $\mathbf{u}$ , of the subchain as

$$\boldsymbol{\sigma}(t) = \frac{3\nu N k_B T}{n_s b^2} \left\{ \langle \mathbf{u}\mathbf{u} \rangle - \frac{\mathbf{I}}{3} \text{tr} \langle \mathbf{u}\mathbf{u} \rangle \right\} \quad (1-2)$$

$$\langle \mathbf{u}\mathbf{u} \rangle = \frac{1}{N} \sum_{n=1}^N \langle \mathbf{u}(n, t) \mathbf{u}(n, t) \rangle \quad (1-3)$$

Here,  $n_s$  is the number of viscoelastic segments in the subchain, and  $b$  is the length of viscoelastic segments.  $k_B$  and  $T$  represent the Boltzmann constant and the absolute temperature, respectively.  $\langle \mathbf{u}\mathbf{u} \rangle$  is the ensemble average of the dyadic  $\mathbf{u}\mathbf{u}$  and  $\mathbf{I}$  is the unit tensor.  $n$  is the suffix of viscoelastic segments in subchain. Under relatively small deformation,  $\boldsymbol{\sigma}(t)$  can be related with the average orientational anisotropy tensor of the monomeric rod,  $\mathbf{O} = \langle \mathbf{v}\mathbf{v} \rangle - (\mathbf{I}/3) \text{tr} \langle \mathbf{v}\mathbf{v} \rangle$ , where  $\mathbf{v}$  is the end-to-end vector of the rod.

$$\left\{ \langle \mathbf{u}\mathbf{u} \rangle - \frac{\mathbf{I}}{3} \text{tr} \langle \mathbf{u}\mathbf{u} \rangle \right\} = \frac{5}{3} n_s^2 b^2 \left\{ \langle \mathbf{v}\mathbf{v} \rangle - \frac{\mathbf{I}}{3} \text{tr} \langle \mathbf{v}\mathbf{v} \rangle \right\} \quad (1-4)$$

$$\boldsymbol{\sigma}(t) = 5n_s \nu N k_B T \left\{ \langle \mathbf{vv} \rangle - \frac{\mathbf{I}}{3} \text{tr} \langle \mathbf{vv} \rangle \right\} \quad (1-5)$$

On the other hand, according to Kuhn and Grün,<sup>23</sup> the deviatoric part of polarizability tensor,  $\boldsymbol{\alpha}$ , of the subchain is defined in terms of  $\mathbf{O}$  as

$$\begin{aligned} \boldsymbol{\alpha}(t) &= \frac{3}{5} \frac{\Delta\beta}{n_s b^2} \left\{ \langle \mathbf{uu} \rangle - \frac{\mathbf{I}}{3} \text{tr} \langle \mathbf{uu} \rangle \right\} \\ &= \Delta\beta n_s \left\{ \langle \mathbf{vv} \rangle - \frac{\mathbf{I}}{3} \text{tr} \langle \mathbf{vv} \rangle \right\} \end{aligned} \quad (1-6)$$

Here,  $\Delta\beta$  is the anisotropy of the polarizability of the rod. To correlate  $\boldsymbol{\alpha}(t)$  with the deviatoric part of refractive index tensor (e.g. birefringence),  $\mathbf{n}(t)$ , Kuhn and Grün<sup>23</sup> applied the Lorent-Lorenz equation and obtained eq. (1-7) as follows

$$\mathbf{n}(t) = \frac{2\pi}{9} \frac{(n^2 + 2)^2}{n} N \nu n_s \Delta\beta \left\{ \langle \mathbf{vv} \rangle - \frac{\mathbf{I}}{3} \text{tr} \langle \mathbf{vv} \rangle \right\} \quad (1-7)$$

Substituted  $\boldsymbol{\alpha}$  and  $P$  in eq. (1-1) to  $\mathbf{n}$  and  $C_R$ , we can calculate the proportional factor,  $C_R$ , in terms of  $\mathbf{n}$  and  $\Delta\beta$  from eq. (1-5) and eq. (1-7).

$$C_R = \frac{2\pi}{45k_B T} \frac{(n^2 + 2)^2}{n} \Delta\beta \quad (1-8)$$

$C_R$  is called the stress-optical coefficient.

### 1-3-2 Modified Stress-Optical Rule (MSOR)

The SOR indicates that the molecular origin of both stress and birefringence is the

orientation of viscoelastic segments. Therefore, it is well known that the SOR holds well in systems of polymer melts and concentrated polymer solutions in the time-scale range from the rubbery to the flow zone.<sup>24</sup>

Around the glass-to-rubber transition zone, the SOR does not hold valid and alternatively the modified stress-optical rule, MSOR, holds well.<sup>25</sup> This is because the glassy component contributes to the stress and the birefringence in addition to the rubbery component originating from the segment orientation around the transition zone. The MSOR says that the both the stress and birefringence are composed of two components, R and G, and the ordinary proportionality holds valid for each component. Here, R and G stand for the rubbery and glassy components, respectively. For example, under oscillatory tensile deformation, the MSOR provides the following simultaneous equations.

$$E^*(\omega) = E_R^*(\omega) + E_G^*(\omega) \quad (1-9)$$

$$O^*(\omega) = C_R E_R^*(\omega) + C_G E_G^*(\omega) \quad (1-10)$$

Here,  $E^*$  and  $O^*$  represent the parameters corresponding to the stress and birefringence, respectively.

The sign and the order of stress optical coefficient, and the frequency dependence of each component enable us to predict the molecular origin of stress.

#### 1-4 Scope of This Thesis

The goal of this thesis is to provide the comprehensive understanding of the relationship between viscoelastic properties, ionic conductivity, morphology, and chemical structures of PILs.

Figure 1-3 shows the chemical structures of imidazolium-based PILs used in this thesis. Poly(1-alkyl-3-vinylimidazolium)-based ionic liquids with different alkyl chain lengths

and various counter anion species are used. Hereafter, the PILs are abbreviated as  $PC_m\text{-X}$  where  $m$  is the number of alkyl chains and X is the counter anion species. For example, poly(1-hexyl-3-vinylimidazolium bis(trifluoromethanesulfonyl)imide) is abbreviated as  $PC_6\text{-TFSI}$ .

This thesis consists of the following six chapters.

In chapter 2, the molecular origin for the new relaxation process observed in the glass-to-rubber transition zone of PILs is discussed using simultaneous measurements of the stress and birefringence. The effects of negative charge positions and shapes of counter anions on this new relaxation process is also discussed. Here, poly(1-butyl-3-vinylimidazolium)-based ionic liquids with  $\text{BF}_4$ , TfO, NfO, TFSI, or CPFSI anions are used.

In chapter 3, I show a thermally stable liquid crystal like ordered structure observed in a polymerized ionic liquids by incorporating counter anions having ionic sizes larger than those of polycations. Here, poly(1-butyl-3-vinylimidazolium)-based ionic liquids with TFSI, PFSI, and HFSI anions in order to discuss the effects of ionic volume ratio of an anion to a cation.

In chapter 4, the relationship between ionic transporting mechanism and morphology of a series of poly(1-alkyl-3-vinylimidazolium)-based ionic liquids having various counter anions is discussed using linear viscoelastic measurements, dielectric relaxation spectroscopy, and wide-angle X-ray scattering. The decoupling behavior observed in PILs systems is correlated with the volume ratio of cations and anions.

In chapter 5, the dynamic rigidity of polyelectrolyte in ionic liquids is discussed using a simultaneous measurement of the stress and birefringence. The Rouse segment size for polyelectrolyte/ionic liquid dilute solutions is compared with that for electrically neutral polymer solution systems in order to clarify the effects of electrostatic interaction on local dynamics of polymers. Here, poly(1-butyl-3-vinylimidazolium)-based ionic liquids with Cl,  $\text{BF}_4$ , and TFSI anions are used as polyelectrolytes.

In chapter 6, I summarize this dissertation thesis.

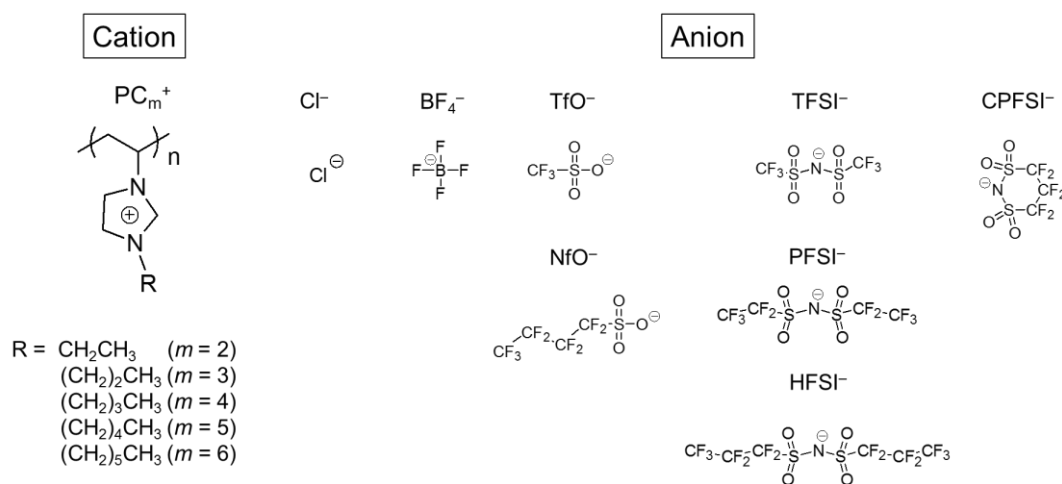


Figure 1–4. Chemical structures of repeating units of PILs used in this thesis. Cations: poly(1-alkyl-3-vinylimidazolium) ( $PC_m^+$ ) from ethyl ( $m = 2$ ) to hexyl ( $m = 6$ ). Anions: chloride ( $Cl^-$ ), tetrafluoroborate ( $BF_4^-$ ), trifluoromethanesulfonate ( $TfO^-$ ), nonafluorobutanesulfonate ( $NfO^-$ ), bis(trifluoromethanesulfonyl)imide ( $TFSI^-$ ), bis(pentafluoroethanesulfonyl)imide ( $PFSI^-$ ), bis(heptafluoropropanesulfonyl)imide ( $HFSI^-$ ), and 1,1,2,2,3,3-hexafluoropropane-1,2-disulfonimide ( $CPFSI^-$ ).

## 1–5 References

- (1) Wilkes, J. S. *Green Chemistry* **2002**, 4, 73-80.
- (2) Yamagata, M.; Tanaka, K.; Tsuruda, Y.; Sone, Y.; Fukuda, S.; Nakasuka, S.; Kono, M.; Ishikawa, M. *Electrochemistry* **2015**, 83, 918-924.
- (3) Arimoto, S.; Oyamatsu, D.; Torimoto, T.; Kuwabata, S. *Chemphyschem* **2008**, 9, 763-767.
- (4) Mecerreyes, D. *Prog. Polym. Sci.* **2011**, 36, 1629-1648.
- (5) Ohno, H.; Ito, K. *Chem. Lett.* **1998**, 751-752.
- (6) Yuan, J. Y.; Antonietti, M. *Polymer* **2011**, 52, 1469-1482.
- (7) Yuan, J. Y.; Mecerreyes, D.; Antonietti, M. *Prog. Polym. Sci.* **2013**, 38, 1009-1036.
- (8) Tang, J. B.; Tang, H. D.; Sun, W. L.; Radosz, M.; Shen, Y. Q. *J Polym Sci Pol Chem* **2005**, 43, 5477-5489.
- (9) Obadia, M. M.; Mudraboyina, B. P.; Serghei, A.; Phan, T. N. T.; Gimes, D.; Drockenmuller, E. *Acs Macro Lett* **2014**, 3, 658-662.
- (10) Smith, T. W.; Zhao, M.; Yang, F.; Smith, D.; Cebe, P. *Macromolecules* **2013**, 46, 1133-1143.

- (11) Evans, C. M.; Bridges, C. R.; Sanoja, G. E.; Bartels, J.; Segalman, R. A. *Acs Macro Lett* **2016**, *5*, 925-930.
- (12) Sanoja, G. E.; Popere, B. C.; Beckingham, B. S.; Evans, C. M.; Lynd, N. A.; Segalman, R. A. *Macromolecules* **2016**, *49*, 2216-2223.
- (13) Green, M. D.; Salas-de la Cruz, D.; Ye, Y. S.; Layman, J. M.; Elabd, Y. A.; Winey, K. I.; Long, T. E. *Macromol. Chem. Phys.* **2011**, *212*, 2522-2528.
- (14) Salas-de la Cruz, D.; Green, M. D.; Ye, Y. S.; Elabd, Y. A.; Long, T. E.; Winey, K. I. *J Polym Sci Pol Phys* **2012**, *50*, 338-346.
- (15) Sangoro, J. R.; Iacob, C.; Agapov, A. L.; Wang, Y.; Berdzinski, S.; Rexhausen, H.; Strehmel, V.; Friedrich, C.; Sokolov, A. P.; Kremer, F. *Soft Matter* **2014**, *10*, 3536-3540.
- (16) Nakamura, K.; Fukao, K.; Inoue, T. *Macromolecules* **2012**, *45*, 3850-3858.
- (17) Choi, U. H.; Ye, Y. S.; de la Cruz, D. S.; Liu, W. J.; Winey, K. I.; Elabd, Y. A.; Runt, J.; Colby, R. H. *Macromolecules* **2014**, *47*, 777-790.
- (18) Fan, F.; Wang, Y. Y.; Hong, T.; Heres, M. F.; Saito, T.; Sokolov, A. P. *Macromolecules* **2015**, *48*, 4461-4470.
- (19) Fan, F.; Wang, W. Y.; Holt, A. P.; Feng, H. B.; Uhrig, D.; Lu, X. Y.; Hong, T.; Wang, Y. Y.; Kang, N. G.; Mays, J.; Sokolov, A. P. *Macromolecules* **2016**, *49*, 4557-4570.
- (20) Nakamura, K.; Saiwaki, T.; Fukao, K.; Inoue, T. *Macromolecules* **2011**, *44*, 7719-7726.
- (21) H, J.-K. *Springer: Berlin* **1983**.
- (22) Watanabe, H.; Matsumiya, Y.; Inoue, T. *Nihon Reoroji Gakk* **2015**, *43*, 105-112.
- (23) Kuhn, W.; Grun, F. *Kolloid Z* **1942**, *101*, 248-271.
- (24) Janeschitz-Kriegl, H. *Adv. Polym. Sci.* **1969**, 170.
- (25) Inoue, T.; Okamoto, H.; Osaki, K. *Macromolecules* **1991**, *24*, 5670-5675.

---

## CHAPTER 2

# Rheo-Optical Studies on Dynamics of Polymerized Ionic Liquids with Various Counter Anions

---

### 2-1 Introduction

Most of polymerized ionic liquids, PILs, are amorphous and show the glass transition phenomenon. A pioneer work on viscoelastic properties of PILs reported broadening of the viscoelastic spectrum around the glass transition zone depending on the molecular structure of repeating units.<sup>1,2</sup> In this chapter, I am focusing on linear viscoelasticities of PILs with the aim of clarifying the molecular origin of the broadening of viscoelastic spectrum in the vicinity of glass transition zone. For this purpose, the dynamic viscoelasticity and birefringence were employed on five poly(1-butyl-3-vinylimidazolium)-based PILs. Figure 2-1 shows the chemical structures of cations and anions used in this chapter. I show that the molecular origin of the broad relaxation spectra can be attributed to cooperative local motions of chains. In addition, the effects of the shape of counter anions and those of the negative charge positions on the cooperative local motion are discussed.

### 2-2 Experimental Methods

**Materials.** 1-Vinylimidazole was purchased from TCI and used after distillation. Lithium trifluoromethanesulfonate (LiTfO) and lithium 1,1,2,2,3,3-hexafluoropropane-1,2-disulfonimide (LiCPFSI) were purchased from TCI. 1-Bromobutane, 2,2'-azobis(isobutyronitrile) (AIBN), lithium bis(trifluoromethanesulfonyl)imide (LiTFSI), lithium nonafluorobutanesulfonate (LiNfO), and sodium tetrafluoroborate (NaBF<sub>4</sub>) were purchased from Wako Pure Chemicals. These materials were used as received. Deuterated water (D<sub>2</sub>O)

was purchased from Merck and used as a solvent in NMR measurements. Deionized water was obtained using an Elix system (Japan Millipore, Tokyo, Japan) and used as the pure water.

**Synthesis.** 1-Butyl-3-vinylimidazolium bromide ( $C_4\text{-Br}$ ) was synthesized by refluxing 1-vinylimidazole and excess 1-bromobutane in methanol at  $60^\circ\text{C}$  for 3 days. The molar ratio of 1-bromobutane to 1-vinylimidazole was 1.29 and the volume ratio of 1-vinylimidazole to solvent was 1.1. After the evaporation of methanol and unreacted 1-bromobutane at  $50^\circ\text{C}$ ,  $C_4\text{-Br}$  was dried overnight at  $50^\circ\text{C}$ . The purity of  $C_4\text{-Br}$  was confirmed by  $^1\text{H-NMR}$  in  $\text{D}_2\text{O}$ . (ppm)  $\delta$  9.1 (1H, s,  $\text{N-CH-N}$ ),  $\delta$  7.8 (1H, d,  $\text{N-CH=CH-N-Bu}$ ),  $\delta$  7.7 (1H, d,  $\text{N-CH=CH-N-Bu}$ ),  $\delta$  7.2 (1H, q,  $\text{CH}_2=\text{CH-N}$ ),  $\delta$  5.9 (1H, dd,  $\text{trans-CH}_2=\text{CH-N}$ ),  $\delta$  5.5 (1H, dd,  $\text{cis-CH}_2=\text{CH-N}$ ),  $\delta$  4.3 (2H, t,  $\text{N-CH}_2\text{-CH}_2\text{-CH}_2\text{-CH}_3$ ),  $\delta$  2.0 (2H, m,  $\text{N-CH}_2\text{-CH}_2\text{-CH}_2\text{-CH}_3$ ),  $\delta$  1.4 (2H, m,  $\text{N-CH}_2\text{-CH}_2\text{-CH}_2\text{-CH}_3$ ),  $\delta$  1.0 (3H, t,  $\text{N-CH}_2\text{-CH}_2\text{-CH}_2\text{-CH}_3$ ))

Poly(1-butyl-3-vinylimidazolium bromide) ( $\text{PC}_4\text{-Br}$ ) was prepared by free radical polymerization of  $C_4\text{-Br}$ . Polymerization was initiated by AIBN at  $60^\circ\text{C}$  for 16 hours in deionized water (6 mL). The molar ratio of monomer to initiator,  $M_M/M_I$ , was 100. The ratio,  $M_M/M_I$ , for the preparation of each PIL summarized in Table 2-1 is different from each other and hence the molecular weight can be different from each other. However, based on the results of linear viscoelastic responses shown below, we found that each PIL has the molecular weight high enough so that the effects of molecular weight on linear viscoelastic behavior near glass-to-rubber transition zone can be negligible. After the polymerization,  $\text{PC}_4\text{-Br}$  was dialyzed against deionized water for a few days by using a No.2 Spectra/Por membrane. Subsequently, the obtained solution was dried via freeze-drying method and  $\text{PC}_4\text{-Br}$  was obtained as a powder. Elimination of  $C_4\text{-Br}$  monomer from the product was confirmed using  $^1\text{H-NMR}$  in  $\text{D}_2\text{O}$ . Here, it should be noted that some bromide ions can be replaced with hydroxyl ions during the dialysis.

Samples of PC<sub>4</sub>-BF<sub>4</sub>, PC<sub>4</sub>-TfO, PC<sub>4</sub>-NfO, PC<sub>4</sub>-TFSI, and PC<sub>4</sub>-CPFSI were prepared using the counterion conversion method proposed by Mecerreyes.<sup>3</sup> For the preparation of PC<sub>4</sub>-NfO, an aqueous solution of LiNfO was slowly titrated into aqueous solution of PC<sub>4</sub>-Br and stirred for at least 1 day at room temperature. The molar ratio of salt to pre-polymer,  $M_{SA}/M_P$ , was 1.51. The resultant precipitation was washed with deionized water until the filtrate remained transparent when adding an aqueous solution of AgNO<sub>3</sub>. The purity of PC<sub>4</sub>-NfO was confirmed using elemental analysis and X-ray fluorescence spectrometry. The ratio,  $M_{SA}/M_P$ , for the preparation of each PIL summarized in Table 2–1 was varied in order to achieve the complete ion conversions. The results of elemental analysis and X-ray fluorescence spectroscopy were summarized in Table 2–2. Consequently, the exchange ratio from the bromide ions to the aimed anions was almost 100%. Here, the X-ray fluorescence spectroscopy was conducted to estimate the weight fraction of the residual bromide ions in the product,  $W_{Br}$ .

The van der Waals volume,  $V$ , and the aspect ratio,  $R$ , of ions were estimated using the program built into the Winmostar version 6.018 software, and the results are listed in Table 2–3. The  $V$  for a cation was calculated using a structure of 1-butyl-3-methylimidazolium cation (Bmim<sup>+</sup>) as shown in Figure 1–1. Here, the all trans configurations for butyl groups on Bmim<sup>+</sup> and nonafluorobutyl groups on NfO<sup>–</sup> were considered in the calculations. The NfO anion has the similar ionic volume and shape to that of the TFSI anion. The difference can be in the degree of charge delocalization due to the difference in the position of charges. Comparing the molecular characteristics between TFSI and CPFSI anions, the aspect ratio is quite different each other. The CPFSI anion has the circular shape. The volume ratio,  $V_r = V_a / V_c$ , of an anion,  $V_a$ , and a cation,  $V_c$ , is  $V_r = 0.32$  for PC<sub>4</sub>-BF<sub>4</sub> and  $V_r = 0.55$  for PC<sub>4</sub>-TfO. The  $V_r$ s for PC<sub>4</sub>-TFSI, PC<sub>4</sub>-CPFSI, and PC<sub>4</sub>-NfO are almost unity.

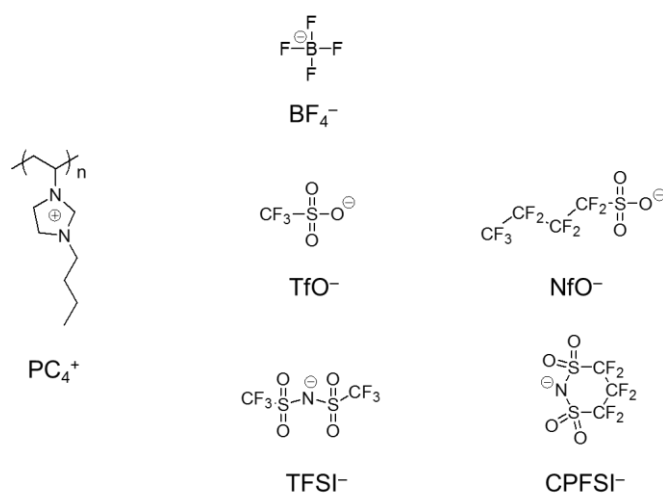


Figure 2–1. Chemical structures of a polycation, poly(1-butyl-3-vinylimidazolium) ( $\text{PC}_4^+$ ), and anions, tetrafluoroborate ( $\text{BF}_4^-$ ), trifluoromethanesulfonate ( $\text{TfO}^-$ ), nonafluorobutanesulfonate ( $\text{NfO}^-$ ), bis(trifluoromethanesulfonylimide) ( $\text{TFSI}^-$ ), and 1,1,2,2,3,3-hexafluoropropane-1,2-disulfonylimide ( $\text{CPFSI}^-$ ).

Table 2–1. Molar ratio of monomer to initiator,  $M_M/M_I$ , molar ratio of salt to pre-polymer,  $M_{SA}/M_P$ , used for the preparation of the aimed PILs, and the exchange rate of anions.

Sample Code	$M_M/M_I$	$M_{SA}/M_P$	Exchange rate /%
PC <sub>4</sub> -TFSI	100	1.02	~100
PC <sub>4</sub> -TfO	98.9	1.52	98.7
PC <sub>4</sub> -BF <sub>4</sub>	98.9	2.55	99.7
PC <sub>4</sub> -CPFSI	98.0	1.30	99.9
PC <sub>4</sub> -NfO	33.3	1.51	99.9

Table 2–2. Weight fraction of elements, carbon, hydrogen, nitrogen for the products determined from the elemental analysis. Weight fractions of the residual bromide ions in the product are also shown.

Sample Code	C /wt%	H /wt%	N /wt%	Br /wt%
PC <sub>4</sub> -TFSI	30.85 (30.62)	3.47 (3.51)	9.86 (9.74)	NA
PC <sub>4</sub> -TfO	39.32 (39.99)	5.26 (5.04)	9.37 (9.33)	1.3
PC <sub>4</sub> -BF <sub>4</sub>	43.20 (45.40)	6.35 (6.36)	11.35 (11.77)	0.26
PC <sub>4</sub> -CPFSI	32.68 (32.50)	3.33 (3.42)	9.49 (9.48)	0.078
PC <sub>4</sub> -NfO	34.12 (34.67)	3.34 (3.36)	6.24 (6.22)	0.12

( ): Theoretical values

Table 2–3. Van der Waals volume,  $V$ , and the aspect ratio,  $R$ , of PC<sub>4</sub><sup>+</sup> and counter anions.

	PC <sub>4</sub> <sup>+</sup>	BF <sub>4</sub> <sup>-</sup>	TfO <sup>-</sup>	NfO <sup>-</sup>	TFSI <sup>-</sup>	CPFSI <sup>-</sup>
$V/\text{nm}^3$	0.15	0.048	0.082	0.16	0.15	0.16
$R$	1.91	1.00	1.02	1.62	1.50	1.04

### Methods.

**a) Thermal Analysis.** Thermal analysis was carried out by a differential scanning calorimetry (DSC) measurement with the use of an EXSTAR 6000 (Hitachi High-Tech Science Corporation). Sample films of 6.27–12.1 mg were placed in open pans and then annealed before being hermetically sealed. Temperature ramps cycled from 20°C to 190°C with cooling and heating rates of 10 °C/min. The glass transition temperature,  $T_g$ , was determined as the midpoint of the heat capacity change in the second heating process. The value of  $T_g$  for each PIL is listed

in Table 2–4. The  $T_g$  for PC<sub>4</sub>-TFSI was much smaller than the others. The difference in  $T_g$  will be discussed in chapter 4.

**b) Rheo-Optical Measurement.** The experimental apparatus for rheo-optical measurements under oscillatory shear and tensile deformation is reported elsewhere.<sup>4, 5</sup> In short, Figure 3–2 shows the schematic illustrations of apparatus.

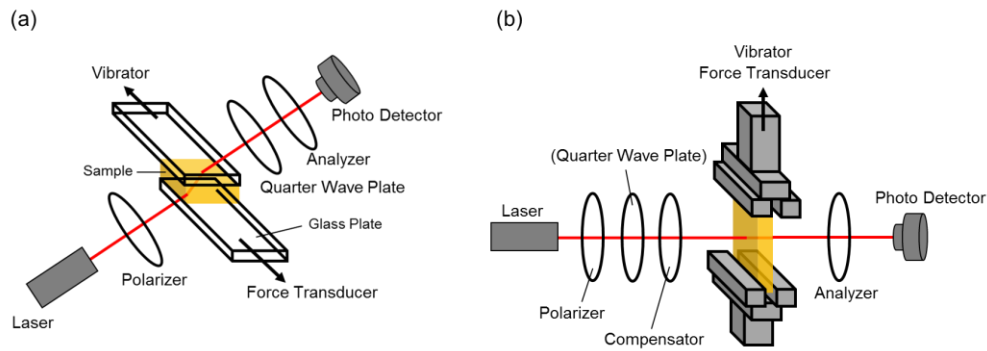


Figure 2–2. Schematic illustrations of (a) shear type apparatus and (b) tensile type apparatus.

When using the apparatus shown in Figure 2–2 (a) with oscillatory shear deformation  $\gamma^* = \gamma_0 \exp(i\omega t)$ , the shear stress,  $\sigma_{xy}^*$ , calculated from the force,  $f^*$ , is described as follows.

$$\sigma_{xy}^* = f^* / A = \sigma_0 \exp(i\omega t + \delta) \quad (2-1)$$

Here,  $A$  is the area of the upper plate of the apparatus.  $x$  is the axis parallel to the direction of induced shear deformation and  $y$  is the axis perpendicular to the direction of shear plane. The vibration amplitude of the force and the phase shift,  $\delta$ , are detected using a lock-in-amplifier. The complex shear modulus,  $G^*$ , is defined as the complex ratio of the shear stress to the strain.

$$G^* = \sigma_{xy}^* / \gamma^* \quad (2-2)$$

The measurable parameter corresponding to the birefringence is the difference between the principal values of refractive index tensor. For the case of Sénarmont optical train, the birefringence,  $\Delta n^Z (\equiv n_X - n_Y)$ , can be calculated from the intensity of light.

$$\Delta n^Z = \frac{\lambda}{2\pi d \alpha} \frac{\Delta I_\omega}{I_0} \tan \theta \quad (2-3)$$

Here,  $\lambda$  is the wavelength of the incident light in vacuum,  $d$  is the distance between a pair of the glass plates, and  $\theta$  is the refraction angle, respectively.  $I_0$  and  $\Delta I_\omega$  are respectively the intensities of incident light and the light transmitted through the sample. A small angle,  $\alpha$ , is the small offset angle ( $\sim 4^\circ$ ) of analyzer. The  $xy$  component of refractive index tensor,  $n_{xy}$ , can be related to  $\Delta n^Z$  through eq. (2-4)

$$n_{xy} = \frac{1}{2} \Delta n^Z \sin 2\chi_B \quad (2-4)$$

Here,  $\chi_B$  is the extinction angle and can be  $(1/4)\pi$  under small shear deformations. The complex shear birefringence,  $\Delta n^{Z*}$ , is then expressed as follows.

$$\Delta n^{Z*} = \Delta n^Z \exp(i\omega t + \delta_B) \quad (2-5)$$

$\Delta I_\omega$  and  $\delta_B$  can be detected using a lock-in-amplifier. The complex strain-optical coefficient,  $K^*$ , is obtained from eq. (2-4) and eq. (2-5).

$$K^* = \Delta n^{z^*} / 2\gamma^* = n_{xy}^* / \gamma^* \quad (2-6)$$

To check the reliability of the data measured with the shear birefringence apparatus,  $G^*$  was measured using an ARES-G2 system (TA Instruments) with a homemade parallel plates fixture having 4 mm diameter. Instrument compliance was carefully corrected with the method reported by McKenna et al.<sup>6, 7</sup> All the measurements were performed under a nitrogen atmosphere with a temperature range of 35–260°C.

## 2-3 Results and Discussion

### 2-3-1 Overview of Modulus and Strain-Optical Coefficient

Figure 2-3 displays the composite curves for the complex shear modulus,  $G^*=G'+iG''$ , and the complex Young's modulus,  $E^*=E'+iE''$ , for PC<sub>4</sub>-BF<sub>4</sub>. In what follows, I will not distinguish  $G^*$  and  $E^*/3$ . The obtained spectra at various temperatures were reduced at a reference temperature  $T_r = T_g + 50K$  using the method of reduced variables. The superposition worked well over the whole frequency region including the glass-to-rubber transition zone. The frequency dependence of  $G^*$  and  $E^*$  coincides with that for PC<sub>4</sub>-BF<sub>4</sub> previously reported.<sup>2</sup>

Also included is the composite curves for the shear complex strain-optical coefficient,  $K^* = K' + iK''$ , and the tensile complex strain-optical coefficient,  $O^* = O' + iO''$ . Similarly, I will not distinguish  $K^*$  and  $O^*/3$ . The obtained spectra at various temperatures were reduced at a reference temperature  $T_r = T_g + 50K$  using the different shift factors from those of  $G^*$ . Birefringence at low frequencies was negative while it was positive at high frequencies. Similar frequency dependence of the complex strain-optical coefficient was observed for polystyrene.<sup>8</sup>

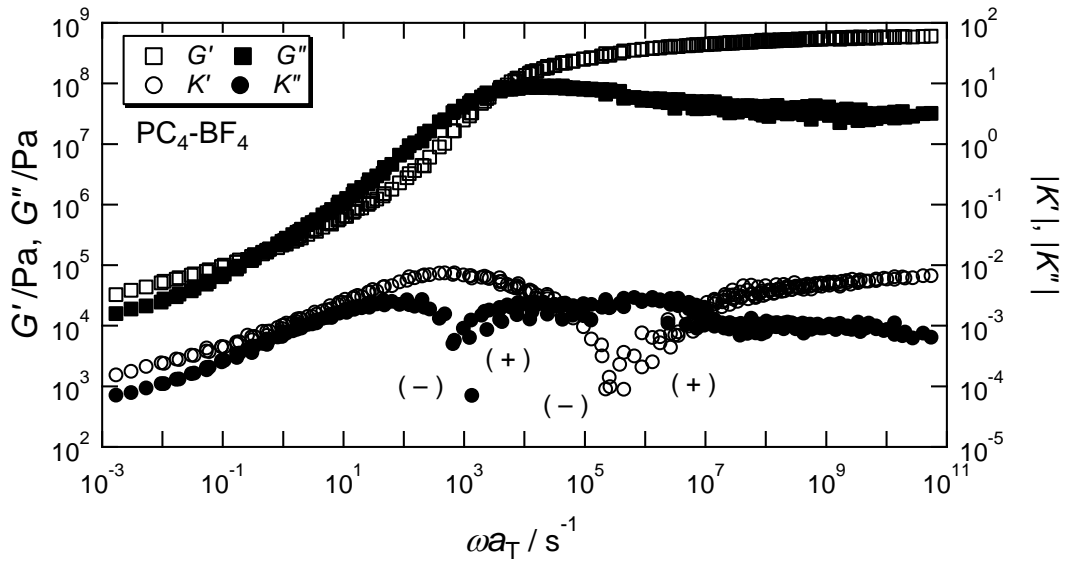


Figure 2-3. Composite curves of  $G^*$  (or  $E^*/3$ ) and  $K^*$  (or  $O^*/3$ ) for PC<sub>4</sub>-BF<sub>4</sub>.

Figure 2-4 shows the composite curves of  $G^*$  (or  $E^*/3$ ) and  $K^*$  (or  $O^*/3$ ) for PC<sub>4</sub>-TFSI. Again, the shift factors were utilized to make the composite curves reduced at  $T_r = T_g + 50\text{K}$ . The superposition worked well over the whole frequency region.

The linear viscoelastic spectra of  $G^*$  for PC<sub>4</sub>-TFSI around the glass-to-rubber transition zone was broader than the ordinary polymers such as polystyrene, similarly to the case reported by Nakamura et al.<sup>1</sup> This broadening indicates the existence of another relaxation mechanism. Here, I noted that a similar broadening of linear viscoelastic spectra is observed for poly(isobutylene)<sup>9</sup> and poly(methyl methacrylate).<sup>10</sup> On the other hand, the frequency dependence of  $K^*$  (or  $O^*/3$ ) was comparable to that for PC<sub>4</sub>-BF<sub>4</sub>. The similar frequency dependence was observed for PC<sub>4</sub>-CPFSI.

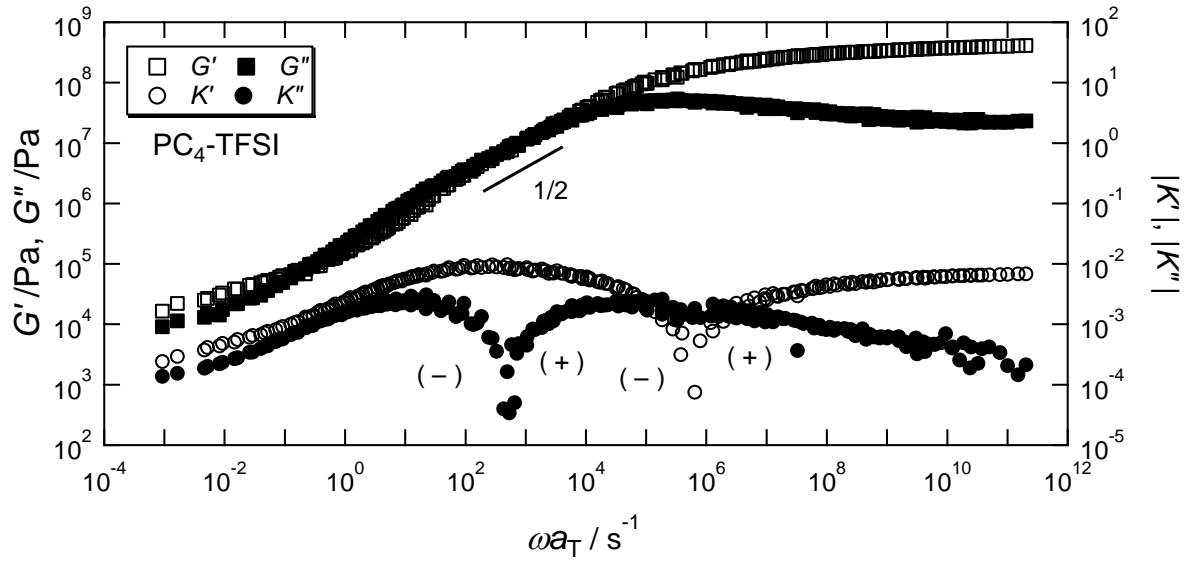


Figure 2–4. Composite curves of  $G^*$  (or  $E^*/3$ ) and  $K^*$  (or  $O^*/3$ ) for PC<sub>4</sub>-TFSI.

However, as shown in Figure 2–5, the frequency dependence of  $G^*$  (or  $E^*/3$ ) and  $K^*$  (or  $O^*/3$ ) for PC<sub>4</sub>-NfO was different from that for PC<sub>4</sub>-TFSI. The power law region showing  $G' \sim G'' \propto \omega^{1/2}$  in the glass-to-rubber transition zone for PC<sub>4</sub>-TFSI was not observed in the PC<sub>4</sub>-NfO system. Moreover, the transition width, which is estimated from the frequency width between crossovers of  $G'$  and  $G''$  at high and low frequencies, became smaller for PC<sub>4</sub>-NfO. As for the frequency dependence of  $K^*$ , the real part of  $K^*$  showed negative values over the whole frequency region, and three peaks were observed in the imaginary part of  $K^*$  at  $\omega a_T \cong 10^1$ ,  $10^3$ , and  $10^5 \text{ s}^{-1}$ .

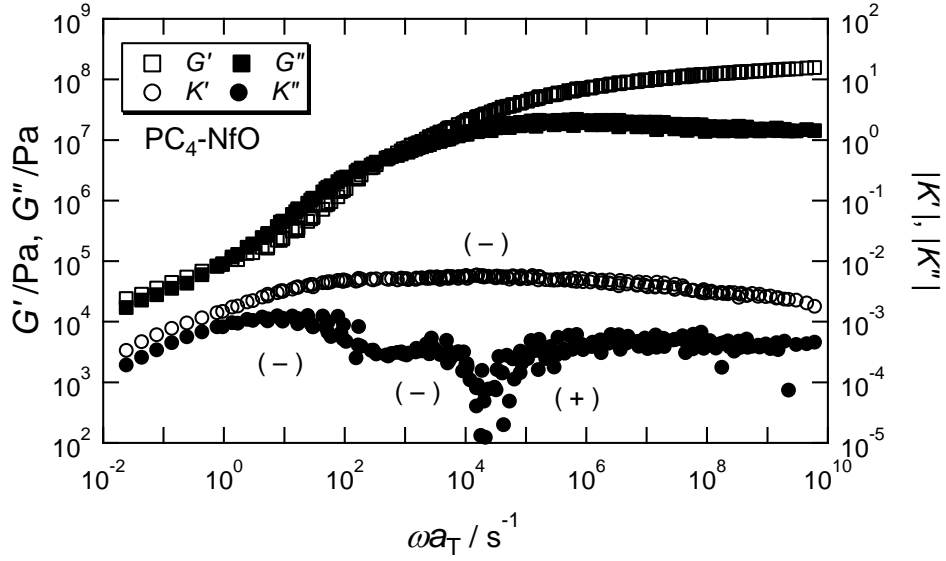


Figure 2–5. Composite curves of  $G^*$  (or  $E^*/3$ ) and  $K^*$  (or  $O^*/3$ ) for PC<sub>4</sub>-NfO. The reference temperature is chosen as  $T_r = 178^\circ\text{C}$ .

### 2–3–2 MSOR Analysis

As shown in Figures 2–3, 2–4, and 2–5, the SOR does not hold over the whole frequency region. This is because the glassy component contributes to both the modulus and the strain-optical coefficient at high frequencies. Therefore, I apply the two components MSOR for ordinary amorphous polymers.<sup>5</sup> The MSOR for the rubbery (R) and glassy (G) components can be written as follows.

$$G^*(\omega) = G_R^*(\omega) + G_G^*(\omega) \quad (2-7)$$

$$K^*(\omega) = C_R G_R^*(\omega) + C_G G_G^*(\omega) \quad (2-8)$$

Here,  $G_j^*(\omega)$  ( $j = \text{R, G}$ ) is the component function.  $C_R$  is the stress-optical coefficient for the rubbery component and can be estimated from the value of plateau region at the low frequency limit in  $K'/G'$  or  $K''/G''$ . In fact, the SOR holds valid at low frequencies,  $\omega a_T < 10^{-1} \text{ rad s}^{-1}$  for all the samples. It is because at low frequencies the glassy component is completely relaxed and

can be negligible.

$$K^*(\omega) = C_R G^*(\omega) \quad \text{at } \omega\alpha_T < 10^{-1} \text{ s}^{-1} \quad (2-9)$$

On the other hand,  $C_G$  is the stress-optical coefficient for the glassy component, which is defined as follows.

$$C_G = \lim_{\omega \rightarrow \infty} \frac{K''(\omega)}{G''(\omega)} \quad (2-10)$$

Following the definition of  $C_G$ , the  $C_G$  for PC<sub>4</sub>-TFSI was determined as  $C_G = 1.5 \times 10^{-11} \text{ Pa}^{-1}$ .

The other optical properties for the PILs I investigated were summarized in Table 2–4.

Table 2–4. The glass transition temperature  $T_g$  and optical properties of PILs

	$T_g$ /°C	$C_R$ / $10^{-12}\text{Pa}^{-1}$	$C_L$ / $10^{-12}\text{Pa}^{-1}$	$C_G$ / $10^{-12}\text{Pa}^{-1}$	$\Delta\alpha$ / $10^{-24}\text{cm}^{-3}$
PC <sub>4</sub> -BF <sub>4</sub>	134	-4100	NA	28	-1.7
PC <sub>4</sub> -TfO	118	-3300	NA	18	-1.4
PC <sub>4</sub> -NfO	128	-14000	-68	28	-1.4
PC <sub>4</sub> -TFSI	49.8	-14000	180	15	-2.3
PC <sub>4</sub> -CPFSI	99.8	-4800	63	7.5	-1.7
Polystyrene	102	-4700	NA	30	-1.9

Solving the simultaneous eq. (2–8) and eq. (2–9), we can determine the complex modulus of each component from the  $K^*$  and  $G^*$  data.

$$G_R^*(\omega) = \frac{K^*(\omega) - C_G G^*(\omega)}{C_R - C_G} \quad (2-11)$$

$$G_G^*(\omega) = \frac{K^*(\omega) - C_R G^*(\omega)}{C_G - C_R} \quad (2-12)$$

The results are shown in Figure 2-6 and 2-7 for PC<sub>4</sub>-TfO and PC<sub>4</sub>-TFSI, respectively. Here, I used the method of reduced variables for each component individually. The reference temperature is  $T_g + 50\text{K}$ .

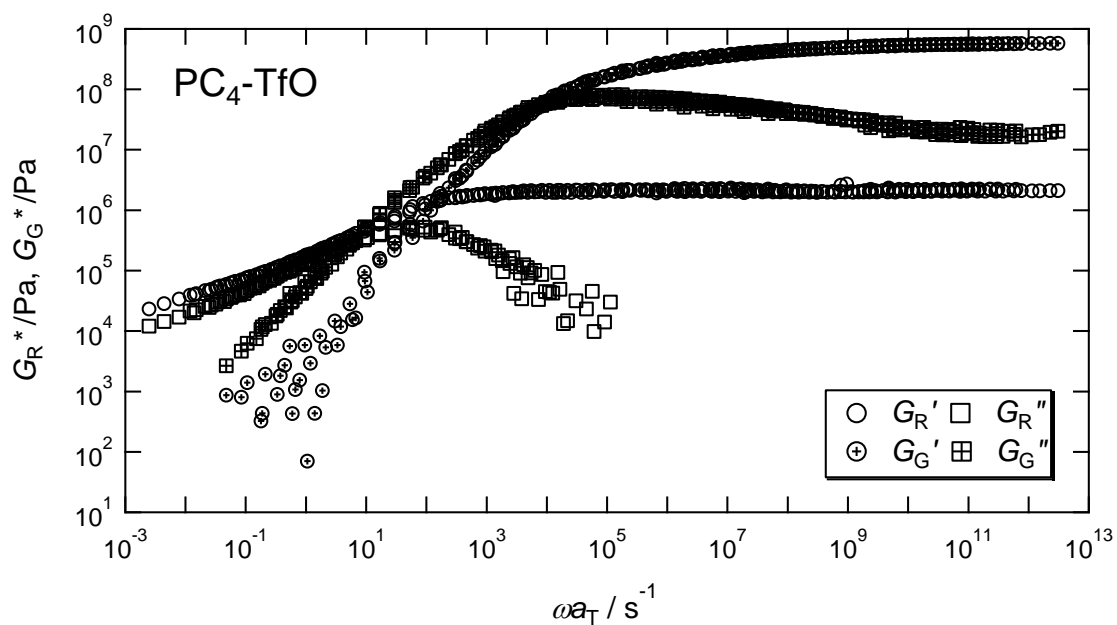


Figure 2-6. Component functions for PC<sub>4</sub>-TfO.

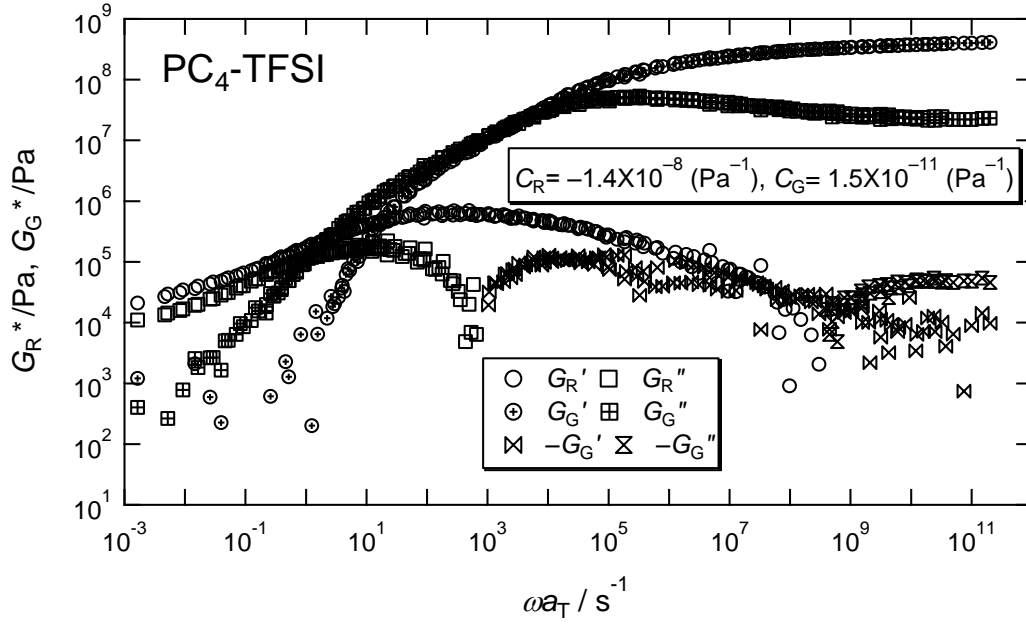


Figure 2–7. Component functions for PC<sub>4</sub>-TFSI determined by two components MSOR.

The R and G component functions for PC<sub>4</sub>-TfO and PC<sub>4</sub>-BF<sub>4</sub> (not shown here) are respectively very similar to those of polystyrene, indicating that the decomposition of the modulus is performed reasonably.

For the case of PS,  $G_G^*$  is very similar to  $G^*$  for oligostyrene ( $M \sim 1000 \text{ g mol}^{-1}$ ).<sup>11</sup> This result indicates that  $G_G^*$  is related to the local motion of chain,  $M < 1000 \text{ g mol}^{-1}$ . On the other hand, the R component for PC<sub>4</sub>-TFSI is different from ordinary component functions.  $G_R''$  was negative at high frequencies and  $G_R'$  showed a maximum around  $\log(\omega / \text{s}^{-1}) = 1$ . The phenomenological theory for linear viscoelasticity requires that  $G_R'$  should be a monotonically increasing function of  $\omega$  and  $G_R''$  should be positive. Therefore, I conclude that the two components MSOR does not work for PC<sub>4</sub>-TFSI.

Now, let us consider MSOR composed of three components. The MSOR for three components can be written as follows.

$$G^* = G_R^* + G_L^* + G_G^* \quad (2-13)$$

$$K^* = C_R G_R^* + C_L G_L^* + C_G G_G^* \quad (2-14)$$

If we solve these equations following the standard method for the two components MSOR, that is, if we calculate the right hand sides of eq. (2-13) and eq. (2-14), then we obtain

$$\frac{K^*(\omega) - C_G G^*(\omega)}{C_R - C_G} = G_R^*(\omega) + \frac{C_L - C_G}{C_R - C_G} G_L^*(\omega) \quad (2-15)$$

$$\frac{K^*(\omega) - C_R G^*(\omega)}{C_G - C_R} = G_G^*(\omega) + \frac{C_L - C_R}{C_G - C_R} G_L^*(\omega) \quad (2-16)$$

Equation 2-15 explains why the apparent R component,  $(K^*(\omega) - C_G G^*(\omega))/(C_R - C_G)$  shown in Figure 2-7, shows an anomalous frequency dependence. The function contains the contribution of the third unknown function,  $G_L^*$ . The coefficient  $(C_L - C_G)/(C_R - C_G)$  can be negative and hence the function shows the change of sign as shown in Figure 2-7.

Alternatively, if we can find true  $C_L$ , and then eq. (2-13) and eq. (2-14) are solved for  $G_R^*$  and  $G_L^*$ , the function,  $(K^*(\omega) - C_L G^*(\omega))/(C_R - C_L)$ , includes contribution of  $G_R^*$  and  $G_G^*$ .

$$\frac{K^*(\omega) - C_L G^*(\omega)}{C_R - C_L} = G_R^*(\omega) + \frac{C_G - C_L}{C_R - C_L} G_G^*(\omega) \quad (2-17)$$

$$\frac{K^*(\omega) - C_R G^*(\omega)}{C_L - C_R} = G_L^*(\omega) + \frac{C_G - C_R}{C_L - C_R} G_G^*(\omega) \quad (2-18)$$

As suggested in Figure 2-4, the third function,  $G_L^*$ , would locate between the R and G components. In other words, the difference in the relaxation time between  $G_R^*$  and  $G_G^*$  will be larger than that between  $G_R^*$  and  $G_L^*$ , and therefore I anticipate that locations of  $G_R^*$  and  $G_G^*$

might be separated enough to distinguish the two function in  $(K^*(\omega) - C_L G^*(\omega)) / (C_R - C_L)$ . In order to examine this conjecture, I sought the correct value of  $C_L$ , which gives phenomenologically reasonable  $(K^*(\omega) - C_L G^*(\omega)) / (C_R - C_L)$ . It was composed of  $G_R^*$  at low frequencies and  $G_G^*$  at high frequencies. The result is shown in Figure 2–8, which perfectly satisfies our requirements. As is indicated by the arrows, two relaxation maxima are observed. The slower relaxation can be assigned to the R component from the similarity with  $G_R^*$  in Figure 2–6. According to eq. (2–17), the faster relaxation is attributed to the glassy component,  $(C_G - C_L)G_G^*(\omega) / (C_R - C_L)$ . I note that the frequency dependence of  $(C_G - C_L)G_G^*(\omega) / (C_R - C_L)$  is very similar to the ordinary G component. To show this, I added  $G_G^*$  of PC<sub>4</sub>-BF<sub>4</sub> in Figure 2–

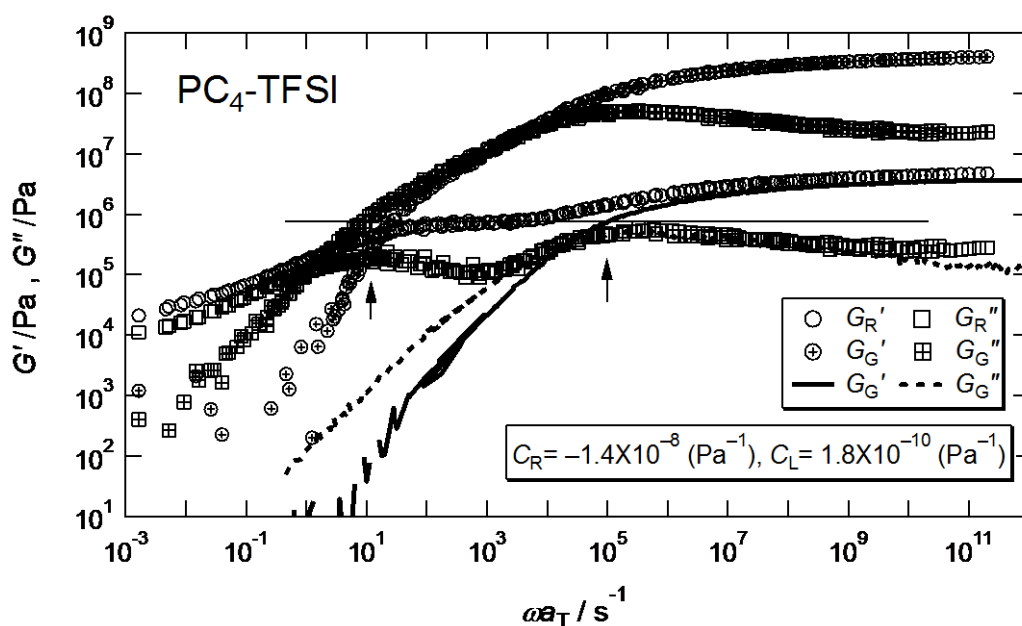


Figure 2–8. Component functions for PC<sub>4</sub>-TFSI determined by two components MSOR.

By using thus determined, coefficients  $G_R^*$ ,  $G_G^*$ ,  $C_R$ ,  $C_L$ , and  $C_G$ , I finally determined  $G_L^*$  through the eq. 2–18. The separated component function of  $G''$  for each component is shown in Figure 2–9. I note all of the real parts for the three components are a monotonically

increasing function of  $\omega$ .

Following the same consideration mentioned above, the frequency dependence of  $G^*$  for PC<sub>4</sub>-CPFSI and PC<sub>4</sub>-NfO are successfully separated into three components, R, G, and L. Figure 2–10 compared the component functions of the L mode for each PIL. The reference temperature was chosen so that the spectra were fitted each other at low frequencies for clarity. The shape of spectrum for PC<sub>4</sub>-NfO becomes sharper than those for the others.

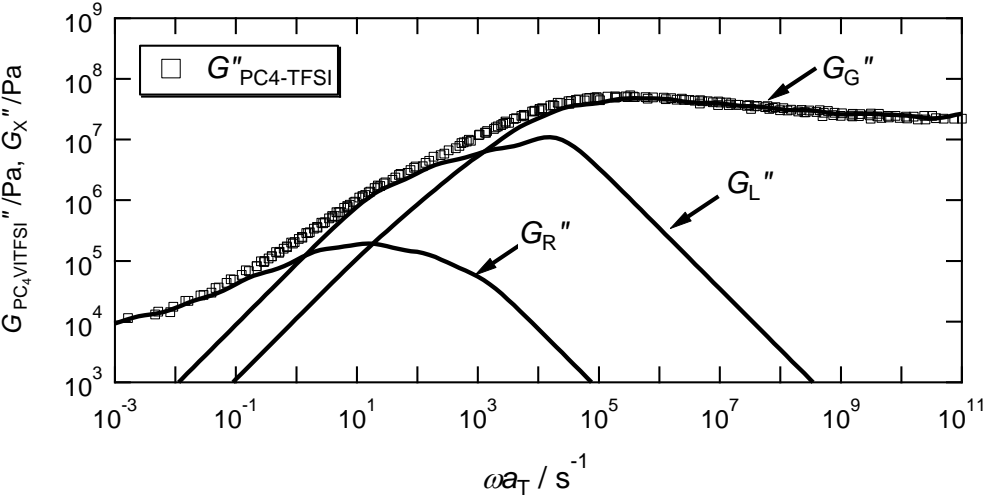


Figure 2–9. Three component functions determined by MSOR for PC<sub>4</sub>-TFSI at the reference temperature. Lines represent the component functions. Symbols represent the loss modulus from the experimental results.

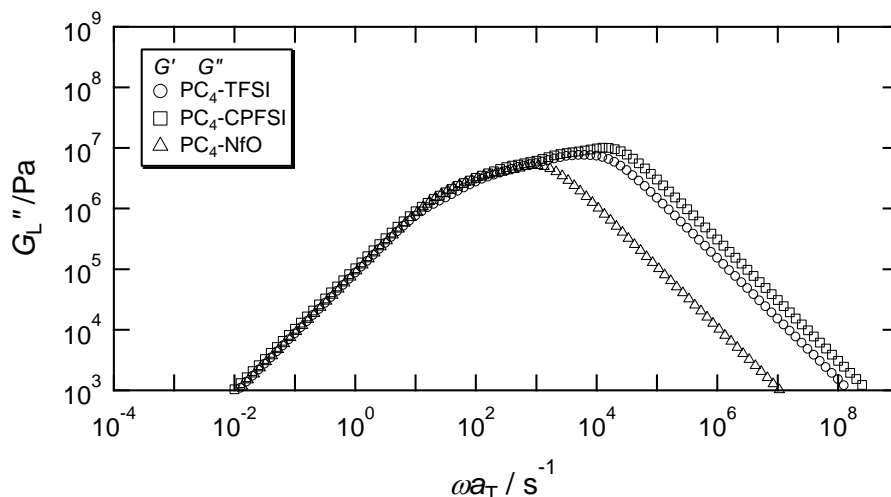


Figure 2–10. Comparison of the component functions of the L mode for PC<sub>4</sub>-TFSI, PC<sub>4</sub>-CPFSI, and PC<sub>4</sub>-NfO.

### 2–3–3 Viscoelastic Segment Size

Molar mass of viscoelastic segment,  $M_s$ , can be calculated from the limiting modulus at high frequencies for the rubbery component,  $G_R'(\infty)$ .<sup>12</sup>

$$M_s = \frac{\rho RT}{G_R'(\infty)} \quad (2-19)$$

Here,  $R$  is the gas constant,  $T$  is the absolute temperature, and  $\rho$  is density.  $RT/G_R'(\infty)$  in eq. (2–19) is the molar number of segments per unit volume, and therefore  $\rho RT/G_R'(\infty)$  corresponds to the molar mass of segments. The densities of PC<sub>4</sub>-CPFSI and PC<sub>4</sub>-NfO were assumed as  $\rho = 1.516 \text{ g cm}^{-3}$  for PC<sub>4</sub>-TFSI, and  $\rho = 1.357 \text{ g cm}^{-3}$  for PC<sub>4</sub>-TfO and  $\rho = 1.312 \text{ g cm}^{-3}$  for PC<sub>4</sub>-BF<sub>4</sub> according to the literature.<sup>2</sup> I note that eq. (2–19) is applicable irrespective of ionization state of counter ions and that the obtained value is the molar mass of segment composed of deionized repeating units. The values of  $M_s$  for each PIL is summarized in Table 2–5. In a previous study, Inoue showed that viscoelastic segment size is in agreement with the Kuhn

segment size.<sup>13</sup> The ratio,  $M_s / M_0$ , is a good measure of main chain flexibility. Here,  $M_0$  is the molar mass of repeating units. The values of  $M_s / M_0$  for PC<sub>4</sub>-TfO and PC<sub>4</sub>-BF<sub>4</sub> are close to that for PS, indicating that the dynamic rigidities of the two polymers are comparable with that of PS. On the other hand,  $M_s/M_0$  of PC<sub>4</sub>-NfO is higher than those, suggesting that PC<sub>4</sub>-NfO become more rigid than the others.

The anisotropy of the polarizability for a segment,  $\Delta\beta$ , is related to the stress-optical coefficient for the rubbery component,  $C_R$ .<sup>14</sup> The anisotropy of the polarizability for a repeating unit,  $\Delta\alpha$ , can be approximately related to  $\Delta\alpha \sim \Delta\beta M_0/M_s$ . Therefore, substituting  $\Delta\beta$  to  $\Delta\alpha$ , we can obtain the following equation.

$$\Delta\alpha = \frac{45}{2\pi} \frac{\bar{n}kT}{(\bar{n}^2 + 2)^2} \frac{M_0}{M_s} C_R \quad (2-20)$$

Here,  $\bar{n}$  denotes the refractive index of polymers in isotropic state. Assuming that the refractive index of each PIL is equal to that for PS ( $n_{PS} = 1.57$ ), the  $\Delta\alpha$  was estimated as shown in Table 2-4.

If all the repeating units are ionized,  $\Delta\alpha$  should agree with each other because  $\Delta\alpha$  is determined by the same backbone. However,  $\Delta\alpha$  for each PIL does not agree, suggesting that not all the repeating units are ionized.  $\Delta\alpha$  for PC<sub>4</sub>-TFSI is larger than others, suggesting that PC<sub>4</sub>-TFSI are highly ionized. Compared with the values of  $\Delta\alpha$  and the chemical structures of PILs, the degree of dissociation could depend on ionic size, ionic shape, and the position of charges.

Table 2–5. High limiting modulus of the R component,  $G'_R(\infty)$ , molar mass of Rouse segment,  $M_s$ , and the ratio  $M_s/M_0$ .

Sample	$G'_R(\infty)/\text{MPa}$	$M_s/\text{Kgmol}^{-1}$	$M_s / M_0$
PC <sub>4</sub> -BF <sub>4</sub>	2.5	2.0	8.4
PC <sub>4</sub> -TfO	2.1	2.4	8.0
PC <sub>4</sub> -NfO	0.33	16	36
PC <sub>4</sub> -TFSI	0.84	5.6	13
PC <sub>4</sub> -CPFSI	1.3	4.3	9.6
Polystyrene	4.0	0.86	8.2

### 2–3–4 Molecular Origin of the L Component

The stress-optical coefficient for the L component,  $C_L$ , is  $1.8 \times 10^{-10} \text{ Pa}^{-1}$  for PC<sub>4</sub>-TFSI,  $0.95 \times 10^{-10} \text{ Pa}^{-1}$  for PC<sub>4</sub>-CPFSI, and  $-0.68 \times 10^{-10} \text{ Pa}^{-1}$  for PC<sub>4</sub>-NfO. The absolute value is roughly one hundred times smaller than  $C_R$  and ten times larger than  $C_G$ , suggesting the molecular origin of the L component has relatively large compliance than the ordinary glassy modes. I note that the value of  $C_L$  is close to the stress-optical ratio for a typical ionic liquid, BmimCl,  $C_{\text{BmimCl}} = 1.8 \times 10^{-10} \text{ Pa}^{-1}$  at  $-20^\circ\text{C}$ .<sup>15</sup> (The SOR did not hold strictly for BmimCl and  $C_{\text{BmimCl}}$  defined as  $K''/G''$  varied with temperature, indicating that some structure changes occurred in BmimCl with temperature.) The similar  $C_L$  value suggests that the L component in PILs might be related to the reorientation process of ions.

$C_L$  of PILs depends on counter anion species. According to Osaki et al.,<sup>16, 17</sup> the stress-optical coefficients for the R component and the G component can be expressed in terms of the polarizability of the ellipsoid-shaped motion units.

$$C_R \propto \alpha_1 - \frac{\alpha_2 + \alpha_3}{2} \quad (2-21)$$

$$C_G \propto \frac{\alpha_2 - \alpha_3}{4} \quad (2-22)$$

Here,  $\alpha_1$  is the polarizability in the direction of main chain axis,  $\alpha_2$  is that in the direction of side chain axis, and  $\alpha_3$  is that in the tangential direction to both  $\alpha_1$  and  $\alpha_2$ . Considering that the L mode is a sort of local motions,  $C_L$  could be described in the same form as eq. (2-22). Again, if all the repeating units are ionized, the  $\alpha_2$  and  $\alpha_3$  are independent of anion species and hence  $C_L$  should agree with each other. However,  $C_L$  does not agree with each other, suggesting that not all repeating units are ionized even in the glass-to-rubber transition zone. Furthermore, the negative value of  $C_L$  for PC<sub>4</sub>-NfO indicates that NfO anions form ion pairs in which the main axis of ions aligns in perpendicular to the imidazolium side chains. In that case, the  $\alpha_3$  can become larger than the  $\alpha_2$ , resulting that the negative value of  $C_L$  for PC<sub>4</sub>-NfO is obtained.

Figure 2-10 shows that the frequency dependence of  $G_L^*$  is broad and cannot be described with a simple relaxation mode. This implies that the molecular origin of  $G_L^*$  is not a simple rotational motion of anions, which might be described with a Maxwellian function, i.e.  $N=1$  in eq. (2-23) and eq. (2-24) as shown in Figure 2-10. This result suggests that the molecular origin of  $G_L^*$  could be some cooperative motion of main chains, such as sub-Rouse motion.

From such a discussion, I examined the damped torsional oscillator model, DTO, model<sup>18</sup> proposed in order to describe the relaxation mechanism of the glassy modulus of polymers when the inter-chain interaction is weak. According to the DTO model, the complex modulus can be described as

$$G'(\omega) = G_\infty \sum_{p=1}^N \frac{\omega^2 \tau_{\text{DTO}}^2 p^{-2}}{1 + \omega^2 \tau_{\text{DTO}}^2 p^{-2}} \quad (2-23)$$

$$G''(\omega) = G_\infty \sum_{p=1}^N \frac{\omega \tau_{\text{DTO}} p^{-1}}{1 + \omega^2 \tau_{\text{DTO}}^2 p^{-2}} \quad (2-24)$$

Here,  $\tau_{\text{DTO}}$  is the longest characteristic time in the DTO model. The frequency dependence of  $G^*$  by the DTO model is similar to that of the Rouse model. The difference is the physical interpretation of the constants used in Rouse model. In DTO model, a coupled torsional oscillation of pairs or triads of bonds along the chain is considered instead of a coupled oscillation of Gaussian segments in Rouse model. Therefore, a torque constant is considered instead of a spring constant in Rouse model. As a result, the prefactor,  $G_\infty$ , has the different physical interpretation from the prefactor in Rouse model defined as  $G_\infty = cRT/M$  where  $c$  and  $M$  are the mass concentration and molecular weight of polymers, respectively. For the case that the damped torsional oscillators are arrayed linearly, the inter-chain interaction is ignored and the dynamics are governed by the connectivity of the chain. Similar frequency dependence was obtained by Verdier-Stockmayer model.<sup>19, 20</sup> In this model, the polymer is made up of  $N$  beads connected by  $N-1$  bonds having the same bond length. Local motions of polymers are represented by the jump of beads with a probability. This probability is not affected by the inter-chain interaction.

In Figure 2–10, the loss modulus,  $G''$ , by the DTO model is compared with that for the L component of PC<sub>4</sub>-TFSI. The prediction of the DTO model is remarkably consistent with the experimental data in low frequency side of  $G''$  maximum. Thus, the L mode can be attributed to the reduction of the inter-chain cooperation. In the fitting procedure, I assumed that the  $G_\infty$  in the DTO model is equal to  $cRT/M_L$ . The obtained fitting parameters are summarized in Table 2–6. The cooperative size of the L mode,  $M_L$ , for each PIL is comparable to the viscoelastic segment sizes determined by the global motion of chain. Moreover, the molar mass of the smallest motion unit for the L mode estimated by  $M_L/N$  is smaller than that for the repeating

units, indicating that the L mode originates from the local motions of polymer chains.

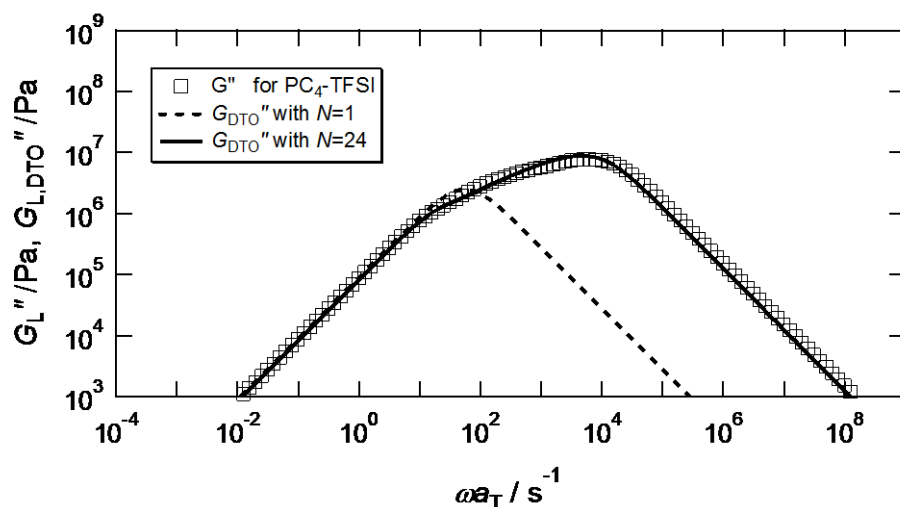


Figure 2-11. Comparison of the frequency dependence of  $G''$  between the L component for PC<sub>4</sub>-TFSI and the prediction of the DTO model with  $N=24$  and  $M_L = 4000$ .

Table 2-6. Fitting parameters of the DTO model for PC<sub>4</sub>-TFSI, PC<sub>4</sub>-CPFSI, and PC<sub>4</sub>-NfO.

	PC <sub>4</sub> -TFSI	PC <sub>4</sub> -CPFSI	PC <sub>4</sub> -NfO
$N$	24	30	7
$M_L / 10^3 \text{g mol}^{-1}$	4.0	4.1	3.0
$\tau_{\text{DTO}} / \text{s}$	0.05	0.05	0.00003

For PC<sub>4</sub>-TFSI, the TFSI ions are highly ionized and occupy the half of the volume. Thus, if TFSI anions work as a solvent, the inter-chain interaction is diminished, resulting that dynamics are governed by the connectivity of the chain.

For PC<sub>4</sub>-CPFSI, the CPFSI anions are less ionized because the value of  $\Delta\alpha$  for PC<sub>4</sub>-CPFSI shown in Table 2-4 is smaller than that for PC<sub>4</sub>-TFSI. However, the L mode was observed in the PC<sub>4</sub>-CPFSI system. This could be explained by the comparison of the ionic shapes between TFSI and CPFSI anions. As shown in Table 2-3, the CPFSI anions have the

round-shaped structure while the TFSI anions have the ellipsoid-shaped structure. In this case, the friction drag of CPFISI ions could be weaker than that of TFSI ions. Therefore, once ions are ionized, the plasticizing effect of CPFISI ions is observed. Thus, the mode distribution of the L mode for PC<sub>4</sub>-CPFISI becomes similar to that for PC<sub>4</sub>-TFSI even though the CPFISI ions are less ionized than TFSI ions.

For PC<sub>4</sub>-NfO, the NfO anions are elliptic and are less ionized, resulting into the higher rigidity of chains. It could be one of the causes for the loss of inter-chain cooperation. Inoue<sup>13</sup> has shown that the ratio,  $M_s / M_0$ , is related to the characteristic ratio of polymers,  $C_\infty$ .

$$\frac{M_s}{M_0} \approx \frac{M_K}{M_0} = \frac{\langle R \rangle^2}{R_{\max}^2} \propto C_\infty \quad (2-25)$$

The large value of  $C_\infty$  implies the strong intra-chain interplay between structural units. As shown in Table 2-5, the ratio,  $M_s / M_0$ , for PC<sub>4</sub>-NfO is four times as large as that for PC<sub>4</sub>-TFSI, indicating that the intra-chain interaction is dominant for chain motions of PC<sub>4</sub>-NfO. Thus, the L mode was observed in the PC<sub>4</sub>-NfO system. The higher rigidity of PC<sub>4</sub>-NfO is caused by the larger rotational hindrance of chain backbones having deionized larger NfO anions. The difference in origins might give rise to the difference in the mode distribution of the L mode.

## 2-4 Conclusion

I employed the rheo-optical measurements for five poly(1-butyl-3-vinylimidazolium)-based ionic liquids, PC<sub>4</sub>-BF<sub>4</sub>, PC<sub>4</sub>-TfO, PC<sub>4</sub>-NfO, PC<sub>4</sub>-TFSI, and PC<sub>4</sub>-TFSI in order to clarify the molecular origin of broad spectra in the vicinity of the glass-to-rubber transition zone. For PC<sub>4</sub>-BF<sub>4</sub> and PC<sub>4</sub>-TfO, the two component MSOR worked well and reasonable two component functions were obtained. In contrast, for PC<sub>4</sub>-TFSI, PC<sub>4</sub>-CPFISI, and PC<sub>4</sub>-NfO having larger

counterions, three component functions were needed. These three component functions were assigned to the segmental reorientation mode, the sub-Rouse mode, and the glassy mode. The sub-Rouse mode is often observed in polymer solutions where intra-chain interaction is dominant for local motions. It was that the intra-chain interplay on the dynamics of polymer chains for PILs became dominant with increasing ionic sizes of anions. For PC<sub>4</sub>-TFSI and PC<sub>4</sub>-CPFSI, the inter-chain interaction is diminished by the plasticizing effect of counterions. The ionized ions could work as solvent molecules. For PC<sub>4</sub>-NfO, the intra-chain interaction is increased by the rotational hindrance of chain backbones having deionized NfO anions.

## 2-5 References

- (1) Nakamura, K.; Saiwaki, T.; Fukao, K.; Inoue, T. *Macromolecules* **2011**, 44, 7719-7726.
- (2) Nakamura, K.; Fukao, K.; Inoue, T. *Macromolecules* **2012**, 45, 3850-3858.
- (3) Mecerreyes, D. *Prog. Polym. Sci.* **2011**, 36, 1629-1648.
- (4) Hayashi, C.; Inoue, T. *Nihon Reoroji Gakk* **2009**, 37, 205-210.
- (5) Inoue, T. O., H.; Hayashihara, H.; Osaki, K. *Nihon Reoroji Gakk* **1991**, 19, 93.
- (6) Schroter, K.; Hutcheson, S. A.; Shi, X.; Mandanici, A.; McKenna, G. B. *J. Chem. Phys.* **2006**, 125.
- (7) Hutcheson, S. A.; McKenna, G. B. *J. Chem. Phys.* **2008**, 129.
- (8) Osaki, K.; Inoue, T.; Uematsu, T. *J Polym Sci Pol Phys* **2000**, 38, 3271-3276.
- (9) Okamoto, H.; Inoue, T.; Osaki, K. *J Polym Sci Pol Phys* **1995**, 33, 1409-1416.
- (10) Takiguchi, O. I., T.; Osaki, K. *Nihon Reoroji Gakk* **1995**, 23, 13.
- (11) Inoue, T.; Onogi, T.; Osaki, K. *J Polym Sci Pol Phys* **2000**, 38, 954-964.
- (12) Inoue, T.; Osaki, K. *Macromolecules* **1996**, 29, 1595-1599.
- (13) Inoue, T. *Macromolecules* **2006**, 39, 4615-4618.
- (14) Kuhn, W.; Grun, F. *Kolloid Z.* **1942**, 101, 248.
- (15) Maeda, A.; Inoue, T.; Sato, T. *Macromolecules* **2013**, 46, 7118-7124.
- (16) Osaki, K.; Okamoto, H.; Inoue, T.; Hwang, E. J. *Macromolecules* **1995**, 28, 3625-3630.
- (17) Inoue, T. *Nihon Reoroji Gakk* **2000**, 28, 167-175.
- (18) Tobolsky, A. V.; Aklonis, J. J. *J. Phys. Chem.* **1964**, 68, 1970.
- (19) Verdier, P. H.; Stockmayer, W. H. *J. Chem. Phys.* **1962**, 36, 227-&.
- (20) Doi, M.; Edwards, S. F., *The Theory of Polymer Dynamics*. Clarendon: Oxford, 1986; p 391.

---

## CHAPTER 3

# Counter Ion-Induced Ordered Structure of a Polymerized Ionic Liquids in Bulk

---

### 3-1 Introduction

In chapter 2, we have seen how characteristics of counter anions affect viscoelastic and dielectric properties of polymerized ionic liquids (PILs). The volume ratio,  $V_r = V_a / V_c$ , of an anion,  $V_a$ , and a cation,  $V_c$ , is likely one of important parameters determining the viscoelastic properties, and it is still a challenge to understand the effects of  $V_r$  in terms of molecular dynamics for the case that  $V_r$  is larger than unity. As I mentioned in chapter 1, Nakamura et al.<sup>1, 2</sup> proposed the presence of ionic aggregates in poly(1-ethyl-3-vinylimidazolium bis(trifluoromethanesulfonylimide)) (PC<sub>2</sub>-TFSI). On the other hand, such aggregates were not observed in poly(1-butyl-3-methylimidazolium bis(trifluoromethanesulfonylimide)) (PC<sub>4</sub>-TFSI).<sup>2</sup> This study supports that  $V_r$  is the parameter to determine viscoelastic properties of PILs. The  $V_r$  for PC<sub>4</sub>-TFSI is 0.96 whereas the  $V_r$  for PC<sub>2</sub>-TFSI is 1.2. The ionic aggregates could be formed due to the weak steric hindrance resulting from the shorter alkyl chains.

One of possible approaches to achieve  $V_r$  higher than unity is introducing perfluoroalkyl chains on counter anions of PILs. Accordingly, a series of poly(1-butyl-3-vinylimidazolium bis(perfluoroalkylsulfonyl)imide) were synthesized. Figure 3-1 shows the chemical structures of repeating units of cations and anions used in this chapter. In order to evaluate the effects of counter anion sizes on structural changes and viscoelastic properties, the similar chemical structures are used.

In this chapter, a unique ordered structure observed in a polymerized ionic liquid is investigated using polarization microscopy, UV/VIS spectroscopy, X-ray scattering, differential

scanning calorimetry, thermal gravimetry, and viscoelastic measurements.

### 3-2 Experimental Methods

**Materials.** Lithium bis(heptafluoropropanesulfonyl)imide (LiHFSI) was purchased from Wako Pure Chemicals. Lithium bis(pentafluoroethanesulfonyl)imide (LiPFSI) was purchased from Kishida Chemical. These materials were used as received.

**Synthesis.** Figure 3-1 shows the chemical structures of cations and anions examined in this chapter. The syntheses of PC<sub>4</sub>-PFSI and PC<sub>4</sub>-HFSI were carried out by the same procedure as described in Chapter 2. The 1-butyl-3-vinylimidazolium cations were chosen as polyions. The molar ratio of the monomer to initiator,  $M_M/M_I$ , the molar ratio of salts to structural units of PC<sub>4</sub>-Br,  $M_{SA}/M_P$ , are summarized in Table 3-1. The results of elemental analysis are also summarized in Table 3-1. Consequently, the exchange ratio from the bromide ions to the aimed anions was almost 100%.

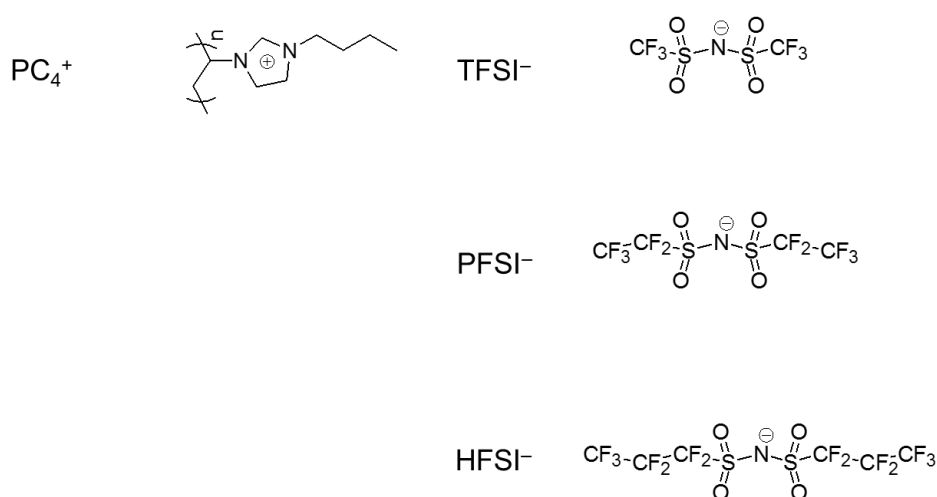


Figure 3-1. Chemical structures of cations and anions.

Table 3–1. Molar ratios,  $M_M/M_I$  and  $M_{SA}/M_P$ , and weight fraction of elements for the products by elemental analysis.

Sample Code	$M_M/M_I$	$M_{SA}/M_P$	C /wt%	H /wt%	N /wt%
PC <sub>4</sub> -PFSI	98.9	1.52	29.47 (29.38)	2.80 (2.85)	7.86 (7.91)
PC <sub>4</sub> -HFSI	98.9	2.55	28.43 (39.99)	2.30 (5.04)	6.75 (6.66)

( ): Theoretical values

The van der Waals volume of each ion was estimated using the Winmostar version 6.018 software and the values are listed in Table 3–2. The volume ratios  $V_{fs}$  are 0.96 for PC<sub>4</sub>-TFSI, 1.3 for PC<sub>4</sub>-PFSI, and 1.6 for PC<sub>4</sub>-HFSI.

Table 3–2. Van der Waals volume  $V$  for each ion.

	C <sub>4</sub> <sup>+</sup>	TFSI <sup>-</sup>	PFSI <sup>-</sup>	HFSI <sup>-</sup>
$V/\text{nm}^3$	0.154	0.148	0.201	0.254

**Sample Preparation.** As explained later, the structure and physical properties of PILs were strongly affected by the preparation history. Firstly, each acetone solution of PC<sub>4</sub>-TFSI, PC<sub>4</sub>-PFSI, and PC<sub>4</sub>-HFSI was cast onto a Teflon Petri dish. After slow evaporation of the solvent, the resultant plane films were dried under vacuum overnight at 70°C. Prefix "c-" is used for as-cast samples such as c- PC<sub>4</sub>-TFSI to distinguish the preparation history. The as-cast films were then molded into thin films using a hot press without a spacer at 150°C for PC<sub>4</sub>-TFSI and at 180°C for PC<sub>4</sub>-PFSI and PC<sub>4</sub>-HFSI, respectively. Prefix "h-" is used for samples molded with press. The obtained thin films with a thickness of 0.051 mm for h-PC<sub>4</sub>-TFSI and 0.14 mm for h-PC<sub>4</sub>-PFSI and h-PC<sub>4</sub>-HFSI were used for thermal gravimetry, X-ray scattering measurements,

and the observation of morphologies using a polarization microscope. Then, these thin films were molded into sheets using the hot press for 15 min with a 1.0 mm spacer at 150°C for PC<sub>4</sub>-TFSI and at 180°C for PC<sub>4</sub>-PFSI and PC<sub>4</sub>-HFSI. The resultant thicker sheets (also with prefix "h-") were used for DSC and viscoelastic measurements. For comparison, the as-cast sheets with a thickness of 0.16 mm for *c*-PC<sub>4</sub>-TFSI, 0.11 mm for *c*-PC<sub>4</sub>-PFSI, and 0.064 mm for *c*-PC<sub>4</sub>-HFSI were prepared from the acetone solutions of the PILs. The samples for PC<sub>4</sub>-TFSI were used after annealing at 70°C for 9 h. The samples for PC<sub>4</sub>-PFSI and PC<sub>4</sub>-HFSI were used after annealing at 150°C for 9 h.

Moreover, a 30 wt% 1-butyl-3-vinylimidazolium bis(pentafluoroethanesulfonyl)imide (BmimPFSI) solution of PC<sub>4</sub>-PFSI was prepared via co-solvent method in order to compare the morphologies between in the solution and bulk systems. A mixture of BmimPFSI and PC<sub>4</sub>-PFSI dissolved into acetone was slowly dried at room temperature and then the solution was dried at 65°C under vacuum for a week until complete evaporation of acetone. BmimPFSI was chosen as the solvent to evaluate morphologies in the same condition as PC<sub>4</sub>-PFSI where the system is composed of only ions.

## ***Methods.***

### **a) Structural Analysis.**

*Polarization Microscopy:* Direct observation of ordered structures was performed by polarized light microscopy using an ECLPSE E400 (Nikon) equipped with a digital camera. A piece of sheet of each PIL was placed onto a slide glass. Micrographs in the crossed Nicol condition were taken for the samples under controlling temperatures using a FP80 (Mettler Toledo Inc.). For the 30 wt% PC<sub>4</sub>-PFSI/BmimPFSI solution system, the viscous liquid was placed onto a slide glass and then spread with a cover glass into a thickness of 0.23 mm.

*Polarization Imaging:* The extinction angle,  $\chi$ , and the birefringence,  $\Delta n$ , were measured using the method reported recently by Inoue et al.<sup>3</sup> A piece of film of *h*-PC<sub>4</sub>-PFSI was mounted onto the sample stage of the polarization microscopy equipped with a polarization imaging camera (PI-110, Phonic Lattice). The circularly polarized inductive light is converted its polarization through the sample, and then the transmitted light is detected using the polarization imaging camera.<sup>3</sup>

*UV/VIS Spectroscopy:* The  $\Delta n$  was also measured using the multi-wavelength method proposed by Hongladarom et al.<sup>4</sup> In the experiment, the linearly polarized light with a wavelength range of 250–800 nm was induced into a sample film, and then the intensity of transmitted light,  $I$ , was detected in the crossed Nicol ( $\perp$ ) or parallel Nicol ( $\parallel$ ) conditions using a Lambda 750 UV/VIS spectrometer (PerkinElmer).

*X-ray Scattering:* Wide- and small-angle X-ray scattering measurement were respectively conducted with a Rigaku DMAX/rapid microdiffractometer and with a Rigaku NANO Viewer at room temperature. For the SAXS measurement, 2–10 pieces of thin film was piled up to obtain sufficient intensity. The profiles with a scattering vector,  $q \equiv 4\pi\sin\theta/\lambda_x$ , ranging from 0.04 nm<sup>-1</sup> to 1 nm<sup>-1</sup> for *h*-PC<sub>4</sub>-TFSI, *h*-PC<sub>4</sub>-PFSI, and *h*-PC<sub>4</sub>-HFSI were collected using a PILATUS 100 K (DECTRIS) detector with a camera length of 1.3 m. All the data were corrected with the sample transmittance and the background intensity.

## **b) Thermal Analysis.**

*Differential Scanning Calorimetry:* The glass transition temperature,  $T_g$ , and the change of heat capacity during the glass transition,  $\Delta c_p$ , were determined using an EXSTAR6000 (Hitachi High-Tech Science Corporation). The sample films of 11.08 mg for *c*-

PC<sub>4</sub>-TFSI, 12.65 mg for *h*-PC<sub>4</sub>-PFSI, 9.28 mg for *c*-PC<sub>4</sub>-PFSI, 12.53 mg for *h*-PC<sub>4</sub>-HFSI, and 11.43 mg for *c*-PC<sub>4</sub>-HFSI were annealed in open pans under vacuum at 150°C for 9 h before being hermetically sealed. Temperature ramps cycled from 300°C to –10°C with cooling and heating rates of 10 °C / min.

*Thermal Gravimetry:* The thermal decomposition temperature,  $T_d$ , was determined using a STA 6000 (PerkinElmer). The sample films of 4.04 mg for *h*-PC<sub>4</sub>-PFSI, 4.40 mg for *c*-PC<sub>4</sub>-PFSI, and 7.80 mg for *h*-PC<sub>4</sub>-HFSI were placed onto alumina cups, and then was heated up from 30 °C to 600 °C with a heating rate of 10 °C/min under nitrogen atmosphere.

**c) Dynamic Viscoelasticity.** Dynamic linear viscoelastic measurements of *h*-PC<sub>4</sub>-PFSI, *c*-PC<sub>4</sub>-PFSI, and *h*-PC<sub>4</sub>-HFSI were carried out using a DVE-V3 rheospectra (Rheology co., Ltd) under oscillatory tensile deformation ( $\varepsilon < 0.04\%$ ) in a temperature range of 35 – 180 °C. The sample sheets for *h*-PC<sub>4</sub>-PFSI and *h*-PC<sub>4</sub>-HFSI having a strip shape of 20 × 6 × 1 mm were cut off away from the center of a 1 mm thickness of hot press molded films. As for the measurement of *c*-PC<sub>4</sub>-PFSI, three pieces of film with a strip shape of 20 × 5 × 0.1 mm were piled up and then attached to the apparatus. The complex Young's modulus,  $E^*$ , was measured in a frequency range of 1–130 Hz under a nitrogen atmosphere. On the other hand, the linear viscoelastic measurement for *h*-PC<sub>4</sub>-TFSI was conducted on an ARES-G2 (TA instruments) rheometer under oscillatory shear deformation ( $\gamma = 0.01 - 30\%$ ) with a temperature range of 35 – 200 °C. The complex shear modulus,  $G^*$ , was measured using a homemade parallel plate fixture having a 4 mm diameter in a frequency range of 0.1 – 100 rad s<sup>-1</sup> under a nitrogen atmosphere. In what follows, I will not distinguish  $3G^*$  and  $E^*$  unless otherwise noted.

**d) Stress Relaxation.** The stress relaxation test for *h*-PC<sub>4</sub>-PFSI was conducted using the

ARES-G2 (TA instruments) rheometer with a torsion fixture under the condition of a strain amplitude  $\gamma = 0.005$  at  $T = 180^\circ\text{C}$ . The relaxation modulus was measured for  $4.0 \times 10^4$  s

**e) Oscillatory Tensile-Induced Birefringence.** The frequency dependence of strain-induced birefringence,  $\Delta n^*(\omega)$ , and that of stress,  $\sigma_E^*(\omega)$ , of *c*-PC<sub>4</sub>-PFSI under oscillatory small tensile deformation was measured using the same handmade apparatus mentioned in Chapter 2.  $O^*$  and  $E^*$  were determined in a temperature range of 60 – 180 °C with a frequency range of 1–130 Hz.

### 3–3 Results and Discussion

#### 3–3–1 Micrographs

Figure 3–2 (a) shows the micrograph of *h*-PC<sub>4</sub>-TFSI. This image is optically isotropic and homogeneous, indicating that *h*-PC<sub>4</sub>-TFSI is amorphous at room temperature. In contrast, the micrographs shown in Figure 3–2 (b) for *h*-PC<sub>4</sub>-PFSI and in Figure 3–2 (c) for *h*-PC<sub>4</sub>-HFSI are bright and marmoreal, indicating the presence of a sort of ordered structures. The structural change was observed when introducing the counter anions having ionic sizes larger than those of polycations.

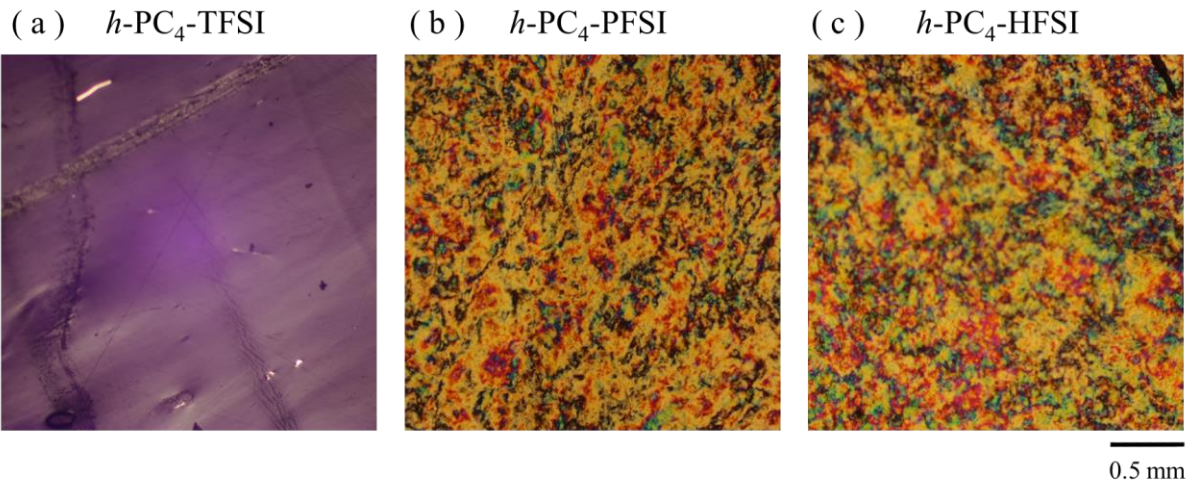


Figure 3–2. Polarization microscope images of (a) *h*-PC<sub>4</sub>-TFSI, (b) *h*-PC<sub>4</sub>-PFSI, and (c) *h*-PC<sub>4</sub>-HFSI at room temperature.

However, as shown in Figures 3–3 (a), (b), and (c), the ordered structures were not observed in the as-cast sheets for each PIL. These images are optically isotropic and homogeneous, compared with the images of *h*-PC<sub>4</sub>-PFSI and *h*-PC<sub>4</sub>-HFSI. We found that the structures were strongly affected by the preparation history.

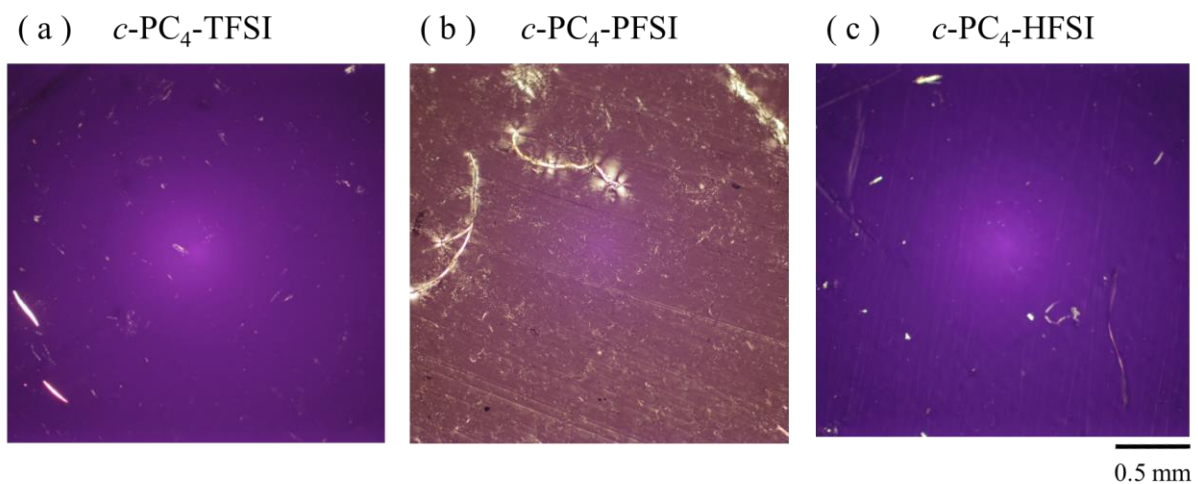


Figure 3–3. Polarization microscope images of (a) *c*-PC<sub>4</sub>-TFSI, (b) *c*-PC<sub>4</sub>-PFSI, and (c) *c*-PC<sub>4</sub>-HFSI at room temperature.

The formation of ordered structures such as crystals and liquid crystals is known to be sensitive to concentration of polymers and applied temperatures.<sup>5-9</sup> Figure 3–4 shows the micrograph of the PC<sub>4</sub>-PFSI/BmimPFSI 30 wt% solution. This image is optically isotropic and homogeneous. The ordered structure was not observed for PC<sub>4</sub>-PFSI at relatively low concentration.

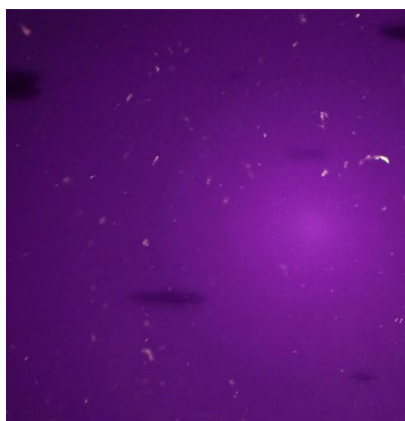


Figure 3–4. Polarization microscope image of the 30 wt% 1-butyl-3-methylimidazolium bis(pentafluoroethanesulfonyl)imide (BmimPFSI) solution of PC<sub>4</sub>-PFSI.

In order to evaluate structural growths and melting processes of observed ordered structure in PIL systems, three types of thermal treatments, the stepwise temperature increment test (STI), the temperature sweep test (TempSw), and the time sweep test (TimeSw) at a constant temperature were conducted under nitrogen atmosphere and the morphologies of several temperatures and times were observed.

Figure 3–5 (a) shows the result of STI test for *h*-PC<sub>4</sub>-PFSI. A piece of film was placed onto the hot stage after reaching 473K. The ordered structure is preserved up to 523 K and subsequently disordering processes seem to occur at some time after reaching 553 K. In order to evaluate more accurate disordering temperature, I conducted the TempSw test at a heating rate of 1 K / min in a range of 553 – 573 K. The sample film was mounted onto the heat stage

after reaching 553 K. As shown in Figure 3–5 (b), the disordering process was observed at 568 K. However, as will be shown below in the TG-DSC traces of Figure 3–6, this breakdown could be caused by the thermal decomposition of *h*-PC<sub>4</sub>-PFSI. Figure 3–5 (c) shows the result of TimeSw test for *c*-PC<sub>4</sub>-PFSI. Structural changes such as the structural growth were not observed at 523K for 115 min. This temperature is much higher than  $T_g$  for *h*-PC<sub>4</sub>-PFSI. As will be discussed below in Figure 3–9 and Figure 3–10, the thermal stability of ordered structures can be caused by the restriction of segmental motion of polymer chains.

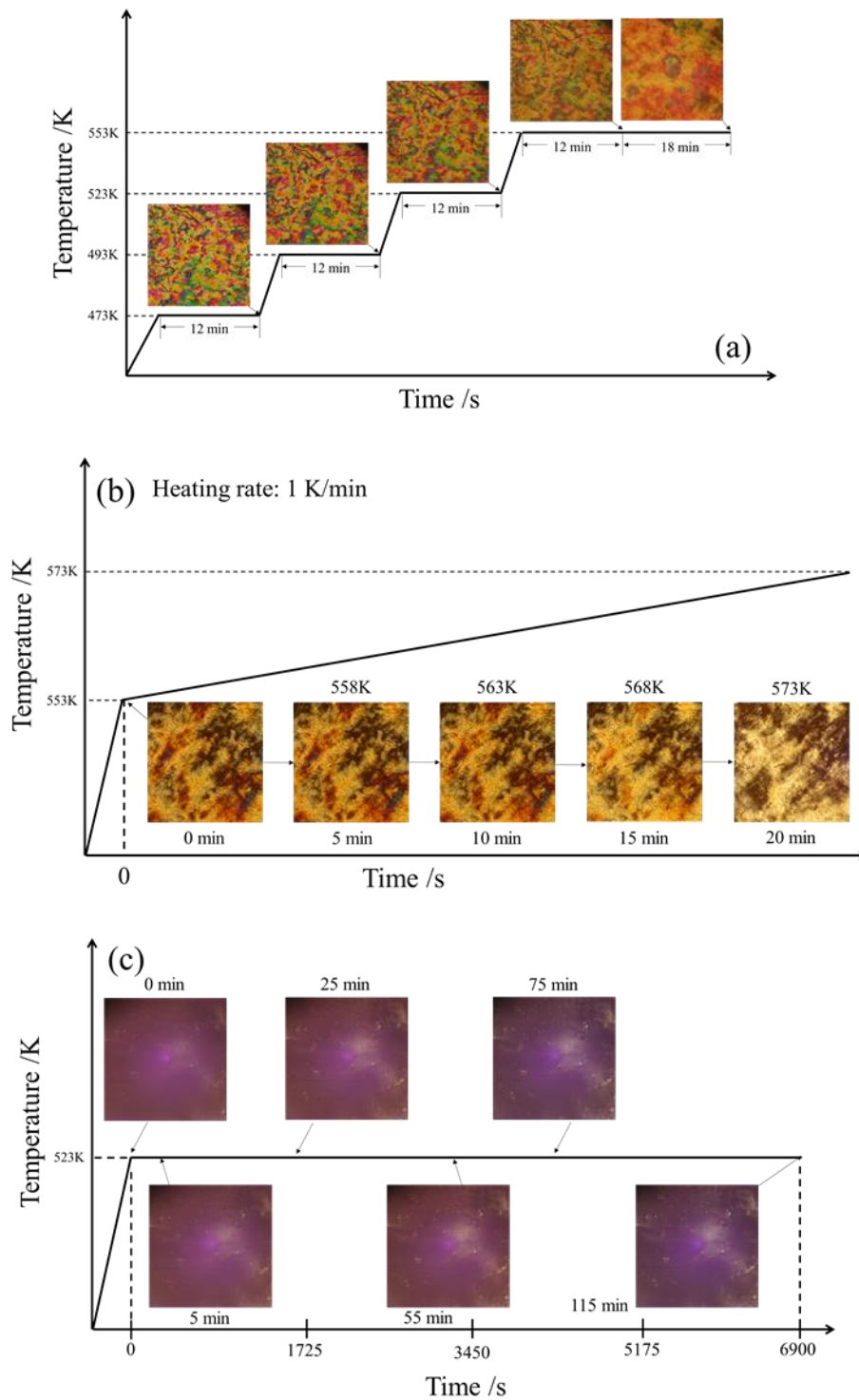


Figure 3–5. The micrographs at given temperatures and times obtained from the tests: (a) the stepwise temperature increment test for *h*-PC<sub>4</sub>-PFSI, (b) the temperature sweep test at a heating rate of 1 K/min for *h*-PC<sub>4</sub>-PFSI, and (c) the time sweep test at 523 K for *c*-PC<sub>4</sub>-PFSI.

Since PC<sub>4</sub>-PFSI and PC<sub>4</sub>-HFSI are composed of only ions, the ordered structures can be formed by ionic arrays. Therefore, the notation of “ionic array” is used for the ordered structure hereafter. Several structural characteristics can be considered as factors to form the ionic arrays observed in *h*-PC<sub>4</sub>-PFSI and *h*-PC<sub>4</sub>-HFSI.

From the rheological studies in Chapter 2, where the intra-chain cooperativity became strong with increasing the ionic sizes of anions, the polymer chains could become more rigid like semi-flexible polymers. In such a discussion, the rod-like segments was speculated to be capable of forming ionic arrays. Furthermore, the orientation directions of counter anions may be attributed to the difference in morphology depending on the preparation methods. For the films prepared by the solvent cast method, the randomly oriented counter anions may hinder chains from forming ordered structures with lengths enabling us to observe using a microscope.

These ionic arrays could be stabilized the cohesive force of perfluoroalkyl chains and the electrostatic interaction between cations and anions. Pereiro et al.<sup>10</sup> reported that ionic liquids haing longer perfluoroalkyl chains exhibit the nanostructured domain due to the segregation of fluorinated units. Therefore, the fluoroalkyl chains on PFSI and HFSI anions could play a role to form ionic arrays though the lengths are relatively short. Furthermore, as mentioned in Chapter 1, the ionic aggregates tend to be formed due to the weak steric hindrance of alkyl chains on cations resulting from the larger counter anions than cations. However, further investigations are required to clarify the precise molecular mechanism to form the ionic arrays.

### **3-3-2 Thermal Characterization**

Figure 3-6 (a) shows TG traces of *h*-PC<sub>4</sub>-PFSI, *c*-PC<sub>4</sub>-PFSI, and *h*-PC<sub>4</sub>-HFSI in a temperature range of 25 – 600 °C. In the plots, the sample weight, *W*, was normalized by the initial sample weight, *W*<sub>0</sub>, of each PIL. The onset of weight decrement due to the thermal

decomposition for each PIL was observed at around 350 °C.

Figure 3–6 (b) compares the DSC traces of *h*-PC<sub>4</sub>-PFSI and *c*-PC<sub>4</sub>-PFSI. None of phase transitions besides that related to the glass transition temperatures at around 50 °C was observed. This result indicates that the morphology in PC<sub>4</sub>-PFSI does not experience any thermal events up to high temperatures where thermal decomposition occurs. Similar temperature dependence of heat capacity was observed for *h*-PC<sub>4</sub>-HFSI and *c*-PC<sub>4</sub>-TFSI.

As shown in Figure 3–6 (c) and Table 3–3, the  $T_g$  values are almost the same between four PIL films irrespective of the preparation methods. On the other hand, there is the difference in  $\Delta c_p$ ; The  $\Delta c_p$  for PC<sub>4</sub>-PFSI and PC<sub>4</sub>-HFSI is half as high as that for PC<sub>4</sub>-TFSI while there is no significant difference in  $\Delta c_p$  between the sample films prepared by hot press molding and solvent cast method. The low  $\Delta c_p$  values suggests that chain motions of *h*- or *c*- PC<sub>4</sub>-PFSI and *h*-PC<sub>4</sub>-HFSI are restricted.

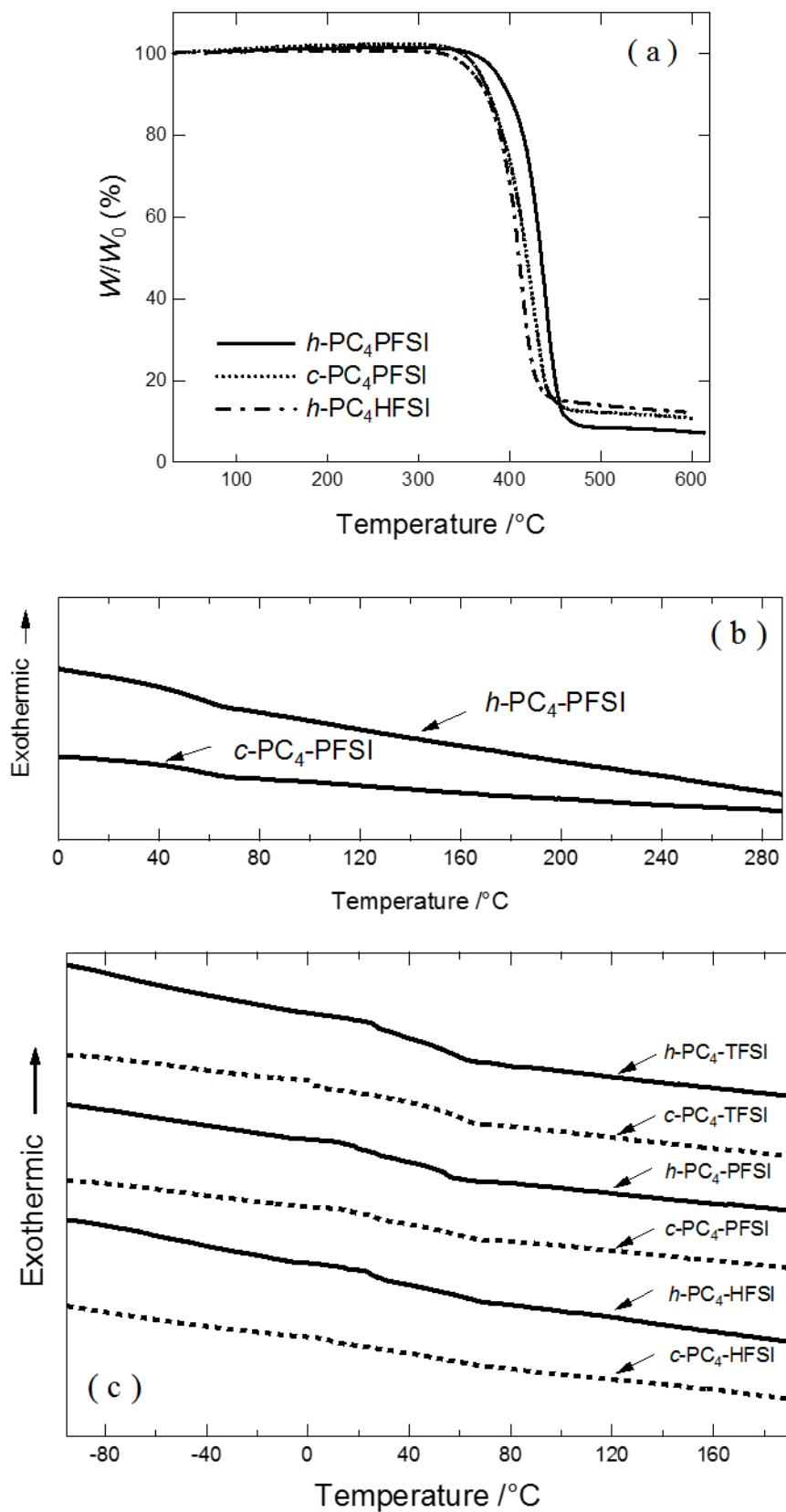


Figure 3-6. (a) TG traces of  $h\text{-PC}_4\text{-PFSI}$ ,  $c\text{-PC}_4\text{-PFSI}$ , and  $h\text{-PC}_4\text{-HFSI}$ . (b) DSC traces of  $h\text{-PC}_4\text{-PFSI}$  and  $c\text{-PC}_4\text{-PFSI}$ . (c) DSC traces for all PILs.

Table 3–4. Glass transition temperature  $T_g$  and change of heat capacity during the glass transition  $\Delta c_p$ .

Sample code	$T_g$ °C	$10\Delta c_p$ J K <sup>-1</sup> kg <sup>-1</sup>	<i>Ordered Structure</i>
<i>h</i> -PC <sub>4</sub> -TFSI	49.8	28.7	×
<i>c</i> -PC <sub>4</sub> -TFSI	53.0	29.8	×
<i>h</i> -PC <sub>4</sub> -PFSI	52.0	11.9	○
<i>c</i> -PC <sub>4</sub> -PFSI	54.3	10.9	×
<i>h</i> -PC <sub>4</sub> -HFSI	41.2	11.0	○
<i>c</i> -PC <sub>4</sub> -HFSI	48.0	10.2	×

### 3–3–3 Birefringence and Extinction Angle

In case that linearly polarized light enters through a birefringent material with the extinction angle,  $\chi$ , and retardation,  $R$  ( $\equiv d \times \Delta n$ ), the intensity of transmitted light ( $I^\perp$  and  $I^\parallel$ ) can be related with  $\chi$  and phase shift,  $\delta$  ( $\equiv 2\pi R/\lambda$ ) as

$$N^\perp = \frac{I^\perp}{I^\perp + I^\parallel} = \sin^2 2\chi \sin^2 \left( \frac{\delta}{2} \right) \quad (3-1)$$

$$N^\parallel = \frac{I^\parallel}{I^\perp + I^\parallel} = 1 - \sin^2 2\chi \sin^2 \left( \frac{\delta}{2} \right) \quad (3-2)$$

where,  $N^\perp$  and  $N^\parallel$  are the normalized intensity of light perpendicular and parallel to the polarization direction of the incident light, respectively.  $d$  denotes the thickness of sample film and  $\lambda$  is the wavelength of light.

In the case of multi-wavelength method,<sup>4</sup>  $\Delta n$  can be calculated as

$$\Delta n = \frac{1}{d} \left( \frac{\lambda_2 \lambda_1}{\lambda_2 - \lambda_1} \right) \quad (3-3)$$

Here,  $\lambda_1$  and  $\lambda_2$  are the wavelengths where periodic intensity of  $N^\perp$  and  $N^\parallel$  takes the minimum values with a distance of one period.

Figure 3–7 (a) shows the wavelength dependence of  $N^\perp$  and  $N^\parallel$  for  $h$ -PC<sub>4</sub>-PFSI. The spectra are relatively flat and obvious sine waves are not observed in the whole measurement wavelength range, suggesting that the retardation from a refractive ellipsoid is cancelled out by the distribution of  $\chi$ , which leads to depolarization. As the result, the ionic array cannot be characterized with macroscopic birefringence measurements. The orientational direction can be observed using the method reported recently by Inoue et al.<sup>3</sup>

Figure 3–7 (b) and 3–7 (c) respectively show the obtained distribution image of  $\chi$  in an angle range of 0 to  $\pi/2$  and that of  $\Delta n$  in an intensity range of 0.00001–0.001 taken by the polarization imaging camera. As found in their histogram of the  $\chi$  and the  $\Delta n$ , the ionic array in  $h$ -PC<sub>4</sub>-PFSI is oriented in various three dimensional directions. Here, we set the angle range of  $\chi$  from 0 to  $\pi/2$  because we cannot distinguish the extinction angle  $\chi$  from  $\chi + \pi/2$  when materials have large unknown values of  $\Delta n$ . Therefore, the obtained values of  $\chi$  ranging from  $-\pi/2$  to 0 were corrected by  $+\pi/2$  since the measurable range of this apparatus is from  $\chi = -\pi/2$  to  $\chi = \pi/2$ . The precise values of  $\chi$  can be obtained by using a sample film having a much thinner thickness but it is not realistic. Consequently, further experiments such as uniaxial deformation test are needed in order to reveal the precise value of  $\Delta n$  for the ionic array in  $h$ -PC<sub>4</sub>-PFSI.

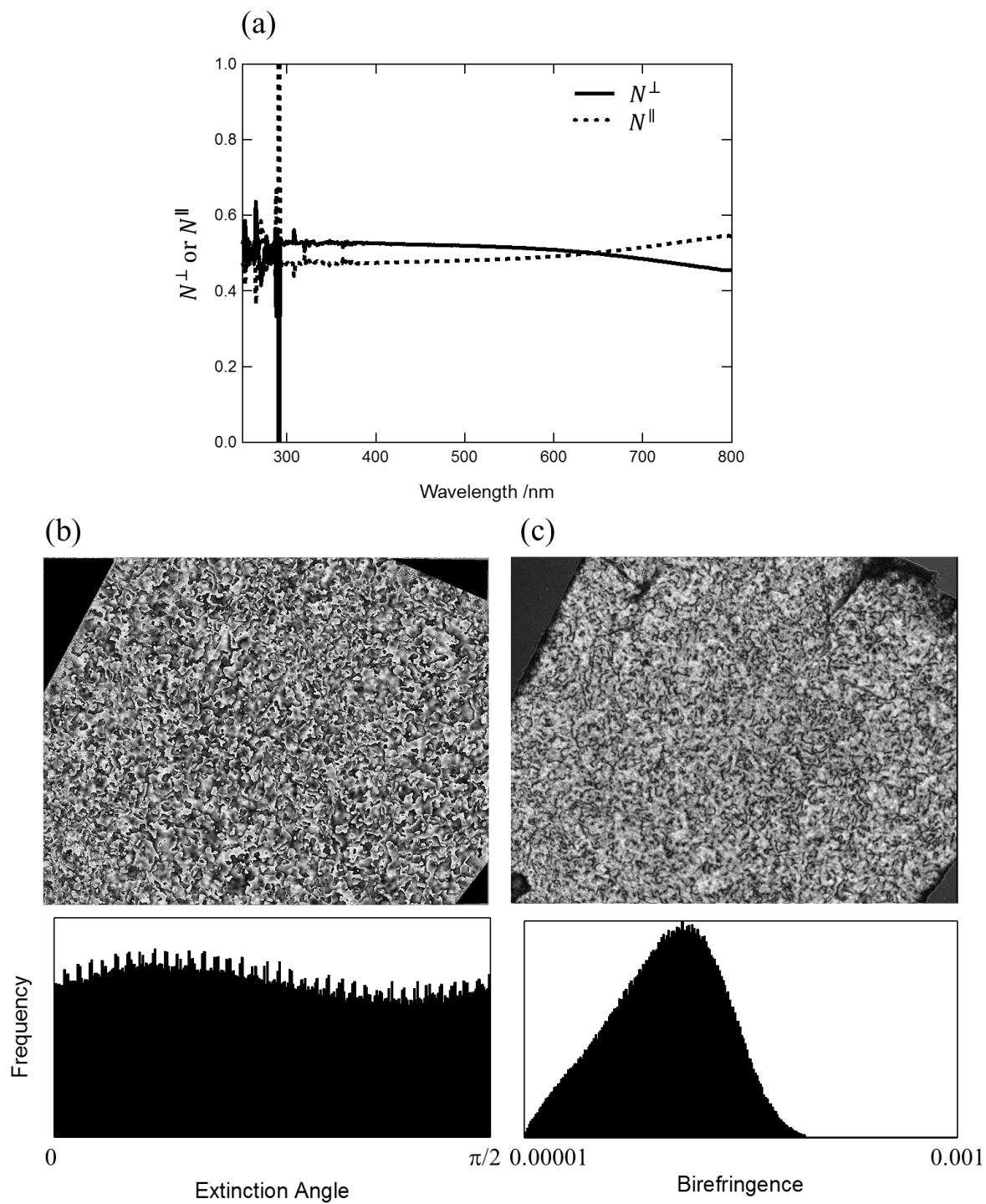


Figure 3–7. (a) Normalized intensity of the transmitted light in the crossed Nicol prisms and in the parallel direction as a function of wavelength in a range of 250 – 800 nm. (b) Distribution image of  $\chi$  at room temperature and its histogram for  $h$ -PC<sub>4</sub>-PFSI. (c) Distribution image of  $\Delta n$  at room temperature and its histogram for  $h$ -PC<sub>4</sub>-PFSI.

### 3-3-4 X-ray Scattering

According to Winey and co-workers,<sup>11, 12</sup> poly(1-butyl-3-vinylimidazolium) based ionic liquids having larger counter anions exhibit three amorphous halo peaks in WAXS profiles around at  $q_b = 3 \text{ nm}^{-1}$ ,  $q_i = 8 \text{ nm}^{-1}$ , and  $q_p = 13 \text{ nm}^{-1}$  corresponding to the backbone-to-backbone, the anion-to-anion, and the pendant-to-pendant spacing, respectively. In our data for *h*-PC<sub>4</sub>-TFSI as shown in Figure 3-8 (a), three scattering peaks are in good accordance with their results. Compared with the *h*-PC<sub>4</sub>-TFSI system, there is a significant difference in the sharpness of the  $q_b$  peak for *h*-PC<sub>4</sub>-PFSI and *h*-PC<sub>4</sub>-HFSI. This sharpening can be caused by the formation of ionic arrays.

One may consider that the mean spacing between the ionic arrays is detected using SAXS measurements. Figure 3-8 (b) shows the SAXS profiles with a scattering vector range of 0.04–1  $\text{nm}^{-1}$  for *h*-PC<sub>4</sub>-TFSI, *h*-PC<sub>4</sub>-PFSI, and *h*-PC<sub>4</sub>-HFSI. None of distinct peaks was observed. However, Nakamura et al.<sup>1</sup> have pointed out that PILs are filled with only ions and hence SAXS measurements probably show no evidence of ion aggregates in PILs systems.<sup>1</sup> Therefore, I speculate that the mean spacing between the ordered structures in *h*-PC<sub>4</sub>-PFSI and *h*-PC<sub>4</sub>-HFSI are out of SAXS  $q$  ranges investigated. Here, it should be noted that the scattered intensity shows the power law dependence,  $I \sim q^{-4}$ , in a  $q$  range from 0.03  $\text{nm}^{-1}$  to 0.2  $\text{nm}^{-1}$ . According to the prediction of Porod's law,<sup>13</sup> the power law  $q^{-4}$  indicates the presence of interface at which electron densities are different. In the SAXS experiments, 2–10 pieces of sample sheets was piled up to obtain sufficient intensity. Therefore, the interface between air and polymers may result in the observation of Porod's law in the PIL systems.

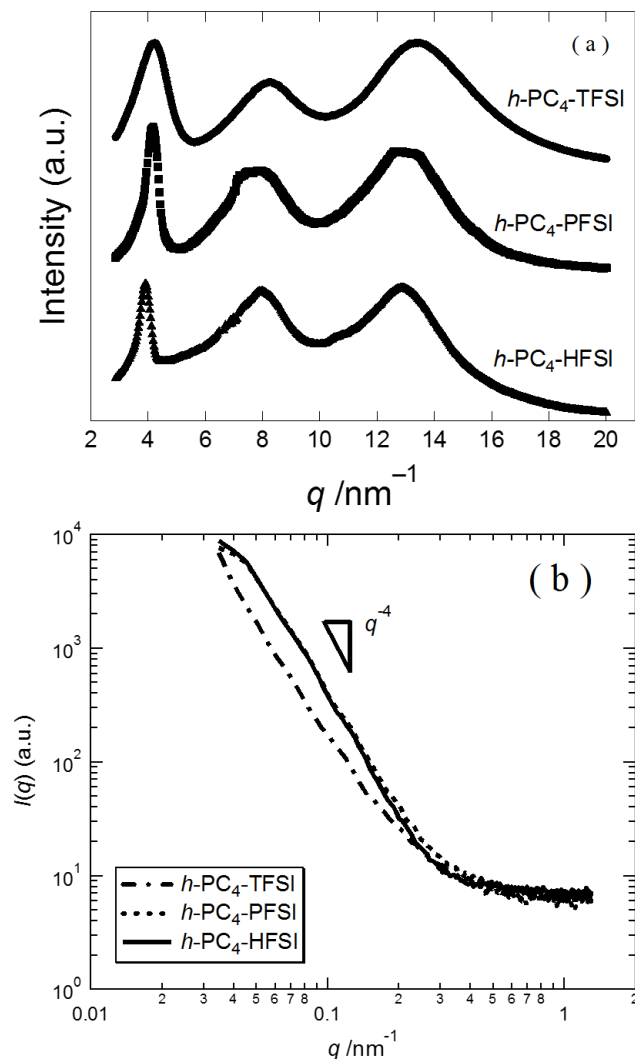


Figure 3–8. (a) Wide angle X-ray scattering profiles for *h*-PC<sub>4</sub>-TFSI, *h*-PC<sub>4</sub>-PFSI, and *h*-PC<sub>4</sub>-HFSI at room temperature. The data are shifted vertically for clarity. (b) SAXS profiles for *h*-PC<sub>4</sub>-TFSI, *h*-PC<sub>4</sub>-PFSI, and *h*-PC<sub>4</sub>-HFSI at room temperature.

### 3–3–5 Linear Viscoelasticity

Figure 3–9 (a) displays the composite curves of  $E^* = E' + iE''$  for *h*-PC<sub>4</sub>-PFSI, *c*-PC<sub>4</sub>-PFSI, *h*-PC<sub>4</sub>-HFSI, and those of  $3G^* = 3G' + i3G''$  for *h*-PC<sub>4</sub>-TFSI. The obtained spectra at various temperatures were reduced at a reference temperature,  $T_r = T_g + 70\text{K}$ , using viscoelastic shift factors,  $a_T$ . The spectra for *c*-PC<sub>4</sub>-PFSI and *h*-PC<sub>4</sub>-HFSI were vertically shifted for clarity.

The time-temperature superposition worked well for all the systems within the whole measurement temperature range, which is consistent with the result from the studies mentioned above.

In the glassy zone from  $10^5 \text{ rad s}^{-1}$  to  $10^9 \text{ rad s}^{-1}$ , the frequency dependence of  $E^*$  for *c*-, *h*-PC<sub>4</sub>-PFSI, and *h*-PC<sub>4</sub>-HFSI is similar to that of  $G^*$  for *h*-PC<sub>4</sub>-TFSI. The slightly stretched spectrum of  $E''$  for *h*-PC<sub>4</sub>-HFSI could be attributed to the mode distribution caused by flexibility of longer perfluoroalkyl chains.

However, the frequency dependence at frequencies lower than  $\omega a_T = 10^4 \text{ rad s}^{-1}$  for *h*-PC<sub>4</sub>-PFSI, *c*-PC<sub>4</sub>-PFSI, and *h*-PC<sub>4</sub>-HFSI are quite different from that for *h*-PC<sub>4</sub>-TFSI. In the *h*-PC<sub>4</sub>-TFSI system, the storage shear modulus decreased by three decades in magnitude during the glass transition zone. In contrast, in the *c*-, *h*-PC<sub>4</sub>-PFSI and *h*-PC<sub>4</sub>-HFSI systems, the storage Young's modulus decreased by only one decade in magnitude during their glass transition zones. Consequently, the elastic modulus for PILs was enhanced by introducing larger counter anions. Furthermore, the similar frequency dependence for *h*-PC<sub>4</sub>-PFSI and *c*-PC<sub>4</sub>-PFSI indicates that the formation of ionic arrays does not affect the mechanical strength of PILs.

After the glass-to-rubber transition zone, the rubbery and subsequent the onset of terminal flow zones were observed in the *h*-PC<sub>4</sub>-TFSI system. In contrast, for *h*-PC<sub>4</sub>-PFSI, *c*-PC<sub>4</sub>-PFSI, and *h*-PC<sub>4</sub>-HFSI, the frequency dependence of  $G'$  is always higher than that of  $G''$ , similarly to that for phenolic resins having relatively large cross-linking density.<sup>14</sup> The modulus gradually decreases with decreasing frequencies. The terminal flow zones were not observed for *h*-PC<sub>4</sub>-PFSI, *c*-PC<sub>4</sub>-PFSI. To see the global relaxation of polymer chains, in Figure 3–9 (b), the relaxation modulus,  $G(t)$ , of *h*-PC<sub>4</sub>-PFSI are shown as a function of time,  $t$ . The modulus keeps its magnitude as high as  $10^6 \text{ Pa}$  at  $t = 4.0 \times 10^4 \text{ s}$  and the terminal relaxation is not observed in this time range. The disordering of ionic arrays can be induced by the reorientational motions of polymer chains. This result suggests that much more time is required

to see the disordering process in micrographs shown in Figure 3–5. As will be discussed in Chapter 4, the dielectric studies showed that a large number of counter anions are trapped in local environments. The coupling between ion pair motion and motions of polymer chains became strong with increasing the ionic sizes of counter anions. These results suggest the stronger restriction of segmental motion of polymers for larger counterion systems. This picture is consistent with the very long terminal relaxation time for the PILs having counter ions of PFSI and HFSI. If ions can move more freely, the chains would relax faster.

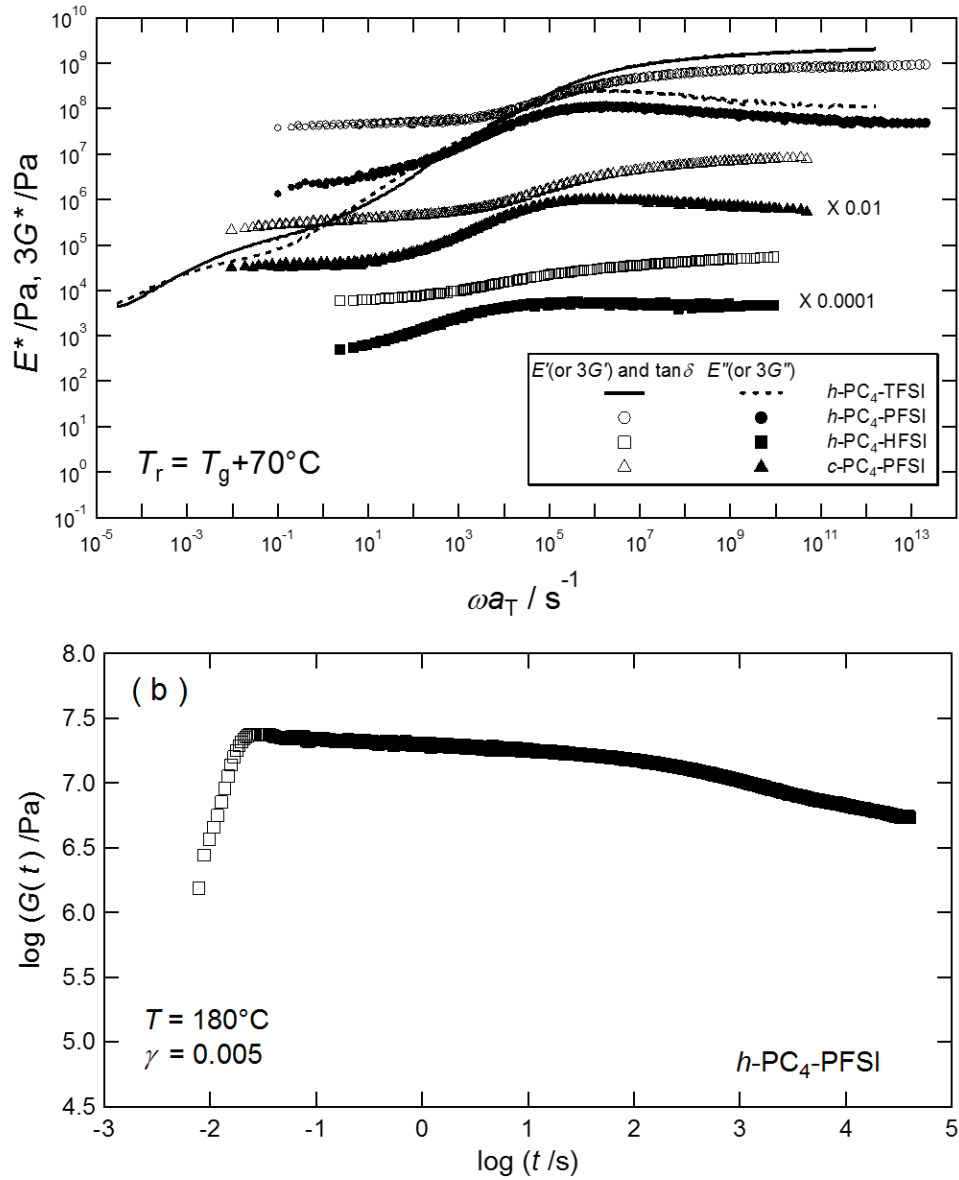


Figure 3–9. (a) Frequency dependence of  $E^*$  for  $h\text{-PC}_4\text{-HFSI}$ ,  $h\text{-PC}_4\text{-PFSI}$ , and  $c\text{-PC}_4\text{-PFSI}$ , and that of  $G^*$  for  $h\text{-PC}_4\text{-TFSI}$ . (b) Time dependence of  $G(t)$  for  $h\text{-PC}_4\text{-PFSI}$  at  $T = 180^\circ\text{C}$ .

### 3–3–6 MSOR Analysis

Figure 3–10 (a) displays the composite curves for the complex tensile strain-optical coefficient  $O^*$  for  $c\text{-PC}_4\text{-PFSI}$ . At low frequencies, the frequency dependence of  $O^*$  is similar to that of  $E^*$  for  $c\text{-PC}_4\text{-PFSI}$ . Moreover, at high frequencies, the frequency dependence of  $O''$

is in good accordance with that of  $E''$ . Thus, according to the MSOR, the frequency dependence of  $E^*$  and  $O^*$  can be described as the simple summation of two components: the glass motion (G) and the motion after glass transition (X).

$$E^*(\omega) = E_X^*(\omega) + E_G^*(\omega) \quad (3-4)$$

$$O^*(\omega) = O_X^*(\omega) + O_G^*(\omega) = C_X E_X^*(\omega) + C_G E_G^*(\omega) \quad (3-5)$$

Here, quantities having subscript,  $i = G$  and  $X$ , stand for the component functions.  $C_i$  is the stress-optical coefficient for the component  $i$ , and the value of  $C_i$ , as shown in Figure 3-10 (b), can be estimated from the plateau value of  $O'/E'$  for the X component and of  $O''/E''$  for the G component, respectively. The component G should be the glassy component of *c*-PC<sub>4</sub>-PFSI because the frequency dependence of the G component agrees with that for the glassy component of *h*-PC<sub>4</sub>-TFSI.

Following the method mentioned above, I determined  $C_X = 5.5 \times 10^{-10} \text{ Pa}^{-1}$  and  $C_G = 1.0 \times 10^{-10} \text{ Pa}^{-1}$ . The value of  $C_G$  is close to the stress-optical coefficient for a typical ionic liquid, BmimCl,  $C_{\text{BmimCl}} = 1.8 \times 10^{-10} \text{ Pa}^{-1}$  at  $-20 \text{ }^\circ\text{C}$ .<sup>15</sup> Therefore, the motion of the G component could be assigned to the reorientation motion of a repeating units of *h*-PC<sub>4</sub>-PFSI, which is consistent with the motion of the glassy component observed in ordinary amorphous polymers. On the other hand, the value of  $C_X$  is five times as large as that of  $C_G$ , and is still much smaller than that corresponding to the orientation motion of viscoelastic segment, namely the rubbery component. Also, I note that this value is close to the stress-optical coefficient related to the cooperative torsional motions of structural units for the *h*-PC<sub>4</sub>-TFSI, i.e.,  $C_L = 1.8 \times 10^{-10} \text{ Pa}^{-1}$  as described in Chapter 2. Therefore, the motion of the S component could be assigned to the cooperative local motion of chains.

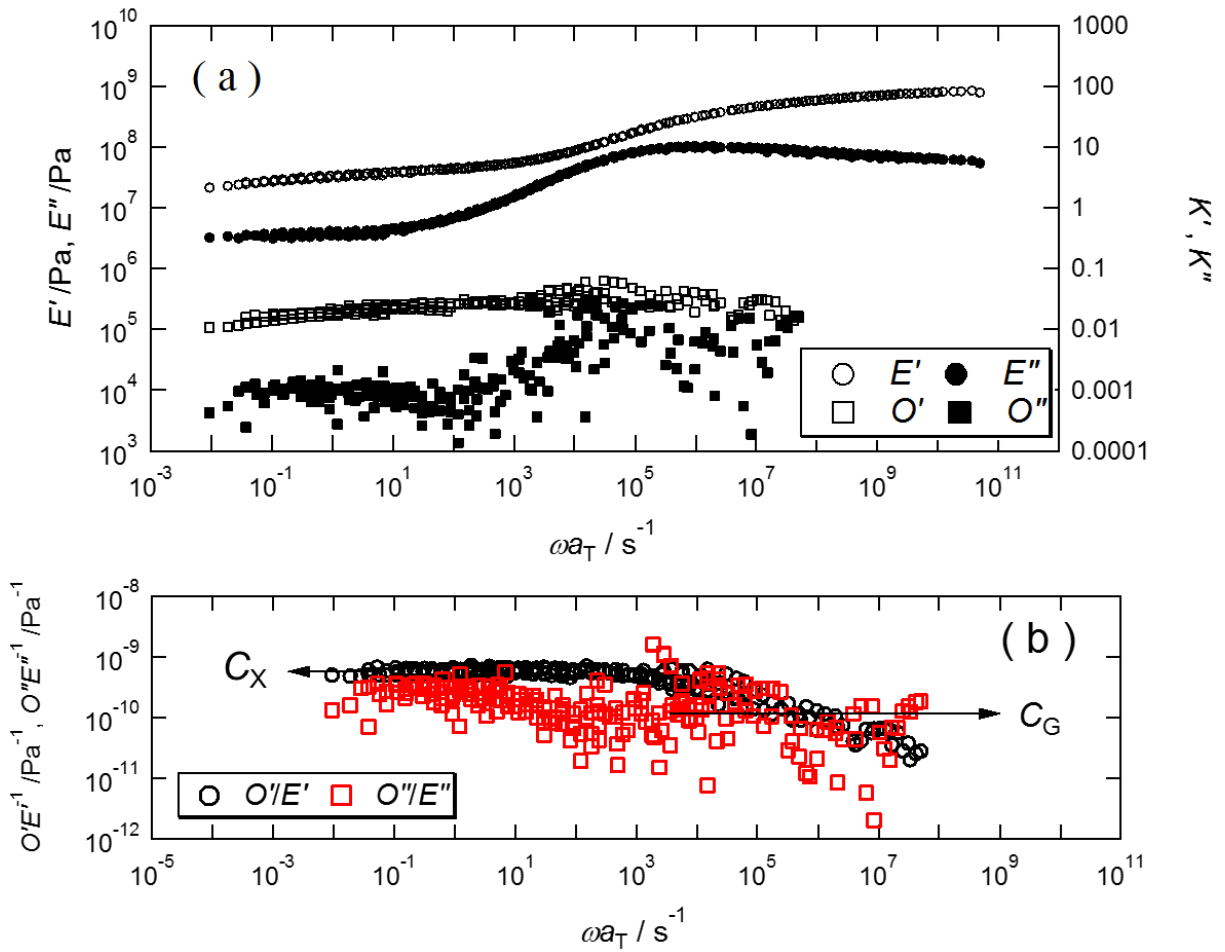


Figure 3–10. (a) Composite curves for the complex Young's modulus  $E^*$  and the complex strain-optical coefficient  $O^*$  for *c*-PC<sub>4</sub>-PFSI. (b) Frequency dependence of  $O'(\omega)/E'(\omega)$  and  $O''(\omega)/E''(\omega)$  for *c*-PC<sub>4</sub>-PFSI.

### 3-4 Conclusion

It is suggested that the unique ionic arrays are formed in PC<sub>4</sub>-PFSI and PC<sub>4</sub>-HFSI having counter anions with larger ionic volume than that of cations. The formation of ionic arrays depended on the preparation methods. Although not completely understand yet, the larger counter anions could make polymer chains more rigid. In this case, the rod-like segments is capable of forming arrays. The orientation directions of counter anions may be attributed to the difference in morphology. These ordered structures held their arrays far above the glass transition temperature. This is presumably because the segmental motions of polymer chains

are highly restricted.

In many cases of solid-state single ion conductive polyelectrolytes, ionic conductivities and mechanical strengths are in trade-off relationship since ion motions are strongly correlated with the motions of polymer chains. In this context, our result provides one of the strategies to enhance mechanical properties of polymerized ionic liquids with keeping ionic conductivity high.

### 3–5 References

- (1) Nakamura, K.; Saiwaki, T.; Fukao, K.; Inoue, T. *Macromolecules* **2011**, *44*, 7719-7726.
- (2) Nakamura, K.; Fukao, K.; Inoue, T. *Macromolecules* **2012**, *45*, 3850-3858.
- (3) Oba, N.; Inoue, T. *Rheol. Acta* **2016**, *55*, 699-708.
- (4) Hongladarom, K.; Burghardt, W. R.; Baek, S. G.; Cementwala, S.; Magda, J. J. *Macromolecules* **1993**, *26*, 772-784.
- (5) Romo-Uribe, A.; Dominguez-Diaz, M.; Romero-Guzman, M. E.; Rejon, L.; Saldivar-Guerrero, R. *Rheol. Acta* **2009**, *48*, 201-215.
- (6) Terao, K.; Shigeuchi, K.; Oyamada, K.; Kitamura, S.; Sato, T. *Macromolecules* **2013**, *46*, 5355-5362.
- (7) Madsen, L. A.; Dingemans, T. J.; Nakata, M.; Samulski, E. T. *Phys. Rev. Lett.* **2004**, *92*.
- (8) Granasy, L.; Pusztai, T.; Tegze, G.; Warren, J. A.; Douglas, J. F. *Phys Rev E* **2005**, *72*.
- (9) Alizadeh, A.; Richardson, L.; Xu, J.; McCartney, S.; Marand, H.; Cheung, Y. W.; Chum, S. *Macromolecules* **1999**, *32*, 6221-6235.
- (10) Pereiro, A. B.; Pastoriza-Gallego, M. J.; Shimizu, K.; Marrucho, I. M.; Lopes, J. N. C.; Pineiro, M. M.; Rebelo, L. P. N. *J. Phys. Chem. B* **2013**, *117*, 10826-10833.
- (11) Salas-de la Cruz, D.; Green, M. D.; Ye, Y. S.; Elabd, Y. A.; Long, T. E.; Winey, K. I. *J Polym Sci Pol Phys* **2012**, *50*, 338-346.
- (12) Liu, H. J.; Paddison, S. J. *Acs Macro Lett* **2016**, *5*, 537-543.
- (13) Porod, G. *Kolloid Z Z Polym* **1951**, *124*, 83-114.
- (14) Maji, S.; Urakawa, O.; Inoue, T. *Polym. J.* **2014**, *46*, 272-276.
- (15) Maeda, A.; Inoue, T.; Sato, T. *Macromolecules* **2013**, *46*, 7118-7124.

---

## CHAPTER 4

# Ionic Transport Mechanism of Polymerized Ionic Liquids with a Correlation of Nanoscale Morphology

---

### 4-1 Introduction

Polymerized ionic liquids (PILs) combine the attractive thermal and mechanical properties of polymers and unique electrical properties of ionic liquids (ILs) in the same material.<sup>1-3</sup> These properties make PILs appealing candidates for various applications, such as batteries, supercapacitors, and actuators. High ionic conductivity is one of the major requirements of electrolytes for these applications. Therefore, a lot of efforts in the recent past has focused on studies of the link between molecular structure and ionic transport in PILs, with the aim of developing new polymer electrolytes with high ionic conductivities.

Ion transport in solid polymer electrolytes involves segmental motion of polymer chains<sup>4</sup> and ion hopping.<sup>5</sup> Nakamura et al.<sup>6</sup> have reported that the ionic conductivities of poly(1-butyl-3-vinylimidazolium)-based ionic liquids exhibits the Vogel-Fulcher-Tammann (VFT) type temperature dependence at high temperatures and crossed over to the Arrhenius type dependence as temperature decreases.<sup>7</sup> They also reported that their ionic conductivities are related to the ion pair motion (the lifetime of ion pair).<sup>6</sup> The transition into the Arrhenius type behavior of ionic conductivity strongly suggests that the ionic transport and segmental motion of chains are decoupled at low temperatures.<sup>3</sup> For ordinary polyelectrolytes systems such as lithium ions in poly(ethylene glycol), the diffusion of ions is dominated by the segmental motion of polymer chains.<sup>8, 9</sup> Furthermore, Sangoro et al.<sup>3</sup> have reported that the ionic conductivity of an aprotic molecular IL controlled by the structural relaxation is  $10^{-12}$  S cm<sup>-1</sup> at  $T_g$ , whereas the IL after polymerization exhibits the ionic conductivity as high as  $10^{-6}$  S cm<sup>-1</sup> at

$T_g$ . However, the molecular origin of this disparity remains unclear. Therefore, fundamental understanding of such dramatic changes in ionic conductivity is required to find new possibilities in the design of PILs with high ionic conductivities.

Structural studies can provide insight into the understanding of the molecular origin of decoupling behavior between the ionic transport and segmental motion of chains. Long and coworkers<sup>10-13</sup> have studied the relationship between the morphology and ionic conductivity using the PILs having different alkyl chain lengths placed at the edge of side chains. The ionic conductivity decreases with increasing alkyl chain lengths. Moreover, the backbone-to-backbone scattering peak in WAXS profile increases proportionally to the number of alkyl chains. They conclude that the intermolecular separation provides the higher energy barrier for counter anions that move from one polymer chain to another chain, resulting in the decrement of ionic conductivity with increasing alkyl chain lengths. However, the correlation between ionic conductivity and the other characteristic spacing such as anion-to-anion spacing described in chapter 3 is still unclear. These spacings may depend on chemical structures of counter anions.

In this Chapter, the relationship between chemical structure, morphology, and ionic conductivity are investigated using a series of poly(1-alkyl-3-vinylimidazolium)-based ionic liquids with various counter anions. Figure 4-1 shows the chemical structures of cations and anions used in this study. A series of poly(1-alkyl-3-vinylimidazolium bis(trifluoromethanesulfonyl)imide) ( $PC_m$ -TFSI) are used for the dependence of alkyl chain lengths. A series of poly(1-butyl-3-vinylimidazolium)-based ionic liquids are used for the dependence of counter anion species. The number density of conducting ions and their mobility are discussed to clarify the effects of alkyl chain lengths and counter anion species on counterion transporting mechanisms. The decoupling between the segmental motion and ionic conductivity is characterized in terms of the ionic volume ratio,  $V_r$ , of an anion,  $V_a$ , to a cation,  $V_c$ .

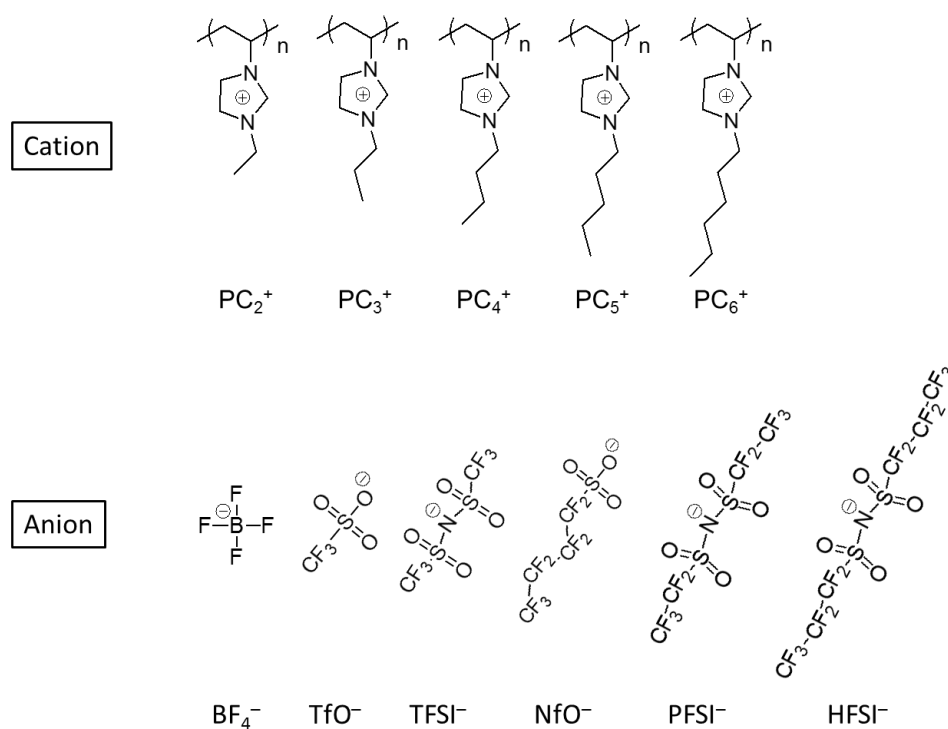


Figure 4–1. Chemical structures of poly(1-alkyl-3-methylimidazolium) polycations (PC<sub>m</sub><sup>+</sup>) having various alkyl chains from ethyl ( $m = 2$ ) to hexyl ( $m = 6$ ) and counter anions, tetrafluoroborate (BF<sub>4</sub><sup>-</sup>), trifluoromethanesulfonate (TfO<sup>-</sup>), nonafluorobuthanesulfonate (NfO<sup>-</sup>), bis(pentafluoroethanesulfonyl)imide (PFSI<sup>-</sup>), and bis(heptafluoropropanesulfonyl)imide (HFSI<sup>-</sup>).

## 4–2 Experimental Methods

**Materials.** 1-Bromopropane was purchased from Wako Pure Chemicals. 1-Bromohexane was purchased from TCI. 1-Bromopentane was purchased from Aldrich. These materials were used as received. Deuterated water and deuterated DMSO were purchased from Merck and used as solvents in NMR measurements.

### *Synthesis.*

(a) Poly(1-propyl-3-vinylimidazolium bis(trifluoromethanesulfonyl)imide). 1-Propyl-3-vinylimidazolium bromide (C<sub>3</sub>-Br) was synthesized by refluxing 1-vinylimidazole (38.4 g) and

excess 1-bromopropane (67.2 g) in methanol (30 mL) at 60°C for 3 days. After the evaporation of methanol and unreacted 1-bromopropane, C<sub>3</sub>-Br was dried overnight under vacuum at 40°C. The purity of C<sub>3</sub>-Br was confirmed using a <sup>1</sup>H-NMR measurement in D<sub>2</sub>O. (ppm) δ 9.1 (1H, s, N-CH-N), δ 7.8 (1H, d, N-CH=CH-N-Pro), δ 7.7(1H, d, N-CH=CH-N-Pro), δ 7.2 (1H, q, CH<sub>2</sub>=CH-N), δ 5.9 (1H, dd, trans-CH<sub>2</sub>=CH-N), δ 5.5 (1H, dd, cis-CH<sub>2</sub>=CH-N), δ 4.2 (2H, t, N-CH<sub>2</sub>-CH<sub>2</sub>-CH<sub>3</sub>), δ 2.0 (2H, m, N-CH<sub>2</sub>-CH<sub>2</sub>-CH<sub>3</sub>), δ 1.0 (3H, t, N-CH<sub>2</sub>-CH<sub>2</sub>-CH<sub>3</sub>))

Poly(1-propyl-3-vinylimidazolium bromide) (PC<sub>3</sub>-Br) was synthesized via free radical polymerization of C<sub>3</sub>-Br (24.1 g). Polymerization was initiated by AIBN (181 mg) at 60°C for 1 day. After polymerization, the product was dialyzed against water and PC<sub>3</sub>-Br was obtained as a powder via freeze-drying method.

Poly(1-propyl-3-vinylimidazolium bis(trifluoromethanesulfonyl)imide) (PC<sub>3</sub>-TFSI) was prepared using the counterion conversion method proposed by Mecerreyes.<sup>14</sup> An aqueous solution including 1.5 eq of LiTFSI (2.0 g) was slowly titrated into aqueous PC<sub>3</sub>-Br (1.04 g) solution and stirred for 5 days at room temperature. The resulting precipitation was washed with water until the filtrate remained transparent when adding an aqueous solution of AgNO<sub>3</sub>. The purity of PC<sub>3</sub>-TFSI was confirmed by elemental analysis. *ELEM.ANAL.* Calcd for C<sub>10</sub>H<sub>13</sub>N<sub>3</sub>O<sub>4</sub>S<sub>2</sub>F<sub>6</sub> (wt%): C, 28.77; H, 3.15; N, 10.07. Found (wt%): C, 28.78; H, 3.02; N, 10.05.

(b) Poly(1-pentyl-3-vinylimidazolium bis(trifluoromethanesulfonyl)imide). A mixture of 1-Bromopentane (32.9 g), 1-vinylimidazole (15.3 g), methanol (30mL) was refluxed at 65°C for 3 days. After the evaporation of methanol and unreacted 1-bromopentane, the aqueous solution of the product was washed with ethyl acetate 2-3 times to eliminate unreacted 1-vinylimidazole. The purity of 1-pentyl-3-vinylimidazolium bromide (C<sub>5</sub>-Br) was confirmed using a <sup>1</sup>H-NMR

measurement in deuterated DMSO. (ppm)  $\delta$  11.3 (1H, s, N-CH-N),  $\delta$  9.6 (1H, t, N-CH=CH-N-Pn),  $\delta$  9.3 (1H, t, N-CH=CH-N-Pn),  $\delta$  8.5 (1H, q, CH<sub>2</sub>=CH-N),  $\delta$  6.8 (1H, dd, trans-CH<sub>2</sub>=CH-N),  $\delta$  6.2 (1H, dd, cis-CH<sub>2</sub>=CH-N),  $\delta$  4.6 (2H, t, N-CH<sub>2</sub>-CH<sub>2</sub>-CH<sub>2</sub>-CH<sub>2</sub>-CH<sub>3</sub>),  $\delta$  1.7 (2H, m, N-CH<sub>2</sub>-CH<sub>2</sub>-CH<sub>2</sub>-CH<sub>2</sub>-CH<sub>3</sub>),  $\delta$  1.1-0.88 (4H, m, N-CH<sub>2</sub>-CH<sub>2</sub>-CH<sub>2</sub>-CH<sub>2</sub>-CH<sub>3</sub>),  $\delta$  0.47 (3H, t, N-CH<sub>2</sub>-CH<sub>2</sub>-CH<sub>2</sub>-CH<sub>2</sub>-CH<sub>3</sub>)

Poly(1-pentyl-3-vinylimidazolium bromide) (PC<sub>5</sub>-Br) was synthesized by free radical polymerization of C<sub>5</sub>-Br (10.8 g) initiated by AIBN (75.3 mg) in water at 60°C for 1 day. After polymerization, the product was dialyzed against water and PC<sub>5</sub>-Br was obtained as a powder via freeze-drying method.

Poly(1-pentyl-3-vinylimidazolium bis(trifluoromethanesulfonyl)imide) (PC<sub>5</sub>-TFSI) was prepared using the counterion conversion method proposed by Mecerreyes.<sup>14</sup> An aqueous solution including 1.5 eq of LiTFSI (1.40 g) was slowly titrated into aqueous PC<sub>5</sub>-Br (0.795 g) solution and stirred for 3 days at room temperature. The resulting precipitation was washed with water until the filtrate remained transparent when adding an aqueous solution of AgNO<sub>3</sub>. The purity of PC<sub>5</sub>-TFSI was confirmed by elemental analysis. *ELEM.ANAL.* Calcd for C<sub>12</sub>H<sub>17</sub>N<sub>3</sub>O<sub>4</sub>S<sub>2</sub>F<sub>6</sub> (wt%): C, 32.35; H, 3.85; N, 9.44. Found (wt%): C, 32.64; H, 3.82; N, 9.84.

(c) Poly(1-hexyl-3-vinylimidazolium bis(trifluoromethanesulfonyl)imide). The synthesis of 1-hexyl-3-vinylimidazolium bromide (C<sub>6</sub>-Br) was carried out following the same procedure proposed by Long et al.<sup>10</sup>

A mixture of 1-Bromohexane (143 g), 1-vinylimidazole (40.1 g), and ethyl acetate (155 mL) was refluxed at 77°C for 24 h. The resultant solution was separated into two phases, and the bottom viscous layer was washed with ethyl acetate. The residual 1-bromohexane and ethyl acetate was evaporated at 40°C for 24 h.

Poly(1-hexyl-3-vinylimidazolium bromide) (PC<sub>6</sub>-Br) was synthesized via free radical

polymerization of C<sub>6</sub>-Br (26.3 g). Polymerization was initiated by AIBN (167 mg) in dimethylformamide (15 mL) at 65°C for 24 h. PC<sub>6</sub>-Br was isolated through precipitation into acetone and subsequent filtering the obtained solid.

Poly(1-hexyl-3-vinylimidazolium bis(trifluoromethanesulfonyl)imide) (PC<sub>6</sub>-TFSI) was prepared using the counterion conversion method proposed by Mecerreyes.<sup>14</sup> A methanol solution of LiTFSI (1.5 eq, 2.06 g) was slowly titrated into methanol solution of PC<sub>6</sub>-Br (1.23 g) and stirred for 3 days at room temperature. This mixture was then slowly poured into water and the obtained solid was filtered. The purity of PC<sub>6</sub>-TFSI was confirmed by elemental analysis. *ELEM.ANAL.* Calcd for C<sub>13</sub>H<sub>19</sub>N<sub>3</sub>O<sub>4</sub>S<sub>2</sub>F<sub>6</sub> (wt%): C, 33.98; H, 4.18; N, 9.15. Found (wt%): C, 34.30; H, 4.10; N, 9.22.

The synthesis of PC<sub>2</sub>-TFSI was described elsewhere.<sup>2</sup>

The van der Waals volume of each cation,  $V_c$ , was estimated using the program built into the Winmostar version 6.018 software. The  $V_c$ s were calculated using structures of 1-alkyl-3-methylimidazolium cation (Amim<sup>+</sup>). Here, the all trans configurations for alkyl groups were considered in the calculations.

## ***Methods***

**a) Differential Scanning Calorimetry.** Glass transition temperature,  $T_g$ , was determined using an EXSTAR6000 (Hitachi High-Tech Science Corporation). Sample films of 9.1–10.1 mg were placed in open pans and then annealed before being hermetically sealed. Temperature ramps cycled from –10 to 180°C with cooling and heating rates of 10 °C/min.  $T_g$  was determined as the midpoint of the heat capacity change in the second cycle, and is listed in Table 4–1.

Table 4–1. Glass transition temperatures for PC<sub>2</sub>-TFSI, PC<sub>3</sub>-TFSI, PC<sub>5</sub>-TFSI, and PC<sub>6</sub>-TFSI.

	PC <sub>2</sub> -TFSI	PC <sub>3</sub> -TFSI	PC <sub>5</sub> -TFSI	PC <sub>6</sub> -TFSI
$T_g / ^\circ\text{C}$	63	58	53	42

**b) Dielectric Relaxation Spectroscopy.** Broadband Dielectric measurements were carried out using a Novocontrol dielectric analyzer with low applied voltage (0.1 V). The complex permittivity ( $\varepsilon^*(\omega) = \varepsilon'(\omega) - i\varepsilon''(\omega)$ ) and the complex conductivity ( $\kappa^*(\omega) = i\omega\varepsilon^*(\omega) = \kappa'(\omega) + i\kappa''(\omega)$ ) were obtained with a frequency ( $10^{-2}$ – $10^7$  Hz) and temperature ( $-150$ – $200^\circ\text{C}$ ) range under a dry nitrogen atmosphere. In the experiments of PC<sub>4</sub>-PFSI and PC<sub>4</sub>-HFSI, the PILs having the ionic arrays shown in Chapter 3 were used.

**c) Linear Viscoelasticity.** Linear viscoelastic measurements were carried out using an ARES-G2 (TA instruments) rheometer under oscillatory shear deformation ( $\gamma = 0.01\% - 30\%$ ) with a temperature range of  $35 - 200^\circ\text{C}$ . The complex shear modulus,  $G^*$ , was measured using a homemade parallel plate fixtures having a 4 mm diameter in a frequency range of  $0.1$ – $100$  rad  $\text{s}^{-1}$  under a nitrogen atmosphere.

**d) Wide-Angle X-ray Scattering.** Wide-Angle X-ray scattering was performed using a Rigaku DMAX/rapid microdiffractometer in transmission mode ( $\lambda = 0.154$  nm) at room temperature.

## 4–3 Results and Discussion

### 4–3–1 Linear Viscoelastic Response

Figure 4–2 shows the composite curves of the complex shear modulus  $G^* = G' + iG''$  for PC<sub>2</sub>-TFSI, PC<sub>3</sub>-TFSI, PC<sub>5</sub>-TFSI, and PC<sub>6</sub>-TFSI. The obtained spectra at various temperatures

were reduced at a reference temperature  $T_r = T_g + 10\text{K}$  using viscoelastic shift factors  $a_T$ . The time temperature superposition principle worked well over the whole frequency range, similarly to the case of PC<sub>4</sub>-TFSI system.

In the glass-to-rubber transition zone at frequencies from  $10^{-4}$  rad s<sup>-1</sup> to  $10^1$  rad s<sup>-1</sup>, the shape of spectra became shaper with increasing alkyl chain lengths. The inter-chain interaction could become more dominant with decreasing the volume ratio of an anion and a cation. In this case, the volume fraction of solvent like counter anions is decreased and hence the plasticization effect becomes weak.

The plausible segmental relaxation time,  $\tau_0$ , which is possibly close to the shortest Rouse relaxation time of segments was estimated from the reciprocal frequency where  $G'$  is equal to  $G''$  in the high frequency region near the  $G''$  peak. Because the loss modulus is widely stretched at high frequencies, the cross point of  $G'$  and  $G''$  was chosen to obtain unambiguously the relevant time scale of the segmental relaxation. The temperature dependence of  $\tau_0$  for PC<sub>6</sub>-TFSI and PC<sub>4</sub>-PFSI is shown in Figure 4-7, and is found to follow the Vogel-Fulcher-Tammann (VFT)-type equation.

$$\tau_0(T) = \tau_\infty \exp\left(\frac{D_0 T_0}{T - T_0}\right) \quad (4-1)$$

where  $\tau_\infty$ ,  $D_0$ , and  $T_0$  are the fitting parameters. Because the time-temperature superposition principle held well, the  $\tau_0$  at each temperature was calculated by  $\tau_0(T) = \tau_0(T_r)a_T(T)$  using the obtained viscoelastic shift factors  $a_T(T)$ . As for PC<sub>4</sub>-PFSI and PC<sub>4</sub>-HFSI where  $G'$  and  $G''$  did not cross as shown in chapter 3, the  $\tau_0$  was approximately estimated as the reciprocal of the frequency where the  $G''$  became the half height of its maximum in the glassy region based on the fact that the  $G''$  for PC<sub>4</sub>-TFSI becomes nearly the half of the maximum height at the cross

point frequency. In this chapter, I will evaluate the temperature dependence of the degree of decoupling between the hopping translation of counter anions and the segmental relaxation of polymers. Therefore, the absolute value of  $\tau_0$  does not affect the discussions described below.

The reciprocal frequency at the peak position in the glassy region of  $G''$  can be related to the relaxation time  $\tau_m$  corresponding to the rotational motion of monomer.

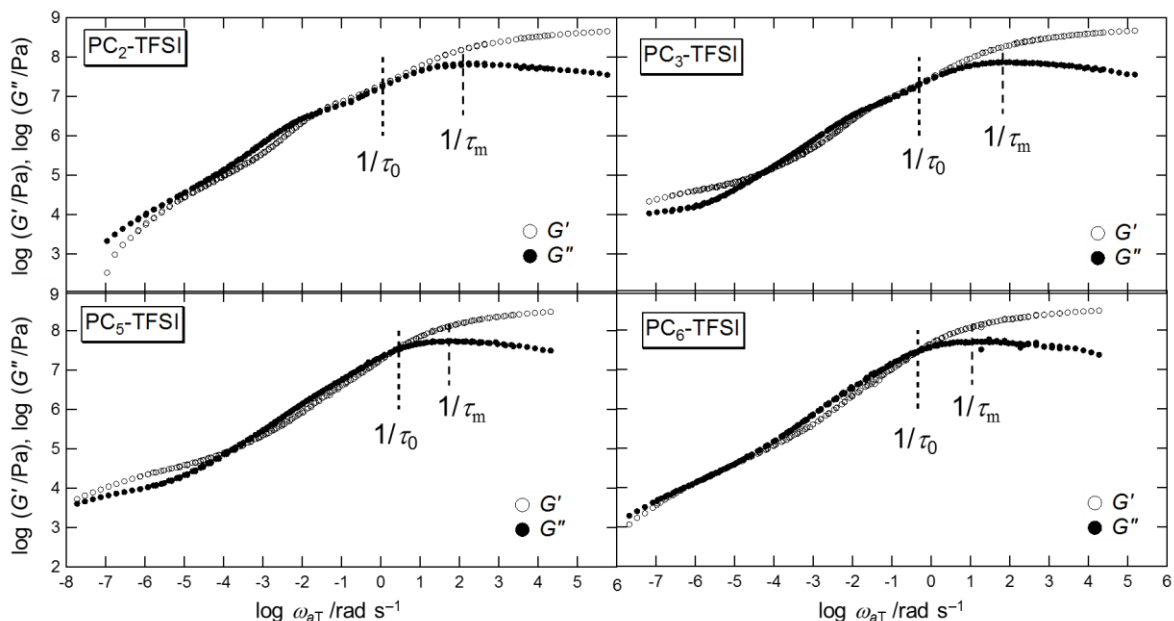


Figure 4–2. Composite curves of  $G^*$  for PC<sub>2</sub>-TFSI, PC<sub>3</sub>-TFSI, PC<sub>5</sub>-TFSI, and PC<sub>6</sub>-TFSI at  $T_r = T_g + 10K$ .

#### 4–3–2 Dielectric Relaxation Response

Figure 4–3 shows the dielectric spectra of PC<sub>6</sub>-TFSI at 40°C and PC<sub>4</sub>-PFSI at 80°C. There are three components found in  $\epsilon^*$  over the measurement frequency range. In the  $\epsilon'$ , a dielectric relaxation process is observed at intermediate frequencies from  $10^2 \text{ rad s}^{-1}$  to  $10^5 \text{ rad s}^{-1}$ . Then, a drastic increase of  $\epsilon'$  corresponding to the electrode polarization (EP) process, the blocking process of charge carriers at electrodes, is observed at lower frequencies. On the other hand, the diffusion process of ions dominates the frequency dependence of  $\epsilon''$  over the whole

frequency region. The dielectric relaxation process observed in the  $\varepsilon'$  is completely hidden in the  $\varepsilon''$ . The value of dc ionic conductivity,  $\kappa_{DC}$ , was estimated from a plateau value observed in  $\kappa'$ .

In order to eliminate the contribution of ionic conductivity from the spectra of  $\varepsilon''$ , the following derivative equation was utilized.

$$\varepsilon''_{\text{der}} = -\frac{\pi}{2} \frac{\partial \varepsilon'}{\partial \ln \omega} \quad (4-2)$$

This provides an ion conduction-free spectra of  $\varepsilon''$  in the frequency range where  $\varepsilon'$  does not show the EP process.<sup>15, 16</sup> Figure 4–2 includes the frequency dependence of  $\varepsilon''_{\text{der}}$ . The loss peak in  $\varepsilon''_{\text{der}}$  is comparable to the frequency region where the dielectric relaxation is observed in  $\varepsilon'$ . To evaluate the dielectric relaxation time  $\tau_{\text{HN}}$ , the  $\varepsilon''_{\text{der}}$  spectra were fitted using the empirical Havriliak-Negami (HN) function given by the following equation.<sup>16</sup>

$$\varepsilon''_{\text{der,HN}} = \frac{\pi}{2} \frac{\alpha\beta\Delta\varepsilon(\omega\tau)^\alpha \cos[\alpha\pi/2 - (1+\beta)\theta_{\text{HN}}]}{[1 + 2(\omega\tau)^\alpha \cos(\pi\alpha/2) + (\omega\tau)^{2\alpha}]^{(1+\beta)/2}} \quad (4-3)$$

$$\theta_{\text{HN}} = \tan^{-1}[\sin(\pi\alpha/2)/((\omega\tau)^{-\alpha} + \cos(\pi\alpha/2))] \quad (4-4)$$

$$\tau_{\text{HN}} = \tau \left( \sin\left(\frac{\alpha\beta\pi}{2+2\beta}\right) \right)^{1/\alpha} \left( \sin\frac{\alpha\pi}{2+2\beta} \right)^{-1/\alpha} \quad (4-5)$$

where  $\alpha$ ,  $\beta$ ,  $\Delta\varepsilon$ , and  $\tau$  are fitting parameters. As shown in Figure 4–7, the temperature dependence of  $\tau_{\text{HN}}$  at temperatures lower than  $T_g$  follows the Arrhenius-type equation ( $\tau_{\text{HN}} = A \exp(-E_a/RT)$ ) while the VFT-type of temperature dependence is observed at higher

temperatures than  $T_g$ , similarly to the case reported by Nakamura et al.<sup>6</sup> Therefore, the dielectric relaxation was assigned to the ion pair motion.

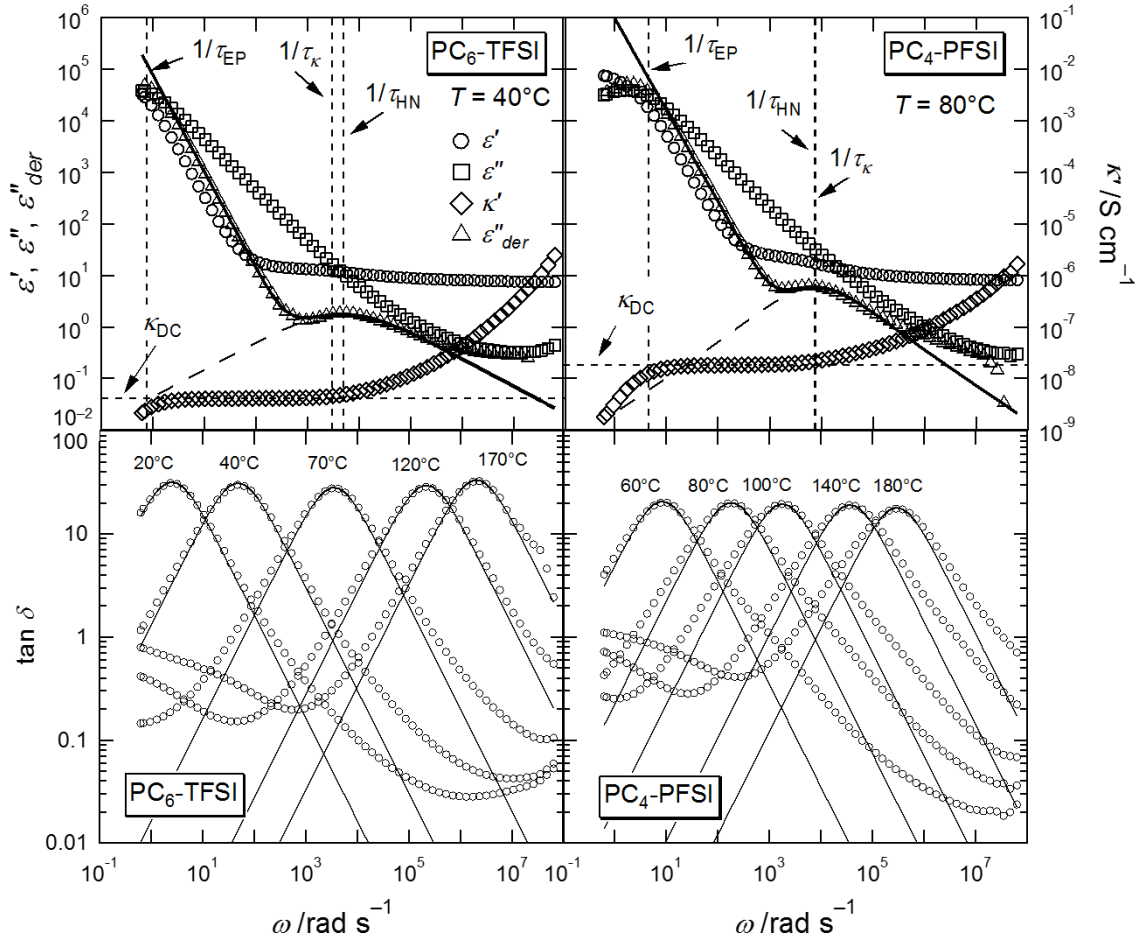


Figure 4–3. Top: the complex permittivity  $\epsilon^*$ , the real part of complex conductivity  $\kappa'$ , and the derivative function of  $\epsilon'$  for PC<sub>6</sub>-TFSI at 40°C and PC<sub>4</sub>-PFSI at 80°C. Bottom: the frequency dependence of loss tangent at representative temperatures.

#### 4–3–3 Comparison between $\tau_m$ and $\tau_{HN}$

Figure 4–4 shows the comparison between the frequency dependence of  $G^*$  and  $\epsilon''_{der}$  at  $T = T_g + 30K$  for PC<sub>4</sub>-PFSI, PC<sub>4</sub>-TfO, PC<sub>2</sub>-TFSI, and PC<sub>6</sub>-TFSI. The frequencies of  $1/\tau_m$  are always lower than those of  $1/\tau_{HN}$ , which is consistent with the previous works.<sup>6, 13</sup> The

difference in relaxation time between  $\tau_{\text{HN}}$  and  $\tau_{\text{m}}$  becomes smaller with increasing the sizes of counter anions and with decreasing the alkyl chain lengths. Figure 4–5 shows that the ratio of relaxation times,  $\tau_{\text{m}}/\tau_{\text{HN}}$ , is decreased with increasing the volume ratio,  $V_{\text{r}} = V_{\text{a}} / V_{\text{c}}$ , of an anion,  $V_{\text{a}}$ , and a cation,  $V_{\text{c}}$  when the  $V_{\text{r}}$  is larger than unity. In contrast, the  $\tau_{\text{m}}/\tau_{\text{HN}}$  seems to be constant with the  $V_{\text{r}}$  smaller than unity. The ion pair motion tended to be coupled with the structural relaxation of polymers with increasing counter anion sizes once the volume ratio of ions exceeds unity. This result suggests that the motions of polymer chains is required for ion transporting when ionic sizes of counter anions are large.

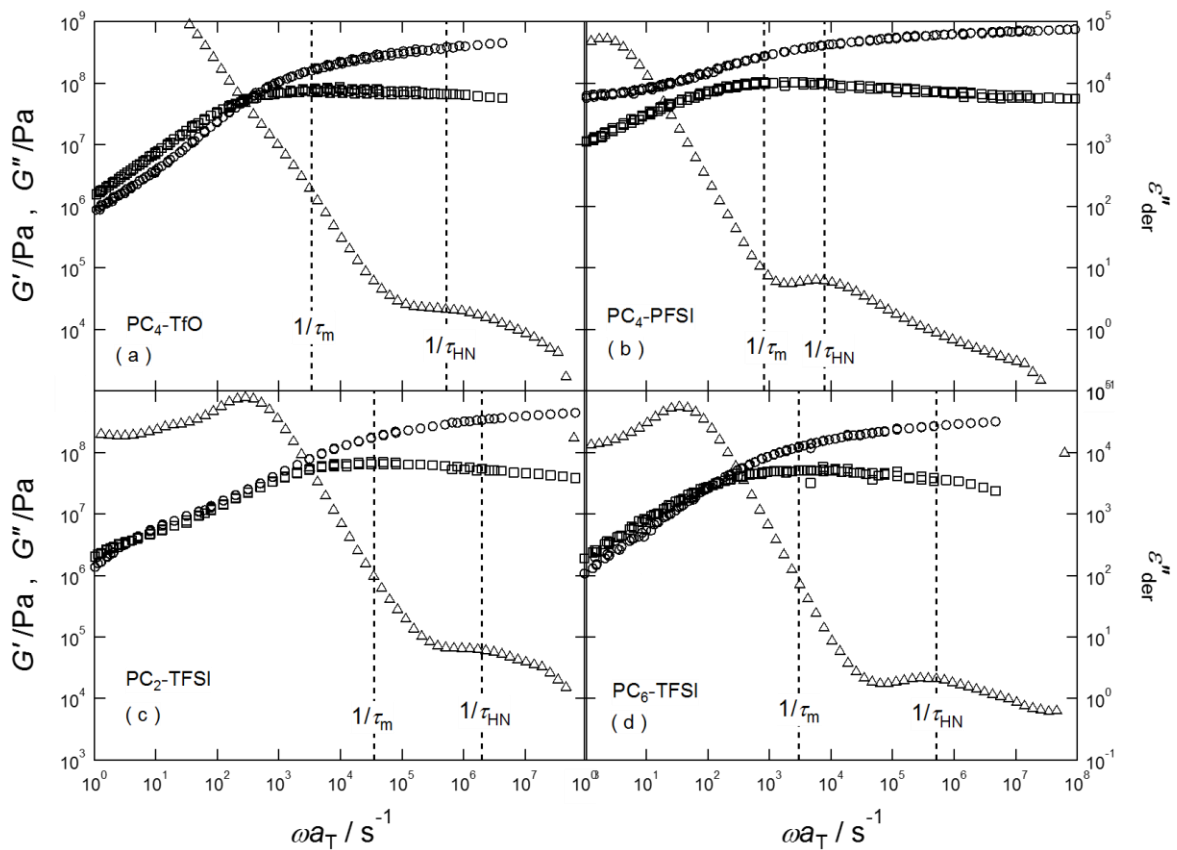


Figure 4–4. Comparison between  $G^*$  and  $\varepsilon''_{\text{der}}$  for (a) PC<sub>4</sub>-TfO, (b) PC<sub>4</sub>-PFSI, (c) PC<sub>2</sub>-TFSI, and (d) PC<sub>6</sub>-TFSI at  $T = T_{\text{g}} + 30\text{K}$ .

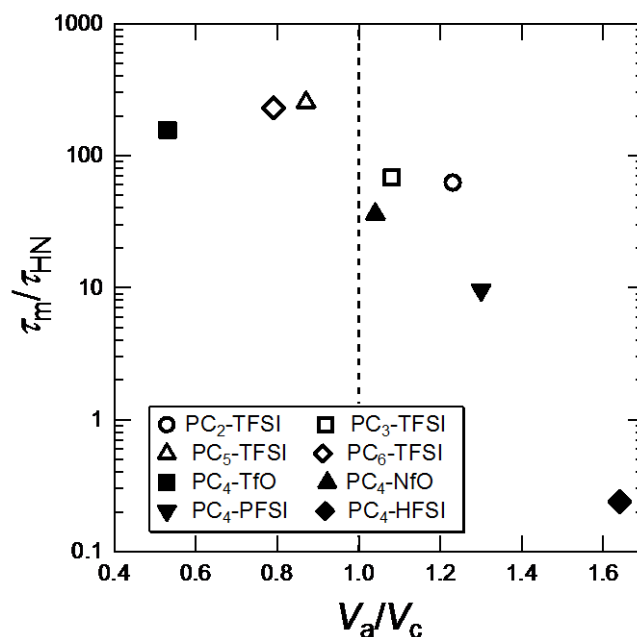


Figure 4–5. The relaxation time ratio of the monomer,  $\tau_m$ , to that for the ion pair motion,  $\tau_{HN}$ , as a function of the volume ratio of ions.

#### 4–3–4 Ionic Conductivity

Figure 4–6 (a) and (b) show the  $T_g/T$  dependence of ionic conductivity, so-called “ $T_g$ -independent ionic conductivity”, for a series of PILs having different alkyl chain lengths and having different counter anions, respectively. Since ion transport is coupled with motions of polymer chains, this  $T_g$ -independent plot enable us to evaluate the temperature dependence of ionic conductivity for the PILs in which the coefficient of friction for motions of polymer chains is equivalent to each other. For  $PC_m$ -TFSI where  $m$  is the number of alkyl chains, the  $T_g$ -independent ionic conductivity at  $T=T_g$  decreases systematically with increasing the alkyl chain length from ethyl ( $m = 2$ ) to hexyl ( $m = 6$ ), which is consistent with the previous report by Long et al.<sup>11</sup> The change in magnitude of  $\kappa_{DC}$  was less than one order. On the other hand, I observed differences in the  $T_g$ -independent ionic conductivity of up to four orders of magnitude when changing the counter anion species. In contrast to low molecular weight aprotic ILs for which the  $T_g$ -independent ionic conductivity remains comparable regardless of counter anion species,

Figure 4–6 reveals a systematic influence of the counterion size on the conductivity of PILs.

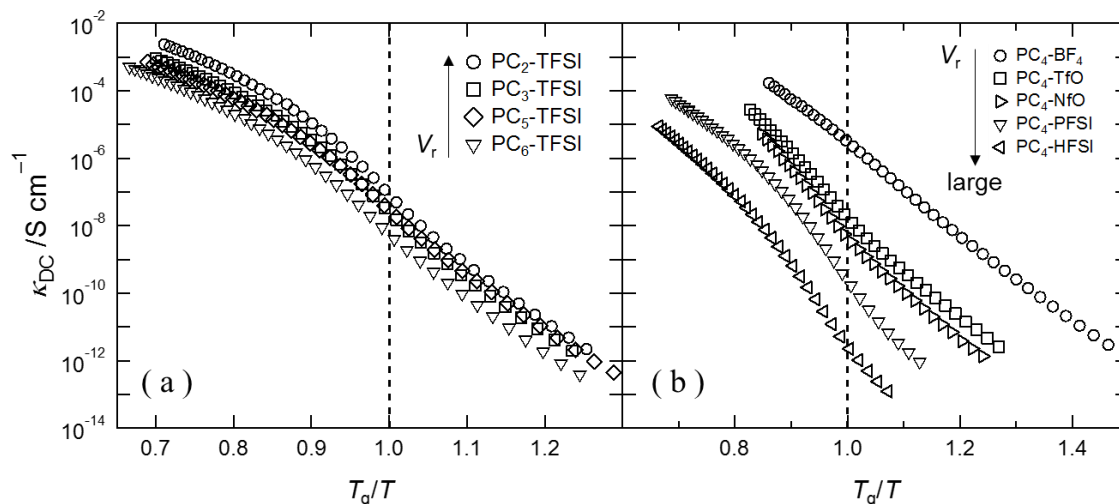


Figure 4–6. Ionic conductivity as a function of normalized inverse temperature by the  $T_g$  for each PIL. (a) Dependence of alkyl chain lengths. (b) Dependence of counter anion species.

The comparison between the temperature dependence of the ionic conductivity, segmental relaxation time, and relaxation time of ion pair motion for PC<sub>6</sub>-TFSI and PC<sub>4</sub>-PFSI is presented in Figure 4–7. The  $\kappa_{DC}$  exhibits the VFT type of temperature dependence at high temperatures above  $T_g$  and change its dependence into the Arrhenius type dependence below  $T_g$ . The transition of temperature dependence is the important parameters in ionic conductivity of PILs and will be discussed in section 4–3–7.

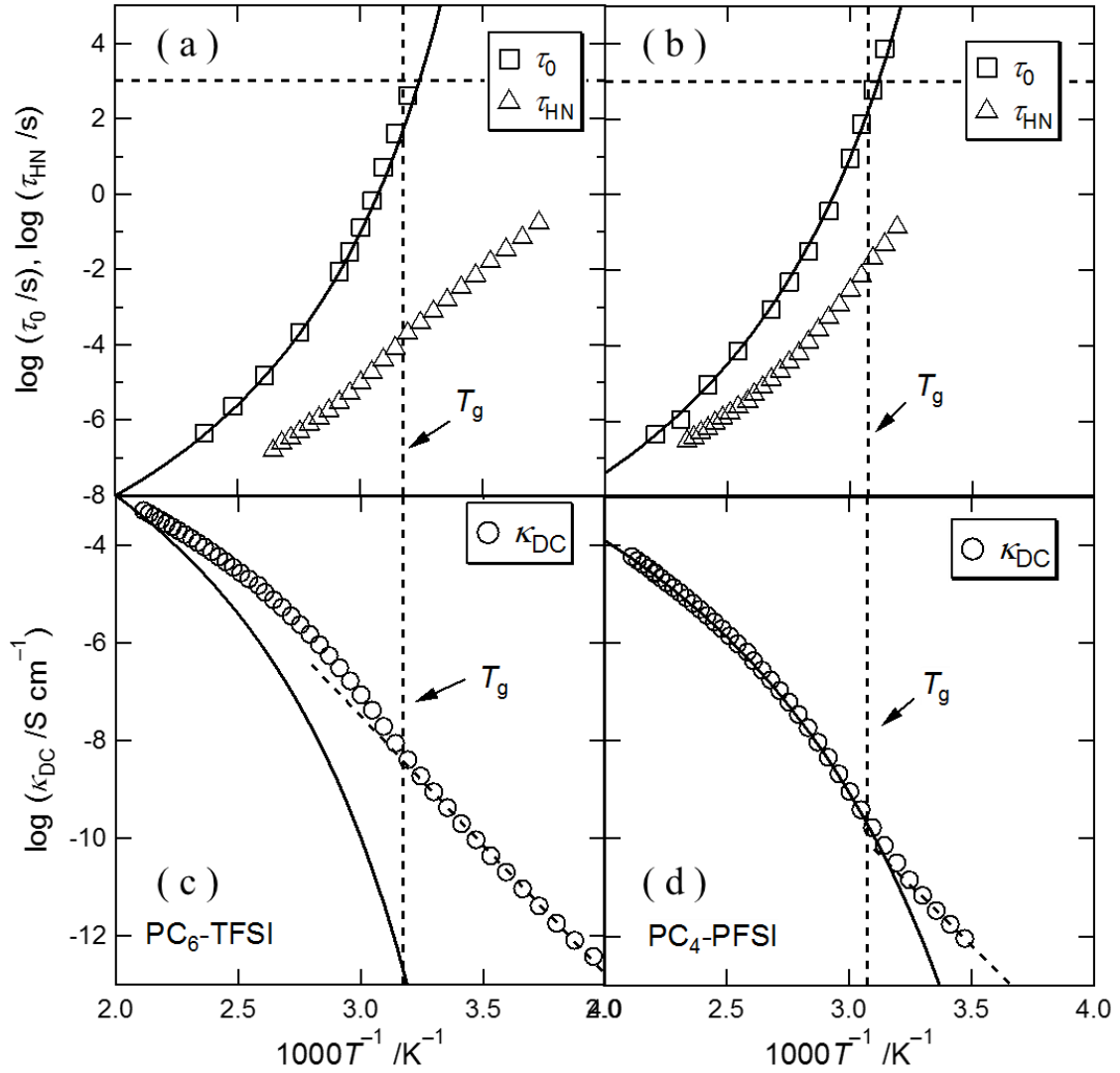


Figure 4–7. Temperature dependence of the segmental relaxation time  $\tau_0$ , dielectric relaxation time  $\tau_{\text{HN}}$ , and ionic conductivity  $\kappa_{\text{DC}}$  for PC<sub>6</sub>-TFSI and PC<sub>4</sub>-PFSI. The solid lines in the upper figures represent the VFT fit results. Those in the lower figures show also the VFT curves in the reciprocal form,  $\tau_0^{-1} \propto \kappa_{\text{DC}} (\propto \exp(-D_0 T_0 / (T - T_0)))$ , to fit the  $\kappa_{\text{DC}}$  data with the same  $T_0$  and  $D_0$  used in the upper figures.

#### 4–3–5 Electrode Polarization Analysis

According to the Nernst-Einstein equation, the dc ionic conductivity can be defined in terms of elementary charge  $e$ , the number density of conducting ions  $\rho$ , and the mobility of

conducting ions  $\mu$ .

$$\kappa_{\text{DC}} = e\rho\mu \quad (4-6)$$

Furthermore, the  $\rho$  and  $\mu$  can be estimated using a physical model of electrode polarization based on the Macdonald and Coelho model.<sup>17-19</sup> In the Macdonald and Coelho model, the electrode polarization is treated as a simple Debye relaxation and the loss tangent is defined in terms of the electrode polarization time  $\tau_{\text{EP}}$  and the conductivity time  $\tau_{\kappa}$ .<sup>20</sup>

$$\tan \delta = \frac{\omega\tau_{\text{EP}}}{1 + \omega^2\tau_{\text{EP}}\tau_{\kappa}} \quad (4-7)$$

Then, this model provides the  $\rho$  and  $\mu$  in terms of  $\tau_{\text{EP}}$  and  $\tau_{\kappa}$ .

$$\rho = \frac{1}{\pi d_{\text{B}} L^2} \left( \frac{\tau_{\text{EP}}}{\tau_{\kappa}} \right)^2 \quad (4-8)$$

$$\mu = \frac{eL^2\tau_{\kappa}}{4\tau_{\text{EP}}^2 kT} \quad (4-9)$$

where  $l_{\text{B}} \equiv e^2/4\pi\epsilon_s\epsilon_0 kT$  is the Bjerrum length and  $L$  is the gap between electrodes.  $k$  and  $T$  are respectively denote the Boltzmann constant and absolute temperature.  $\epsilon_s$  is the measured static relative permittivity before the electrode polarization and  $\tau_{\kappa}$  is defined as  $\tau_{\kappa} \equiv \epsilon_s\epsilon_0 / \sigma_{\text{DC}}$ .

In Figure 4-3, the fitting results of loss tangent at selected temperatures are shown.

Figures 4-8 (a) and (b) show that the  $T_{\text{g}}$ -independent mobility of conducting ions,  $\mu$ , follows the VFT type equation at  $T > T_{\text{g}}$  while the Arrhenius type temperature dependence is observed at  $T < T_{\text{g}}$ . The temperature dependence of  $\mu$  is comparable to that of  $\tau_{\text{HN}}$  (not shown

here). Therefore, the analysis using the Macdonald and Coelho model holds valid in these systems. The change in magnitude of the mobility,  $\mu$ , by the change of alkyl chain lengths spans two decades while that for the variation of counter anion species extends over more than four decades.

Figure 4–8 (c) and (d) shows the  $T_g$ -independent number density of conducting ions,  $\rho$ , normalized by the total number density of ions,  $\rho_0 = d_{\text{PIL}}N_A/M_0$ . Here,  $N_A$  is the Avogadro number.  $d_{\text{PIL}}$  and  $M_0$  are the density for each PIL and the molar mass of repeating units. The  $d_{\text{PIL}}$  values for PC<sub>4</sub>-TFSI, PC<sub>4</sub>-TfO, and PC<sub>4</sub>-BF<sub>4</sub> are reported in the literature.<sup>6</sup> The others are assumed as  $d_{\text{PIL}} = 1.516 \text{ g cm}^{-3}$  which is the value for PC<sub>4</sub>-TFSI. The change of magnitude of  $\rho$  was less than two decades. Thus, the drastic decrement of  $\kappa_{\text{DC}}$  can be explained by the deceleration of ionic mobility.

The temperature dependence of conducting ions above  $T_g/T < 0.8$  for the PILs having different alkyl chain lengths linearly increases with increasing temperatures and can be described by the Boltzmann distribution. At  $T_g/T > 0.8$ , except for PC<sub>2</sub>-TFSI, the  $\rho/\rho_0$  much gradually decreases with increasing temperatures. Similar temperature dependence was observed in the PILs having different counter anion species. The onset temperature for the transition depended on the counter anion species. Colby et al<sup>13</sup> reported the same transition behavior of  $\rho$  around at the glass transition temperature of PILs. They proposed the simple model for the conducting mechanism in which the segmental motion is dominant above  $T_g$  while the hopping of free anions is dominant below  $T_g$ . For the PC<sub>4</sub>-PFSI and PC<sub>4</sub>-HFSI systems, as be mentioned in chapter 3, the segmental motion of polymer chains are highly restricted and therefore the transition into the Arrhenius type temperature dependence is observed at higher temperatures than the  $T_g$ . As for the PC<sub>2</sub>-TFSI system, the  $\rho/\rho_0$  drastically decreases with increasing temperatures. This might be because the TFSI anions are trapped in local environment. The TFSI anions have the tendency to form ionic aggregates as be mentioned in

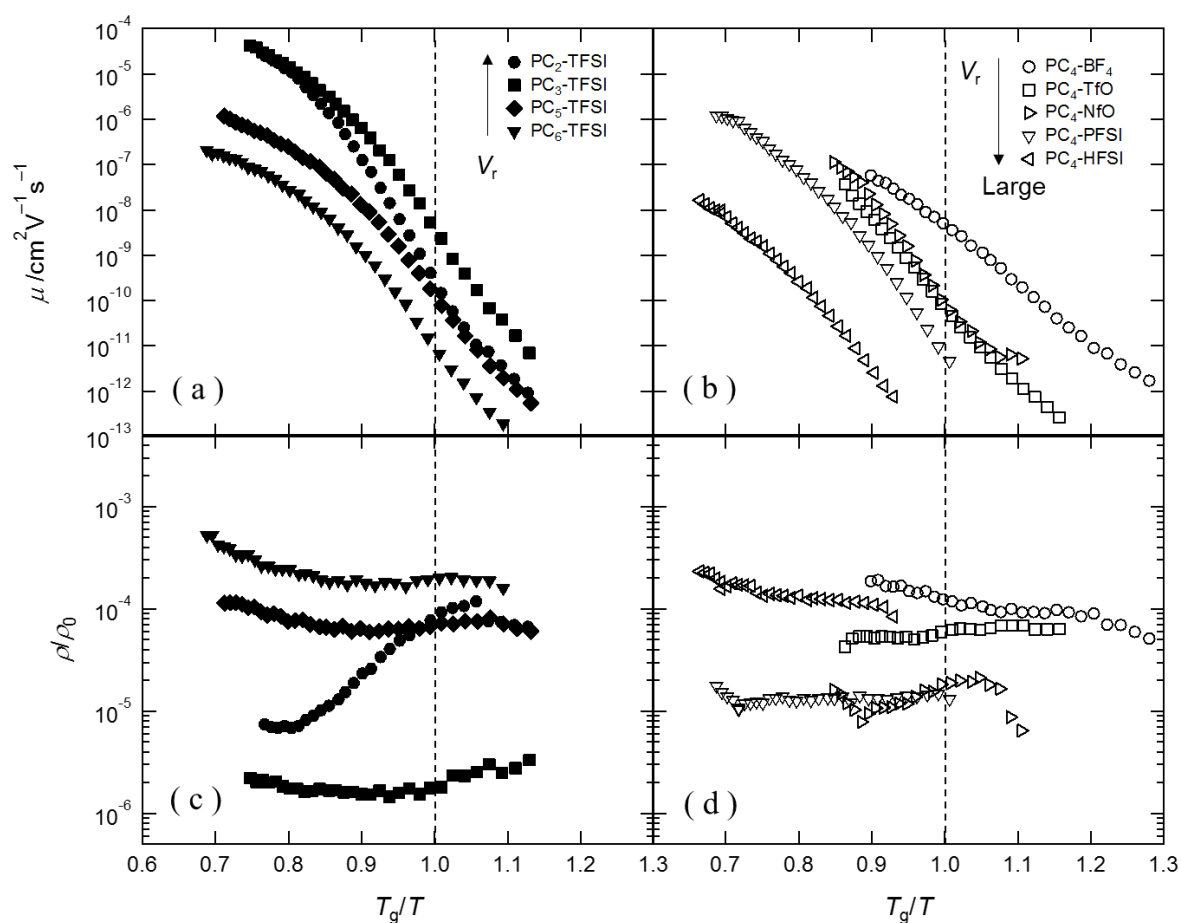


Figure 4–8. The number density of conducting ions and their mobility. (a) and (c) for the dependence of alkyl chain lengths. (b) and (d) for the dependence of counter anion species.

#### 4-3-6 Nanoscale Morphology

At temperatures lower than glass transition temperatures of PILs, ions hop through the spacing in PIL matrix. Therefore, the structural studies such as X-ray scattering can give insight into the spacing for ionic transport. Figure 4–9 shows the X-ray patterns with three unique peaks corresponding to the correlation lengths characterizing morphology of the PILs. These lengths are related to the scattering wave vector  $q_x$  according to Bragg's law,  $d_x = 2\pi/q_x$ . The poly(1-*n*-alkyl-3-vinylimidazolium)-based PILs exhibit scattering peaks at low values of  $q$  (3.4 – 4.8

$\text{nm}^{-1}$ ). This spacing reflects the main chain correlation length (backbone-to-backbone) and varied with the alkyl chain length yielding:  $d_b = (0.12 \text{ nm} / \text{CH}_2)m + d_0$ , with  $d_0 = 1.08 \text{ nm}$  and  $m = 2, 3, 5,$  and  $6$ . The scattering peaks at higher values of  $q$  ( $12 - 15.3 \text{ nm}^{-1}$ ) reflect the side-group correlation length (pendant-to-pendant,  $q_p$ ), which varied substantially with the volumes of the anions. The intermediate peak ( $q_i = 7.4 - 8.7 \text{ nm}^{-1}$ ) is associated with the polar group correlation length (anion-to-anion). The assignment of the three characteristic peaks are in accord with previous experimental studies.<sup>10-12</sup>

Figure 4–10 shows that systematic variation of the alkyl chain lengths has an important impact on the backbone-to-backbone spacing, whereas counterion sizes is not significantly influence any correlation lengths. The change in  $d_i$  and  $d_p$  is less than  $0.1 \text{ nm}$ , which is comparable to the increment in minimum length of counter anions. Therefore, this result suggests that the spacing for ionic transport spreads with increasing the alkyl chain lengths while such the spacing is independent of the ionic sizes of counter anions. The smaller counterions can easily diffuse through the polymer matrix and hence the mobility of conducting ions is increased with decreasing the sized of counter anions. However,  $\text{PC}_6\text{-TFSI}$  having larger spacing showed the lowest mobility of conducting TFSI anions. To explain the results, I propose that the apolar alkyl groups form non-ion conducting region. It would be reasonable that the conducting ions move through the polar region in PILs. Therefore, longer alkyl chains could behave as the obstacles for ion diffusion and hence the mobility is decreased with increasing the alkyl chain lengths.

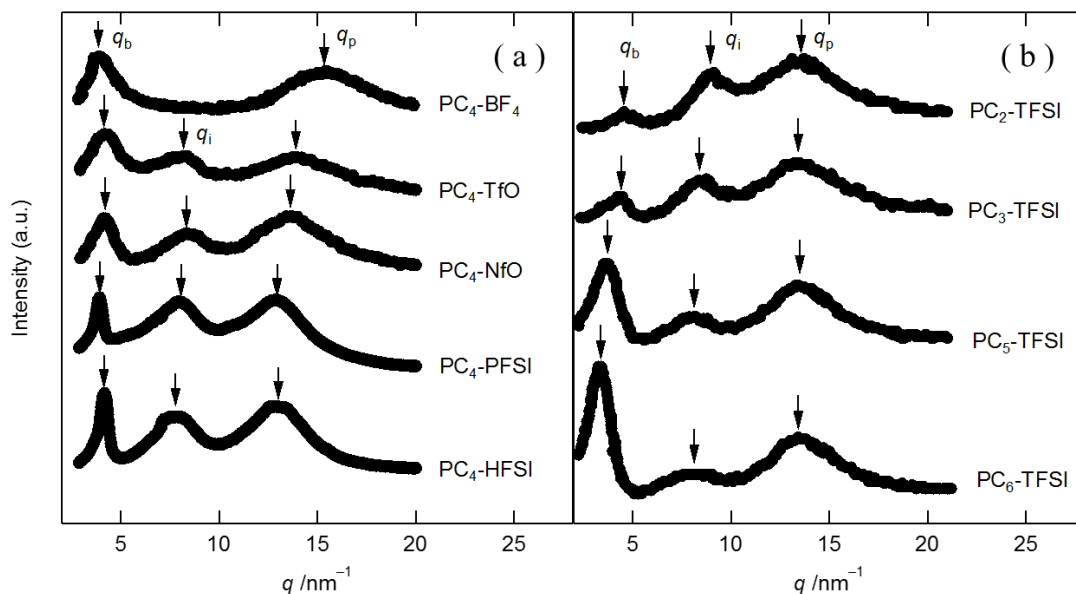


Figure 4–9. Wide-angle X-ray scattering profiles at room temperature for (a) PC $n$ -TFSI where  $n$  is the number of alkyl chains ranging from  $n=2$  to  $n=6$ . (b) PC $_4$ -X where X denotes the counter anion species.

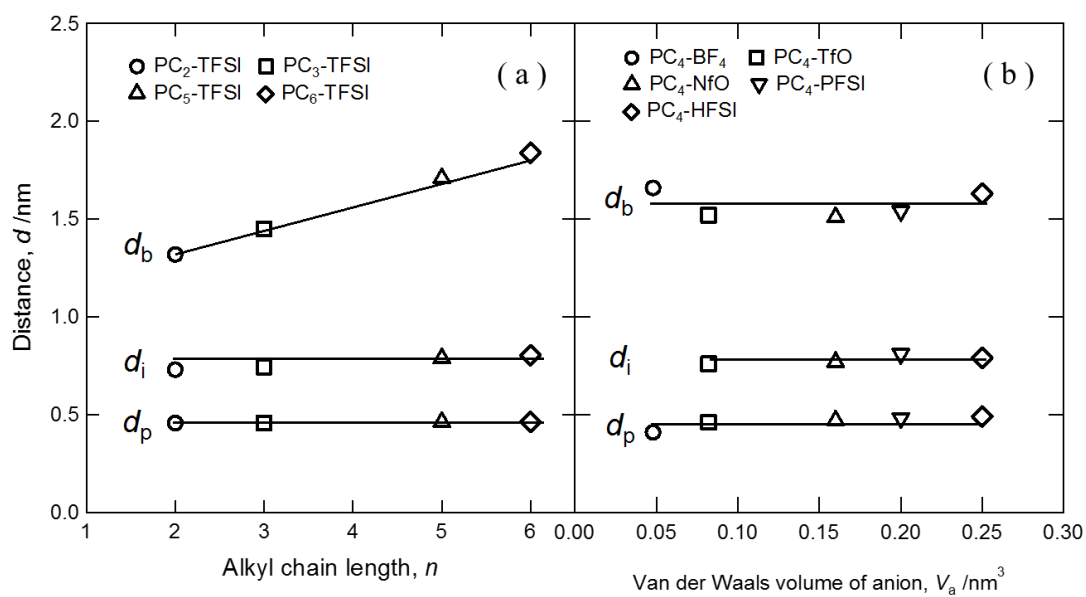


Figure 4–10. (a) Correlation lengths  $d_b$ ,  $d_i$ , and  $d_p$  as a function of the number of alkyl chain length. (b) Correlation lengths  $d_b$ ,  $d_i$ , and  $d_p$  as a function of the van der Waals volume of counter anions.

#### 4-3-7 Decoupling of Ion Transport from Segmental Dynamics

Here, in this section, the transition from VFT to Arrhenius type temperature dependence of  $\kappa_{DC}$  (or  $\tau_{HN}$ ) is considered. In the ordinary polymer electrolytes such as lithium ions in poly(ethylene oxide),<sup>8,9</sup> the ion transport is controlled by the segmental dynamics of polymers in which both of  $\kappa_{DC}$  and  $\tau_0$  follow the VFT equation at temperatures lower than their glass transition temperatures. Aprotic molecular ILs have revealed that the ionic conductivity is mainly controlled by structural dynamics.<sup>21-23</sup> The transition behavior strongly suggests that the ionic conductivity is dominated by contributions from hopping conduction in the polymeric matrix.

In order to estimate the ionic conductivity controlled only by segmental dynamics, the VFT type fitting curves are plotted in Figure 4-7 (c) and (d) using the same parameters as those for the segmental relaxation. For the PC<sub>6</sub>-TFSI system, the ionic conductivity is strongly decoupled from the segmental motion. In contrast, for the PC<sub>4</sub>-PFSI system, the ionic conductivity is closely coupled with the polymer motion till  $T_g/T = 1$  and then decoupled at  $T_g/T > 1$ . From these results, it can be said that the decoupling behavior depends on molecular structures of PILs.

Table 4-2 shows the activation energies obtained from the Arrhenius fit shown in Figure 4-7. The activation energies are comparable with each other, indicating that the ionic conduction is dominated only by the same origin, i.e. hopping conduction, at temperatures lower than their glass transition temperatures. On the other hand, the decoupling behavior at  $T > T_g$  strongly depends on the counter ion size as shown in Figure 4-7.

In order to estimate the degree of decoupling between the segmental dynamics and ionic conductivity, the decoupling exponent  $g (= 1 - \gamma)$  was estimated following the procedure proposed by Sokolov et al. Figure 4-11 shows the relationship between the molar conductivity  $\Lambda$  and the segmental relaxation time  $\tau_0$  on a double-logarithmic scale. The molar conductivity

$\Lambda$  was calculated by the following equation,  $\Lambda = \kappa_{\text{DC}} N_{\text{A}} / \rho$ . The relation characterized by a power law equation  $\Lambda \propto \tau_0^{-\gamma}$  was observed for all the PILs investigated. Here,  $g = 0$  ( $\gamma = 1$ ) implies that the ion transport is completely coupled with the segmental dynamics. For all the samples, the decoupling exponents are larger than zero.

Figure 4–12 shows the decoupling exponent as a function of volume ratio  $V_r$  of counter anions ( $V_{\text{a}}$ ) to cations ( $V_{\text{c}}$ ) estimated by the same method in Chapter 2. The linear relationship was observed. The degree of decoupling between the segmental dynamics and ion transport became larger as the volume ratio of anions to cations is decreased. This result indicates that the smaller anions can diffuse by the hopping process in polymer matrix.

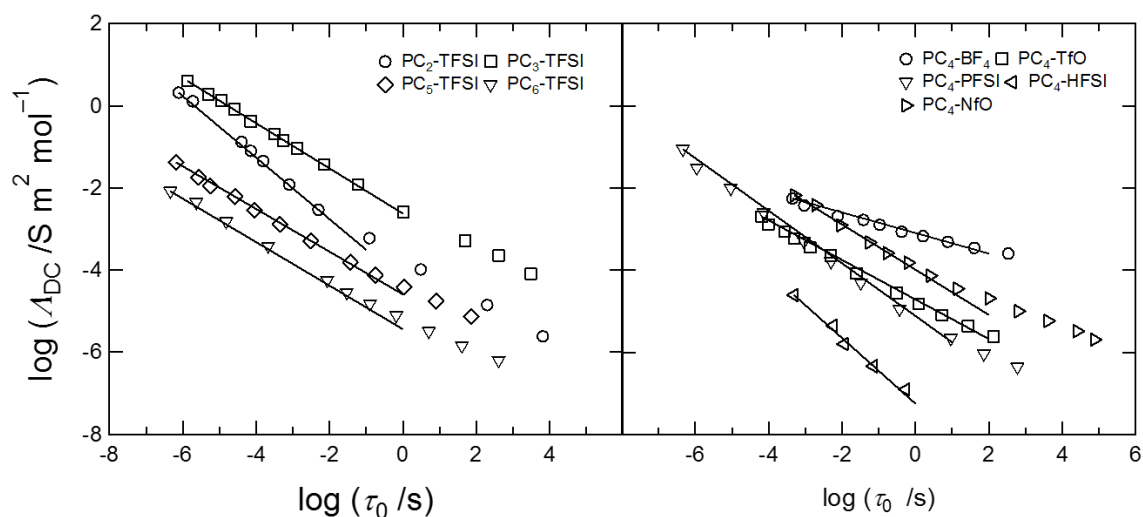


Figure 4–11. Molar conductivities as a function of the segmental relaxation time. Left: dependence of the alkyl chain lengths. Right: dependence of the counter anion species.

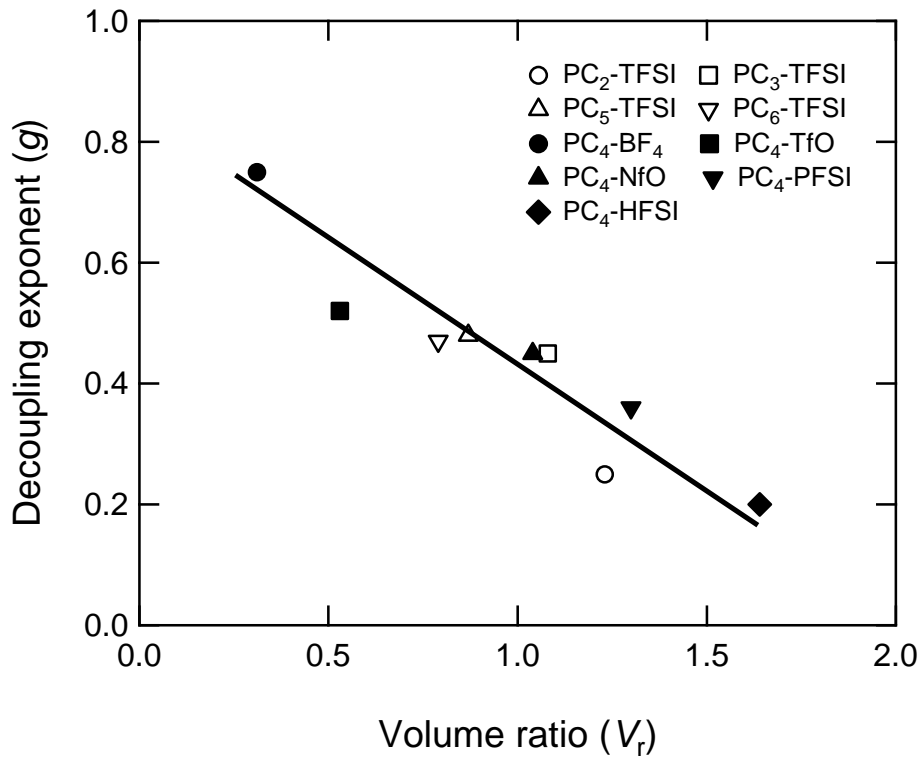


Figure 4–12. Decoupling exponents as a function of the volume ratio of counter anions to cations.

Table 4–2. Activation energy for ion transport at  $T < T_g$ .

	PC <sub>2</sub> -TFSI	PC <sub>3</sub> -TFSI	PC <sub>5</sub> -TFSI	PC <sub>6</sub> -TFSI
$E_a$ /kJ mol <sup>-1</sup>	112	102	101	101
$g$	0.25	0.45	0.48	0.47
	PC <sub>4</sub> -BF <sub>4</sub>	PC <sub>4</sub> -TfO	PC <sub>4</sub> -PFSI	PC <sub>4</sub> -HFSI
$E_a$ /kJ mol <sup>-1</sup>	97.2	98.2	150	NA
$g$	0.75	0.52	0.36	0.2
	PC <sub>4</sub> -NfO			
$E_a$ /kJ mol <sup>-1</sup>	111			
$g$	0.45			

#### 4-4 Conclusion

The linear viscoelastic measurements, broadband dielectric spectroscopy, and wide-angle X-ray scattering were performed for a systematic series of poly(1-alkyl-3-vinylimidazolium)-based ionic liquids with various counter anions to clarify the relationship between ion transporting mechanism and molecular structures of PILs. The  $T_g$ -independent ionic conductivity of imidazolium-based polyILs increases with decreasing the alkyl chain lengths and volumes of the counterions. Variation of the anion is found to result in differences in the  $T_g$ -independent ionic conductivity spanning four orders of magnitude, in contrast to six-fold changes obtained from variation in alkyl chain lengths. From the analysis of electrode polarization, it is found that the drastic decrement of  $\kappa_{DC}$  can be explained by the deceleration of ionic mobility. The smaller anions can move more freely in polymer matrix. From the comparison between the characteristic times for segmental motion of polymer chains and ion conduction, we found that the degree of decoupling between the segmental motion of polymers and the ionic conductivity becomes larger as ionic sizes of counterions are decreased. As a result, we found that the conductivity primarily involves hopping of small counterions through channels determined by the morphology of the PILs.

#### 4-5 References

- (1) Ohno, H.; Ito, K. *Chem. Lett.* **1998**, 751-752.
- (2) Nakamura, K.; Saiwaki, T.; Fukao, K.; Inoue, T. *Macromolecules* **2011**, 44, 7719-7726.
- (3) Sangoro, J. R.; Iacob, C.; Agapov, A. L.; Wang, Y.; Berdzinski, S.; Rexhausen, H.; Strehmel, V.; Friedrich, C.; Sokolov, A. P.; Kremer, F. *Soft Matter* **2014**, 10, 3536-3540.
- (4) Batra, D.; Seifert, S.; Firestone, M. A. *Macromol. Chem. Phys.* **2007**, 208, 1416-1427.
- (5) Lee, M.; Choi, U. H.; Colby, R. H.; Gibson, H. W. *Chem. Mater.* **2010**, 22, 5814-5822.
- (6) Nakamura, K.; Fukao, K.; Inoue, T. *Macromolecules* **2012**, 45, 3850-3858.
- (7) Nakamura, K.; Saiwaki, T.; Fukao, K. *Macromolecules* **2010**, 43, 6092-6098.
- (8) Yoshida, K.; Manabe, H.; Takahashi, Y.; Furukawa, T. *Electrochim. Acta* **2011**, 57, 139-146.
- (9) Furukawa, T.; Mukasa, Y.; Suzuki, T.; Kano, K. *J Polym Sci Pol Phys* **2002**, 40, 613-622.

- (10) Green, M. D.; Salas-de la Cruz, D.; Ye, Y. S.; Layman, J. M.; Elabd, Y. A.; Winey, K. I.; Long, T. E. *Macromol. Chem. Phys.* **2011**, 212, 2522-2528.
- (11) Salas-de la Cruz, D.; Green, M. D.; Ye, Y. S.; Elabd, Y. A.; Long, T. E.; Winey, K. I. *J Polym Sci Pol Phys* **2012**, 50, 338-346.
- (12) Allen, M. H.; Wang, S.; Hemp, S. T.; Chen, Y.; Madsen, L. A.; Winey, K. I.; Long, T. E. *Macromolecules* **2013**, 46, 3037-3045.
- (13) Choi, U. H.; Ye, Y. S.; de la Cruz, D. S.; Liu, W. J.; Winey, K. I.; Elabd, Y. A.; Runt, J.; Colby, R. H. *Macromolecules* **2014**, 47, 777-790.
- (14) Mecerreyes, D. *Prog. Polym. Sci.* **2011**, 36, 1629-1648.
- (15) Steeman, P. A. M.; Vanturnhout, J. *Macromolecules* **1994**, 27, 5421-5427.
- (16) Wubbenhorst, M.; van Turnhout, J. *J. Non-Cryst. Solids* **2002**, 305, 40-49.
- (17) Macdonald, J. R. *Phys Rev* **1953**, 92, 4-17.
- (18) Coelho, R. *Rev Phys Appl* **1983**, 18, 137-146.
- (19) Coelho, R. *Elsevier: New York* **1979**.
- (20) Klein, R. J.; Zhang, S. H.; Dou, S.; Jones, B. H.; Colby, R. H.; Runt, J. *J. Chem. Phys.* **2006**, 124.
- (21) Sangoro, J. R.; Kremer, F. *Acc. Chem. Res.* **2012**, 45, 525-532.
- (22) Sangoro, J. R.; Iacob, C.; Serghei, A.; Friedrich, C.; Kremer, F. *PCCP* **2009**, 11, 913-916.
- (23) Wojnarowska, Z.; Paluch, M. *J Phys-Condens Mat* **2015**, 27.

---

## CHAPTER 5

# Viscoelastic Properties and Local Dynamics of Polyelectrolyte/Ionic Liquid Solutions

---

### 5-1 Introduction

Polyelectrolytes (PELs) are polymers having dissociable ions on repeating units. They are of importance in nature and essential for our life. Understanding PELs is necessary for a fundamental understanding of biological systems and biological processes since many biological polymers such as DNA are PELs. Moreover, understanding properties enable us to develop ideal materials. Owing to these social needs, a lot of investigations have already carried out and found that the electrostatic interaction plays an important role in PEL properties.

In solutions, for example, it is well-known that PEL polymer chains tend to stretch due to the interplay among the strong Coulombic repulsion between nearby charges. Accordingly, viscoelastic properties such as the viscosity can be changed.<sup>1-8</sup> However, it is not understood well enough how local dynamics of PELs in solutions are affected by the electrostatic interaction since almost all of reports were conducted in aqueous solutions due to the solubility problem, in which it is difficult to capture viscoelastic properties at high frequencies. In order to access these regions, viscous, low volatile and glass-forming solvents for PEL are required.

For viscoelastic measurements, ILs can be utilized as solvents since many of ILs have a sufficient viscosity and exhibit the glass transition below accessible temperatures. In addition, ILs are composed of only ions and hence can have a capability to dissolve PELs.

In this study, viscoelasticity and birefringence under oscillatory shear flow were measured for the solutions of polymerized ionic liquids in ionic liquids over a wide range of frequency from the flow to the glassy zone in order to clarify effects of the electrostatic

interaction on the Rouse segment size and its concentration dependence. For the case of electrically neutral polymers such as polystyrene in a dilute solution, it is known that the molar mass of Rouse segment is approximately five times as large as that in bulk state.<sup>9</sup> We will discuss this ratio as a measure of effects of Coulombic force. In addition, our recent study using the solutions of cellulose in ILs reported that the appearance of additional relaxation modes between solvent and polymer global motions in the vicinity of glass transition zone was suggested.<sup>10</sup> Whether or not additional modes for the solutions of PILs in ILs are shown is also our interest.

## 5-2 Experimental Methods

**Materials.** In order to elucidate the effects of counter anion species, three types of PELs were used. Figure 5-1 shows the chemical structures of a repeating unit of PEL. PC<sub>4</sub>-TFSI and PC<sub>4</sub>-BF<sub>4</sub> were synthesized following the same procedure described in Chapter 2. PC<sub>4</sub>-Cl was synthesized by the slightly modified procedure where 1-chlorobutane (WAKO Pure Chemicals) was used instead of 1-bromobutane. The molecular weights of PELs are different each other. However, from the linear viscoelastic response for PELs in bulk state, the molecular weights were found to be high enough so that local dynamics for PELs can be the same.

1-methyl-3-n-octylimidazolium bis(trifluoromethanesulfonyl)imide (OmimTFSI) and 1-butyl-3-methylimidazolium tetrafluoroborate (BmimBF<sub>4</sub>) were purchased from ionic liquids technologies Inc. and used as solvents for PC<sub>4</sub>-TFSI and PC<sub>4</sub>-BF<sub>4</sub> respectively. 1-butyl-3-methylimidazolium chloride (BmimCl) was purchased from WAKO Pure Chemicals and used as a solvent for PC<sub>4</sub>-Cl. OmimTFSI, BmimBF<sub>4</sub>, and BmimCl were sufficiently dried before use. The chemical structures of OmimTFSI, BmimBF<sub>4</sub>, and BmimCl are depicted in Figure 5-1. A previous study reported that dissolved ions in ILs changed structures of ionic liquids, suggesting that dissociated ions from PELs affect their dynamics and hence make discussion complicated.

Therefore, we fixed anions of ILs with those of PELs for simplicity. For the sake of comparison, electrically neutral solutions of standard polystyrene (PS) with  $M_w=1.11 \times 10^6$  and  $M_w/M_n=1.08$  (TOSOH) in tritolyl phosphate (TCP) (Wako; 98%) were used.

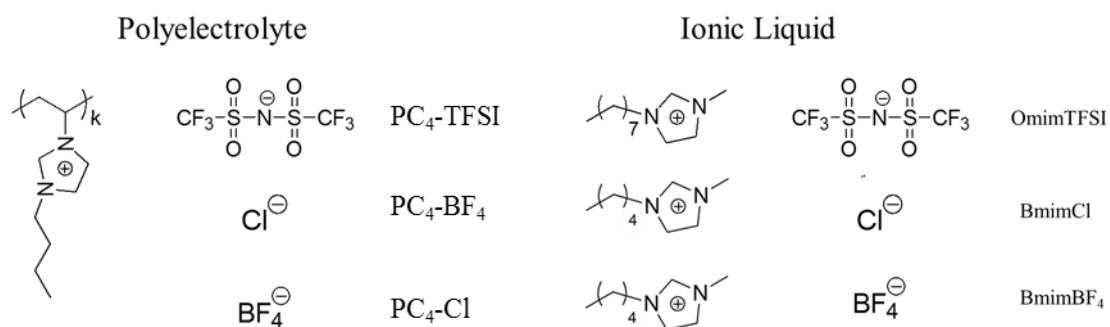


Figure 5–1. Chemical structures of PELs and ionic liquids.

**Sample Preparation.** Mixtures with relatively low concentrations were prepared by the direct weighting of the components into a small vial and then stirred at 65°C overnight. After the mixing at 65°C, solutions were then annealed under vacuum. The volatility of TCP is low enough that there can be no measurable change in the solution mass.

On the other hand, mixtures with high concentrations were prepared via co-solvent method. For PC<sub>4</sub>-BF<sub>4</sub>/BmimBF<sub>4</sub> systems and PC<sub>4</sub>-TFSI/OmimTFSI systems, acetone solutions into a small vial were slowly dried at room temperature and then the solutions were dried at 65°C under vacuum for a week until complete evaporation of acetone. For PC<sub>4</sub>-Cl/BmimCl, deionized water was used as a solvent. The mass concentration of polymer  $c$  for each system was calculated from the following simple equation,  $c = w_{\text{polymer}}d_{\text{solvent}}/w_{\text{solvent}}$  where  $w_{\text{polymer}}$  and  $w_{\text{solvent}}$  are the polymer and solvent amounts, respectively.  $d_{\text{solvent}}$  is the density of solvent ( $d_{\text{OmimTFSI}} = 1.32 \text{ gcm}^{-3}$ ,  $d_{\text{BmimBF}_4} = 1.12 \text{ gcm}^{-3}$ ,  $d_{\text{BmimCl}} = 1.08 \text{ gcm}^{-3}$ , and  $d_{\text{TCP}} = 1.17 \text{ gcm}^{-3}$ ). Thus, the value of  $c$  for solutions with high concentration has an error.

Hereafter, I will abbreviate each solution as X-*w* where X is the counter anion species and *w* is the weight percent concentration. The values of *c* are summarized in Table 5–1. For the case of electrically neutral systems, the PS-*w* is used as their abbreviation.

Table 5–1. Sample codes and concentrations of test solutions.

	TFSI–1	TFSI–3	TFSI–5	TFSI–10	TFSI–50
<i>c</i> /g cm <sup>–3</sup>	0.0132	0.0409	0.0697	0.147	0.457
	BF <sub>4</sub> –1	BF <sub>4</sub> –3	BF <sub>4</sub> –5	BF <sub>4</sub> –50	Cl–1
<i>c</i> /g cm <sup>–3</sup>	0.0121	0.0372	0.0635	0.457	0.0132
	PS–1	PS–3	PS–50		
<i>c</i> /g cm <sup>–3</sup>	0.0133	0.0406	0.482		

### **Methods.**

*a) Thermal Analysis.* The glass transition temperature,  $T_g$ , was determined using a differential scanning calorimetry (EXSTAR6000, Seiko Instruments Inc.) with 10 K/min cooling and heating rates. Samples of 12–15 mg were dried in open pans at 65°C under vacuum before being hermetically sealed in the pans. Temperature ramp was cycled in a temperature range from 30°C to –120°C. The  $T_g$  was determined as the midpoint of the heat capacity change in the second cycle.

*b) Linear Viscoelasticity.* Linear viscoelastic measurements of PEL or PS solutions were carried out using a conventional rheometer (ARES-G2 system, TA Instruments) with a parallel plate fixture having 25 mm in diameter. For the measurements around the glassy zone, a handmade parallel plate fixture having 4 mm in diameter was used. Instrument compliance was carefully corrected with the method reported by McKenna et al.<sup>11, 12</sup> All samples were dried

under vacuum at 65°C before use. At each temperature ranging from -85°C to 60°C, the storage and the loss modulus were measured in a frequency range of  $10^{-1}$ – $10^2$  rad/s with small strain in linear viscoelastic regime.

*c) Oscillatory Flow Birefringence in Linear Regime.* Frequency dependence of strain-induced birefringence,  $\Delta n^*(\omega)$ , under oscillatory small shear deformation was measured using the handmade apparatus and  $G^*$  was also measured simultaneously with the same apparatus. Details of this apparatus are described in Chapter 2. In order to check the reliability of the data, the complex shear modulus,  $G^*$ , was measured simultaneously and compared with those obtained with ARES-G2 system.  $K^*$  and  $G^*$  were determined in a temperature range (-85–50°C) and a frequency range ( $10^{-2}$ – $10^2$  Hz).

## 5-3 Results and Discussion

### 5-3-1 Thermal Characterization

Figure 5-2 illustrates the DSC traces for PC<sub>4</sub>-TFSI/OmimTFSI solutions and neat OmimTFSI. The  $T_g$  for neat OmimTFSI was -85°C, which is in good agreement with the  $T_g$  value reported previously.<sup>13</sup> The  $T_g$  for solutions with low concentrations ( $c < 10$  wt%) shows almost the same values as neat OmimTFSI, while the  $T_g$  for TFSI-50 are shifted to higher temperatures and the width of heat flow jump are significantly broadened, similarly to the case of PS/DBP solutions reported by Lodge et al.<sup>14</sup> For some cases with other polymer solutions, two  $T_g$ s were reported. Low- $T_g$  and high- $T_g$  were respectively attributed to the glass transitions of solvent and polymer components. Lodge and McLeich explained two  $T_g$ s of solutions with the concept of self-concentration.<sup>14</sup> However, in the present system, two  $T_g$ s are not clearly observed.

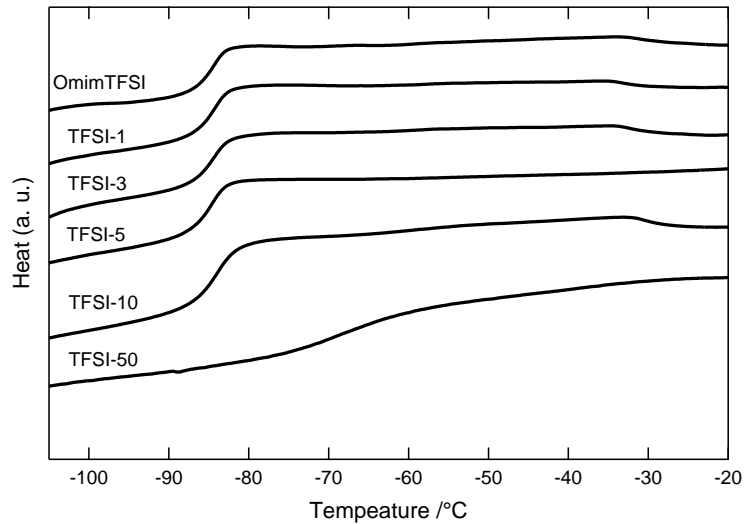


Figure 5–2. DSC traces for PC<sub>4</sub>-TFSI/OmimTFSI solutions.

### 5–3–2 Overview of Modulus and Strain-Optical Coefficient for TFSI–1

Figure 5–3 displays the composite curves of  $G^*$  and  $K^*$  for TFSI–1 and for PS–1 constructed using the reduced variables. The reference temperature was chosen as  $T_r = T_g + 35\text{K}$ . We did not use any vertical shift for superposition of both  $G^*$  and  $K^*$ . The time temperature superposition (TTS) worked very well for both systems over the measured temperature range. The frequency dependence of  $G^*$  and  $K^*$  for TFSI–1 and PS–1 seems similar. Moreover, both for TFSI–1 and PS–1, the sign of  $K'$  and  $K''$  at low frequencies is negative while it is positive at high frequencies. Hereafter, we will discuss the difference of relaxation mechanisms between TFSI–1 and PS–1. The similar frequency dependence of  $G^*$  and  $K^*$  for BF<sub>4</sub>–1 and Cl–1 was obtained and there was no critical difference in that for the TFSI–1 system.

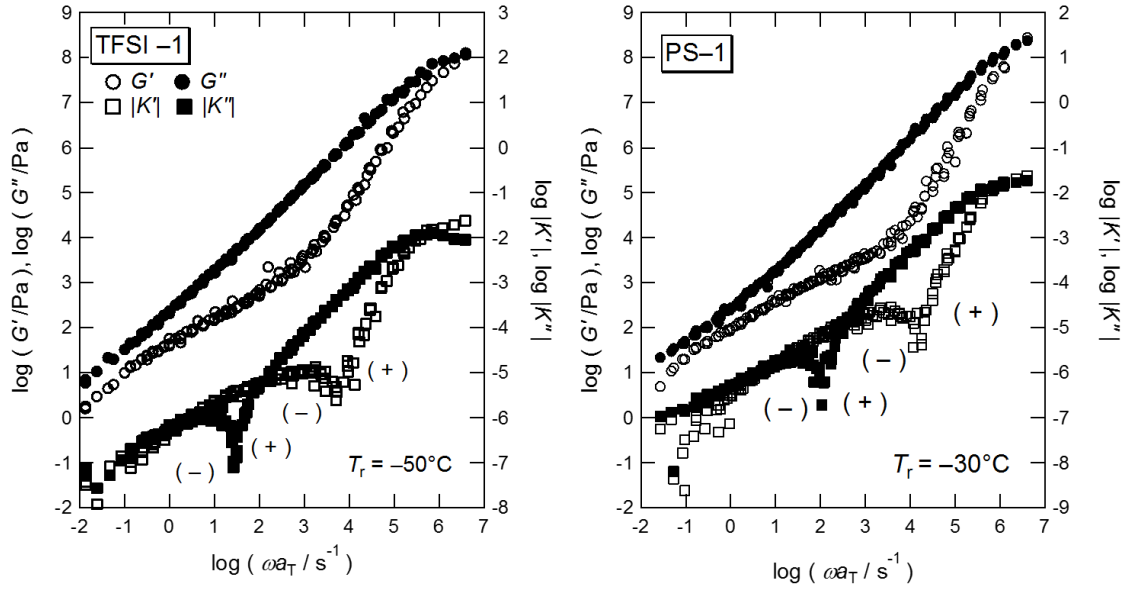


Figure 5–3. Composite curves for the complex modulus and the complex shear strain-optical coefficient for TFSI–1 (left) and PS–1 (right).

### 5–3–3 Overview of Modulus and Strain-Optical Coefficient for TFSI–50

Figure 5–4 compares the composite curves of  $G^*$  for TFSI–50 and PS–50 constructed using the reduced variables. The reference temperature was chosen as  $T_r = T_g + 35\text{K}$ . The TTS hold valid over the measurement temperature range. The two distinguishing peaks in  $G''$  in the glassy zone ( $\omega a_T > 10^0 \text{ s}^{-1}$ ) indicated by arrows in Figure 5–4 are observed for TFSI–50 while the  $G''$  for PS–50 keeps its modulus constant in the same frequency region. These results suggest that the TFSI–50 undergoes the different relaxation processes from the PS–50. As discussed below, applying the simultaneous measurements of  $G^*$  and  $K^*$  shown in Figure 5–4, the assignment of relaxations will be carried out based on the MSOR analysis.

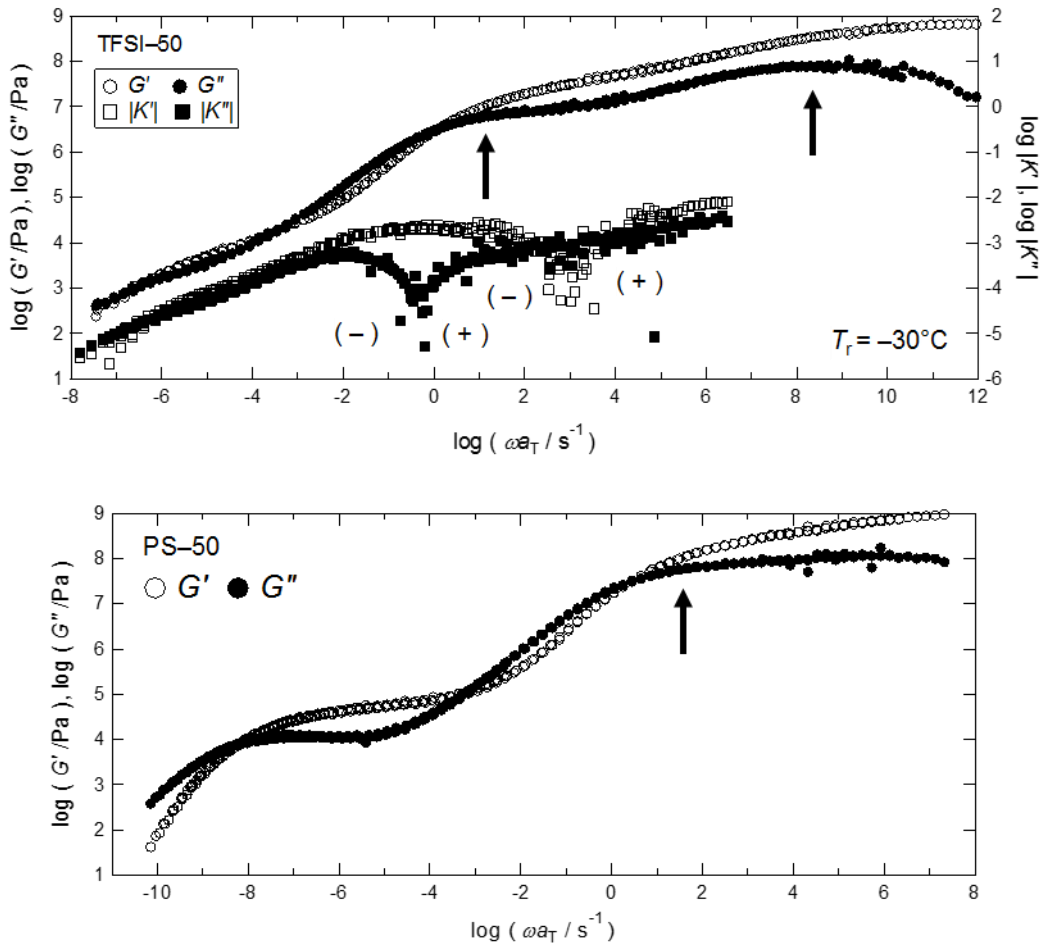


Figure 5–4. Top: Composite curves of  $G^*(\omega)$  and  $K^*(\omega)$  for TFSI–50. Bottom: Composite curve of  $G^*(\omega)$  for PS–50.

### 5–3–4 Estimation of the Rouse Segment Size

For the case of dilute solutions, the frequency dependence of the complex modulus,  $G^*(\omega)$ , can be assumed to be phenomenologically represented as a simple summation of polymer contribution  $G_p^*(\omega)$  and solvent contribution  $G_s^*(\omega)$ .<sup>15</sup> For the case of storage modulus, we obtain

$$G'(\omega) = G_p'(\omega) + G_s'(\omega) \quad (5-1)$$

The polymer contribution may further assumed to be composed of Rouse-Zimm modes and local modes.

$$G_p'(\omega) = G_{RZ}'(\omega) + G_{local}'(\omega) \quad (5-2)$$

In order to estimate  $G_p'(\omega)$ , we assume that  $G_s'(\omega)$  can be written as  $A_G\omega^\alpha$  at low frequencies, and subtract the solvent contribution from experimental  $G'(\omega)$  data.

$$G_p'(\omega) = G'(\omega) - A_G\omega^\alpha \quad (\alpha \sim 2) \quad (5-3)$$

where  $A_G$  is a constant representing elastic contribution of solvent.

Thus obtained spectra of  $G_p'(\omega)$  was depicted in Figure 5-5.  $G_p'(\omega)$  monotonically increases with increasing frequency even at high frequencies. The limiting value of  $G_p'(\omega)$  at high frequencies,  $G_p'(\infty)$ , cannot be obtained by this method. Similar behavior was also reported for Cellulose/Ionic liquid systems.<sup>10</sup> As we will discuss later, this comes from the local component of modulus, which has been argued but not clearly observed for polystyrene solutions. The similar frequency dependence of  $G_p'(\omega)$  was observed in BF<sub>4</sub>-1.

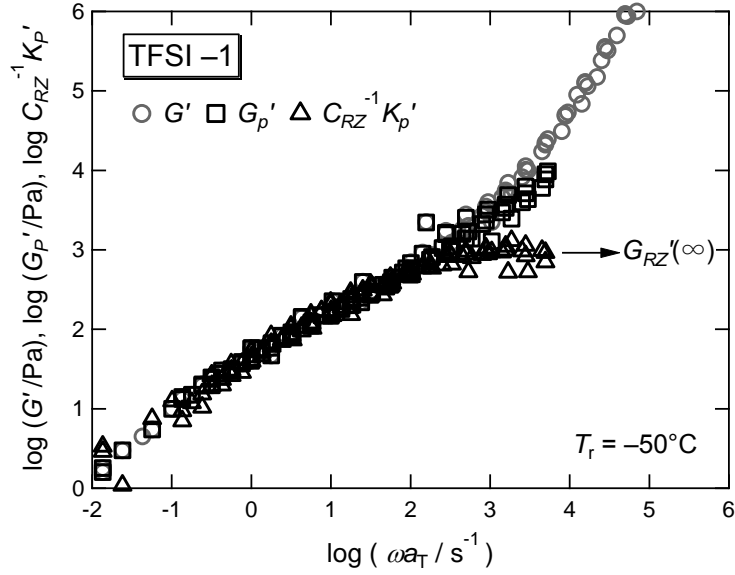


Figure 5–5. Frequency dependence of  $G'(\omega)$  and the main chain orientation term  $G_P'(\omega)$  or  $|C_{RZ}^{-1}K'(\omega)|$  calculated by subtraction and the SOR.

Alternatively, we applied the same procedure to strain-induced birefringence,  $K'(\omega)$ .

The polymer contribution is estimated with the following equation.

$$K_p'(\omega) = K'(\omega) - A_K \omega^\beta \quad (\beta \sim 2) \quad (5-4)$$

The estimated  $K_P'(\omega)$  is shown in Figure 5–5. The SOR holds well between  $K_P'(\omega)$  and  $G_P'(\omega)$  at low frequencies while it does not hold valid at high frequencies between  $K_P'(\omega)$  and  $G_P'(\omega)$ . The breakdown of SOR strongly suggests that  $G_P'(\omega)$  estimated with eq. (5–3) includes two contributions as written with eq. (5–2). Since the main component at low frequencies is originated by the orientation of segments (Rouse-Zimm modes), we modify eq. (5–4) by considering the contribution of local motion.

$$K_P^*(\omega) = C_{RZ} G_{RZ}^*(\omega) + C_{local} G_{local}^*(\omega) \quad (5-5)$$

Here the subscripts “RZ” and “local” stand for Rouse-Zimm modes and local motions of polymer chain, respectively. To our best knowledge, the local motion originates relatively high modulus, but rather small birefringence. The stress-optical coefficient for polymeric modes was determined at low frequencies and was listed in Table 5–2.

For such a case,  $C_{\text{local}} < C_{\text{RZ}}$  is satisfied and therefore eq. (5–5) can be simplified as

$$K_p^*(\omega) \sim C_{\text{RZ}} G_{\text{RZ}}^*(\omega) \quad (5-6)$$

The molar mass of Rouse segment,  $M_s$ , is estimated from the limiting modulus at high frequencies of the polymer component,  $G_{\text{RZ}}'(\infty)$ .<sup>16</sup>

$$M_s = \frac{cRT}{G_{\text{RZ}}'(\infty)} = \frac{cC_{\text{RZ}}RT}{K_{\text{RZ}}'(\infty)} \sim \frac{cC_{\text{RZ}}RT}{K_p'(\infty)} \quad (5-7)$$

Here,  $R$  is the gas constant and  $T$  is temperature.

The molar mass of Rouse segment was calculated with eq. (5–7) and listed in Table 5–2. In this calculation, the value of  $c$  was used irrespective of the degree of ion dissociation from PEL. Therefore, the listed  $M_s$  values correspond to  $M_s$  of a hypothetical chain without any dissociation of ionic parts.

At higher polymer concentration, the solvent dynamics is significantly modified by the presence of polymer chain.<sup>14, 17</sup> Therefore, the simple subtraction method for  $G'(\omega)$  using eq. (5–3) will be no longer valid. However, as shown in Figure 5–4, we found that the plateau region of  $K'(\omega)$  at  $\log(\omega a_T / \text{s}^{-1}) > 3$  was observed even at high concentration, and hence the value of  $M_s$  could be calculated by eq. (5–7). The  $M_s$  values for each systems are summarized in Table 5–2.

Table 5–2. The stress-optical coefficients of  $C_{RZ}$  and  $C_{local}$  and the Rouse segment size,  $M_s$  at the reference temperature.

Sample code	$C_{RZ} / 10^{-8} \text{Pa}^{-1}$	$ C_{local}  / 10^{-8} \text{Pa}^{-1}$	$M_s / \text{kg mol}^{-1}$
TFSI-1	-1.2	0.023	23.3
TFSI-3	-1.6	0.014	21.1
TFSI-5	-1.8	0.016	20.8
TFSI-10	-1.8	0.014	19.0
TFSI-50	-1.5	0.0095 0.0065	6.1
BF <sub>4</sub> -1	-2.0	0.035	11.8
BF <sub>4</sub> -3	-2.0	0.020	12.1
BF <sub>4</sub> -5	-2.0	0.015	12.3
Cl-1	-1.1	NA	8.9
PS-1	-0.53	NA	5.4
PS-3	-0.63	NA	5.1

### 5–3–5 Stress-Optical Coefficient for Polymer Component

As described in Chapter 1,  $C_{RZ}$  can be related with the anisotropy of polarizability of the statistical segments  $\Delta\beta$ .<sup>18</sup>

$$C_{RZ}(T) = \frac{2\pi}{45} \frac{(n+2)^2}{nkT} \Delta\beta \quad (5-8)$$

Here,  $n$  is refractive index and  $k$  is the Boltzmann constant. The anisotropy of polarizability for a repeating unit,  $\Delta\alpha$ , can be related to  $\Delta\beta$  as  $\Delta\alpha \sim \Delta\beta M_0/M_S$ . Thus, the value of  $C_{RZ}$  enables us to evaluate the dissociative state of PELs in ionic liquids under oscillatory deformation.

Figure 5–6 shows the concentration dependence of  $C_{RZ}(T_r)$  of the PC<sub>4</sub>-TFSI/OmimTFSI systems and PC<sub>4</sub>VIBF<sub>4</sub>/BmimBF<sub>4</sub> systems at their reference temperatures. Also included is  $C_{RZ}(T_r)$  of bulk PELs at their reference temperature. Assumed that the optical segment for both systems is independent of concentration similarly to the case of PS systems,<sup>19</sup> the constant  $C_{RZ}$  values within the experimental error (20%) for PC<sub>4</sub>-TFSI/OmimTFSI systems indicate that the dissociative state is similar to that in the bulk state. On the other hand, the values of  $C_{RZ}(T_r)$  for PC<sub>4</sub>-BF<sub>4</sub>/BmimBF<sub>4</sub> systems at low concentrations are five times as large as that in bulk state, indicating that the amount of ionized counter anions is larger than that in bulk state. Moreover, the similarity of values of  $C_{RZ}(T_r)$  for both systems at low concentrations suggests that the dissociative states are similar.

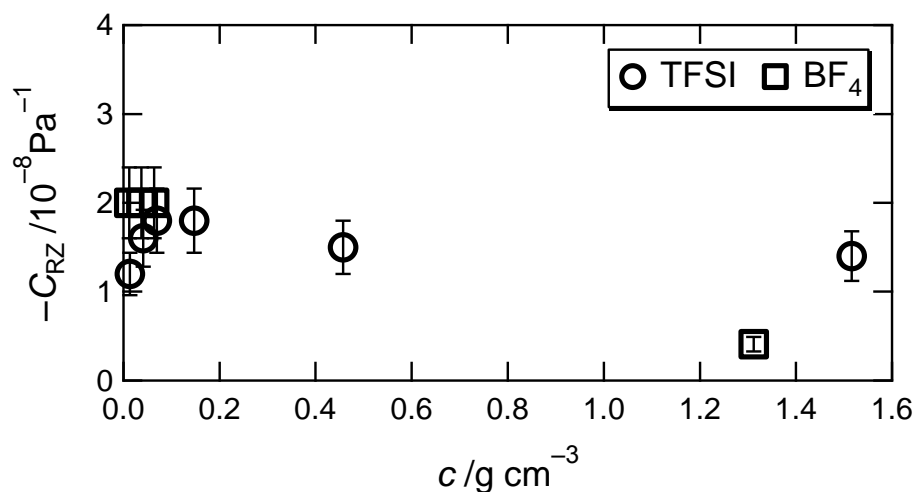


Figure 5–6. Concentration dependence of the stress-optical coefficients for polymer contribution at the reference temperature.

### 5-3-6 Rouse Segment Size and Its Concentration Dependence

As described above, the Rouse segment size in dilute solution is about 5 times larger than that in bulk. If the electrostatic interaction in dilute solutions of PEL/ionic liquid systems is sufficiently screened out, the ratio,  $M_s/M_{s,\text{bulk}}$  should agree with that for dilute solutions of electrically neutral systems. The ratio for TFSI-1 and BF<sub>4</sub>-1 is respectively 4.2 and 4.4, indicating that local dynamics of PELs in the matrix where the electrostatic interaction is screened out behave as those of electrically neutral polymers.

Larson<sup>20</sup> estimated the crossover condition between relaxation dominated by diffusive motion and that controlled by activated bond rotation. The number of Kuhn steps per the Rouse segment,  $N_{K,0}$  is given by the following relation

$$N_{K,0} = \left[ 15\pi \left( \frac{l}{b_K} \right)^3 \beta \exp \left( \frac{\Delta E_a}{k_B T} \right) \right]^{1/(3\nu+1)} \quad (5-9)$$

Here,  $l$ ,  $b_K$  and  $\Delta E_a$  are respectively bond length, Kuhn bond length, and activation energy of bond rotation.  $\beta$  is a dimensionless prefactor that can be estimated from the shape of a typical rotational potential and  $\beta \sim 25$  for this case. The factor  $3\nu + 1$  ranges from 2.5 for  $\Theta$  conditions to 2.8 for good solvents. Since, in bulk state, the Kuhn segment size is comparable to the Rouse segment size,  $N_{K,0}$  can be determined as the Rouse segment size at each concentration in solution. He demonstrated that eq. (5-9) is consistent with the experimental result of  $N_{K,0} (\approx 5)$  for polystyrene in dilute solution. Very roughly speaking, eq. (5-9) indicates that  $N_{K,0}$  is inversely proportional to Kuhn segment length,  $b_K$  or more simply  $N_{K,0} \sim 40 (M_0/M_{s,\text{bulk}})$ .  $M_0/M_{s,\text{bulk}}$  for PEL is 1/13 and therefore eq. (5-9) predicts  $N_{K,0} \sim 3.0$ . The ratio  $M_s/M_{s,\text{bulk}} \sim N_{K,0} \sim 4$  is in good agreement, indicating that eq. (5-9) is applicable to PEL/IL systems.

Figure 5–7 displays the concentration dependence of the molar mass of Rouse segment. For the case of PS solutions,<sup>19</sup> its dependence was described by a following simple exponential function.

$$M_s = A + B \exp(-c/c_c) \quad (5-10)$$

Here,  $A$  and  $B$  are constants depending on polymer species, and  $c_c$  is characteristic concentration. Using this equation, the data for PEL/IL systems were fitted and the following parameters were obtained:  $A = 5.4 \times 10^3$  g/mol,  $B = 2.3 \times 10^4$  g/mol,  $c_c = 0.18$  g cm<sup>-3</sup> for TFSI–1 and  $A = 2.7 \times 10^3$  g/mol,  $B = 1.3 \times 10^4$  g/mol,  $c_c = 0.18$  g cm<sup>-3</sup> for BF<sub>4</sub>–1. There seems to be a transition around  $c \sim 0.3$  gcm<sup>-3</sup>, similar to the case of PS solutions reported by Inoue et al.<sup>19</sup> This threshold is close to  $c^{**}$ , which is the threshold concentration between semi-dilute and concentration regime.

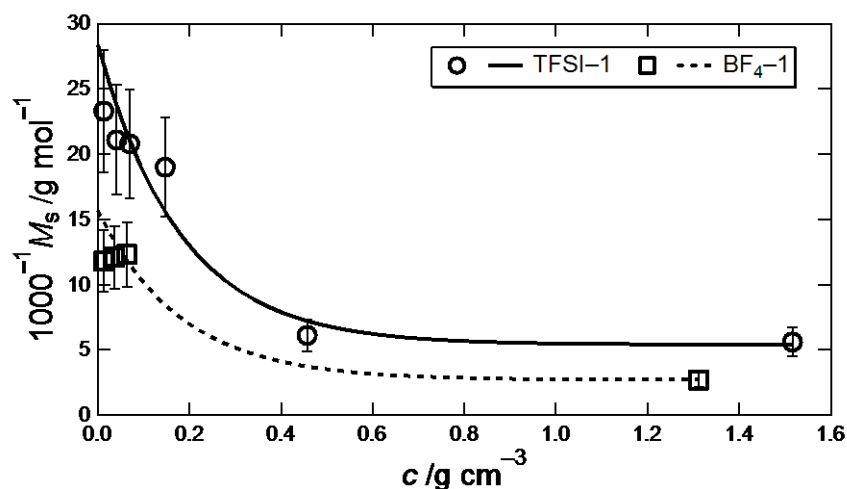


Figure 5–7. Concentration dependence of the Rouse segment size of PEL/ionic liquid systems.

### 5–3–7 Local Motion of a Chain in Solution

In this section, I will discuss the  $G'_{\text{local}}$  of polymer solutions. We start from the results for polystyrene, PS, for which local motions are not clearly observed. Figure 5–8 shows the

composite curves of the storage modulus  $G'$ , the storage modulus of polymeric modes,  $G_P'$ , and the real part of shear strain-optical coefficient of polymer contribution,  $K_P'$ , for PS-1.  $G_P'$  and  $K_P'$  were extracted by the subtraction of solvent contribution following the same manner as explained in section 5-3-4. The reference temperature is  $-30^\circ\text{C}$ . The limiting values of  $G_P'$  and  $K_P' / C_P$  at high frequencies agree with each other, indicating that contribution of  $G'_{\text{local}}$  is negligibly small in the case of polystyrene solution.

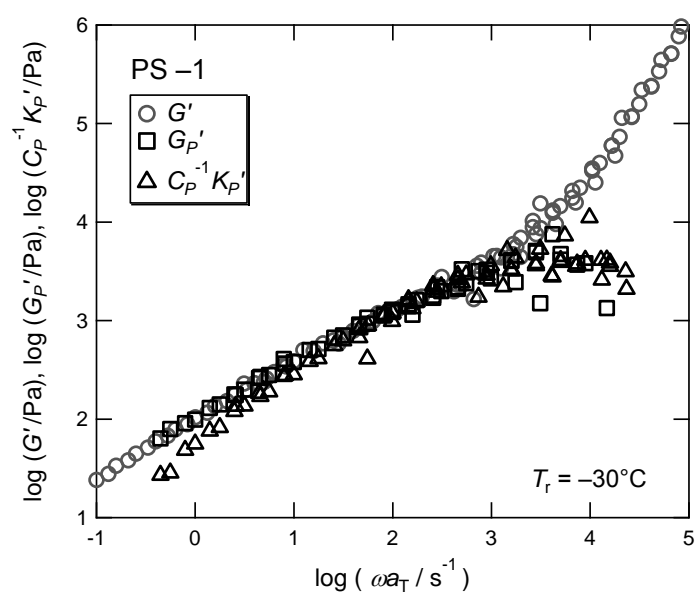


Figure 5-8. Frequency dependence of  $G'$  (circle) and the main chain orientation term  $G_P'$  (square) or  $C_P^{-1}K_P'$  (triangle) for PS-1.

$G_{\text{local}}^*$  can be estimated by solving the simultaneous equations (5-2) and (5-5). The values of  $C_{\text{local}}$  is summarized in Table 5-1. The results are shown in Figure 5-9. The intensity of  $G_{\text{local}}^*$  is not large but it becomes dominant at high frequencies.

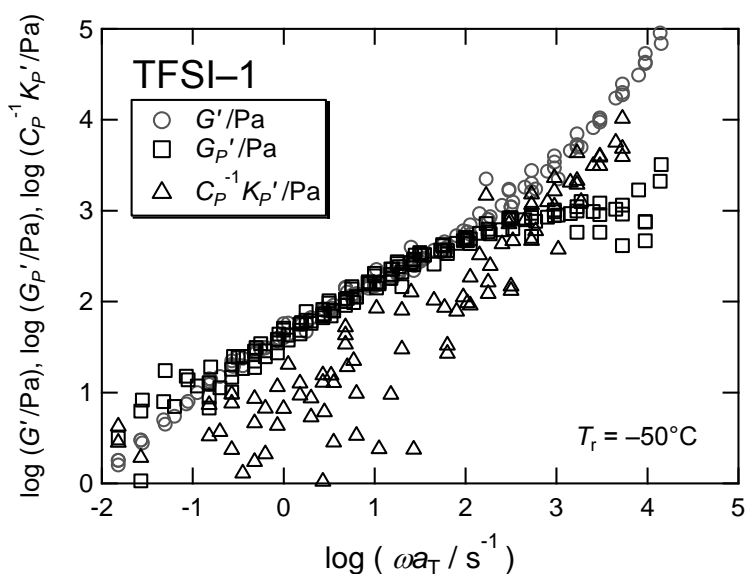


Figure 5–9. Separation of storage modulus into component functions.

### 5–3–8 Estimation of $G_{local}^*$ and Its Molecular Origin

The stress-optical coefficient for the local component can be a measure to assign the origin of stress. We note that the value of  $C_{local}$  is close to the stress-optical ratio for OmimTFSI,  $C_{OmimTFSI} = 5.9 \times 10^{-10} \text{ Pa}^{-1}$  at  $-70^\circ\text{C}$ . Here,  $C_{OmimTFSI}$  was estimated from the limiting value of  $K''/G''$  although the SOR did not hold strictly for OmimTFSI. The similar  $C_{local}$  value suggests that the local component might be related to the reorientation process of ions. Moreover, in Chapter 2, PC<sub>4</sub>-TFSI in bulk state showed the relaxation process corresponding to local motion of a polymer chain described by the DTO model,<sup>21</sup> in which cooperative torsional motions of structural units are considered. The value of the stress-optical coefficient for that local motion is  $2.3 \times 10^{-10}$ , and has the same order.

Figure 5–10 shows the frequency dependence of  $G_{local}'$  at different concentrations for PC<sub>4</sub>-TFSI/OmimTFSI and PC<sub>4</sub>-BF<sub>4</sub>/BmimBF<sub>4</sub> systems. Here the spectra for TFSI–3, TFSI–5, BF<sub>4</sub>–3, and BF<sub>4</sub>–5 were shifted toward high frequencies in order to compare them in the same viscous media, where the flow region of  $G''$  for solvent component of each system fall in the

same line. Intensities of local component increase with increasing polymer concentration, suggesting that local mode is related to polymer motions. Furthermore, the frequency dependence of  $G_{\text{local}}'$  shows the mode distribution. From such a discussion, as is the case of PC<sub>4</sub>-TFSI in bulk state, the relaxation mechanism of the L mode was described by the DTO model.

$$G'(\omega) = G_{\infty} \sum_p \frac{\omega^2 \tau_{\text{DTO}}^2 p^{-2}}{1 + \omega^2 \tau_{\text{DTO}}^2 p^{-2}} \quad (5-11)$$

Here,  $\tau_{\text{DTO}}$  is the characteristic time of the DTO model and listed in Table 5–3. The frequency dependence of  $G^*$  by the DTO model is similar to that of the Rouse model. For the case of linear array of the damped torsional oscillator arrays, the interchain interaction between polymer chains is ignored and the dynamics are governed by the connectivity of the chain. Considering the characteristic concentration  $c_c$  discussed before, the polymer-solvent interaction can be still dominant, and hence these assumptions are quite natural.

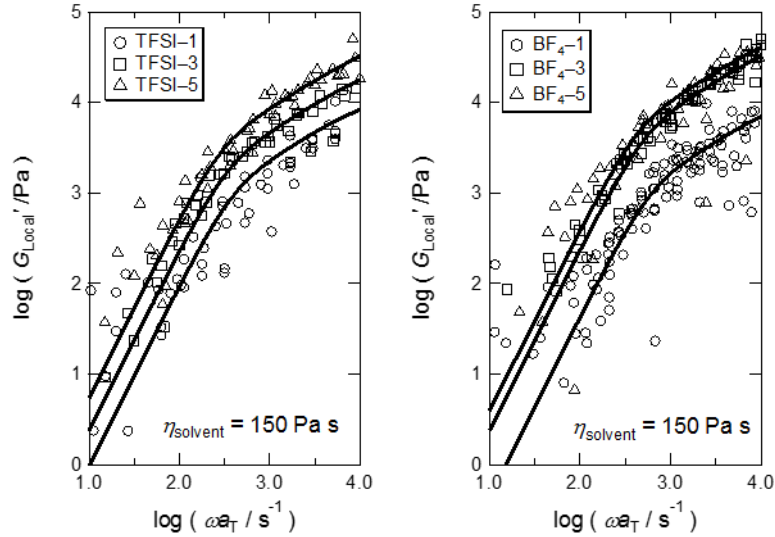


Figure 5–10. Frequency dependence of  $G'_{\text{local}}$  at different concentrations. Solid curves represent the fitting result with the DTO model.

In Figure 5–10, fitting curves written by the DTO model were depicted. The obtained  $\tau_{\text{DTOS}}$  were listed in Table 3. In fitting procedure, we set the number of units in the DTO model as 20 for all systems. If we take the repeating unit as structure unit, the motional unit size of the local mode is estimated from the  $G_{\infty}$  in the DTO model which is equal to  $cRT/M_{\text{local}}$  by taking the ratio of  $M_{\text{local}}/M_0$ . Here,  $M_0$  is molar mass of a repeating unit. The results are  $M_{\text{local}}/M_0$  is  $M=28$  for TFSI–1,  $M=46$  for TFSI–3,  $M=48$  for TFSI–5,  $M=46$  for BF<sub>4</sub>–1,  $M=34$  for BF<sub>4</sub>–3, and  $M=50$  for BF<sub>4</sub>–5. These numbers are comparable to the Rouse segment size ( $M_s/M_0=48$  for TFSI systems,  $M_s/M_0=51$  for BF<sub>4</sub> systems). Therefore, the L mode in present study could be attributed to the local motion of polymer chains. The delay of relaxation times for the higher polymer concentration may be caused by the increase of polymer-polymer interactions.

From several theoretical treatments,<sup>22</sup> viscoelastic properties of dilute solutions are predicted to have four contributions: global and local polymer motions, the Einsteinian contribution and the solvating environment. However, in case of dilute solutions of general amorphous polymers such as polystyrene, the latter three parts can be ignored, and hence the

frequency dependence of  $G^*$  can be well expressed by the eq. (5-1). In present study, the local motion of polymer chains could be observed even for a dilute case.

Figure 5-11 shows the  $M_0$  dependence of  $\tau_{\text{local}}$  and the fastest relaxation time  $\tau_{\text{RZ, fast}}$  of the polymeric Rouse mode for TFSI-1, BF<sub>4</sub>-1, Cl-1, and PS-1. The  $\tau_{\text{RZ, fast}}$  is defined as the reciprocal of frequencies where the Rouse slope line of  $G'$  ( $\propto \omega^{1/2}$ ) for the polymeric mode reach the plateau modulus of polymeric mode at high frequencies. Here we compared the values in the same viscous media, where solvent viscosities is the same. Both of the relaxation times linearly increased with increasing the molecular weight of repeating units. Thus, we conclude that the observation of local modes in PEL/IL systems is explained by the time scale separation between motions of polymers and solvents. The threshold whether the local mode is observed or not may exist at around  $M_0=200 \text{ g mol}^{-1}$ . The slope difference could be caused by the different  $M_0$  dependence of the sizes for motion units.

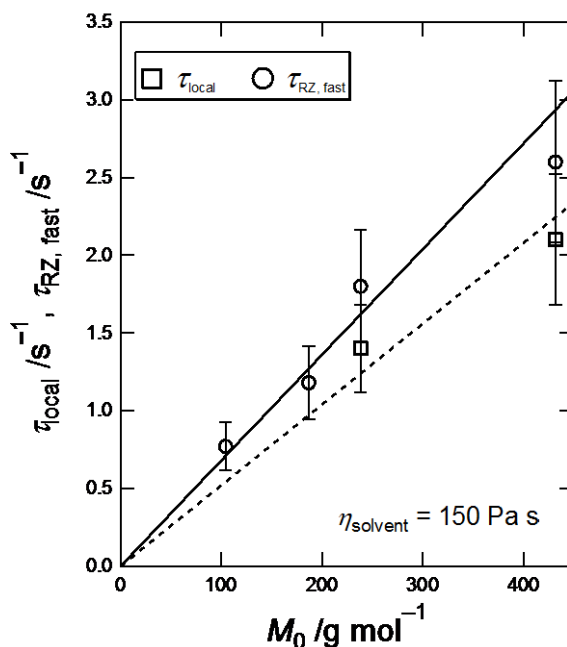


Figure 5-11. Dependence of  $\tau_{\text{local}}$  and  $\tau_{\text{RZ, fast}}$  on molecular weights of repeating units.

Table 5–2. Fitting parameters in eq. (5–3) and (5–4), and the characteristic times for the DTO model.

	$\alpha$	$\beta$	$\tau_{\text{DTO}} / 10^{-3} \text{ s}$
TFSI–1	1.65	2	1.7
TFSI–3	1.4	2	2.4
TFSI–5	1.4	2	2.9
BF <sub>4</sub> –1	1.65	2	1.4
BF <sub>4</sub> –3	1.65	2	1.6
BF <sub>4</sub> –5	1.3	2	1.9

### 5–3–9 MSOR Analysis for TFSI–50

Finally, in this section, we will discuss the linear viscoelastic behavior of TFSI–50. As mentioned before, we applied the three component MSOR described in eq. (2–13) and (2–14) with the aim of separating the component functions and obtain the stress optical coefficient for each component using the same procedure in Chapter 2.

Figure 5–12 displays the frequency dependence of the ratio  $K'/G'$  and  $K''/G''$  at  $T_r = -30^\circ\text{C}$ . At low frequencies, the frequency independent region is observed, indicating that the SOR holds valid. According to eq. (2–7), the  $C_R$  is estimated as  $-1.5 \times 10^{-8} \text{ Pa}^{-1}$ , which is comparable to that for PC<sub>4</sub>-TFSI in bulk state. Moreover, according to eq. (2–10), we determined  $C_G = 6.2 \times 10^{-10} \text{ Pa}^{-1}$ , which shows the same order as that for PC<sub>4</sub>-TFSI in bulk state. In the intermediate frequency region from  $\omega a_T = 10 \text{ s}^{-1}$  to  $\omega a_T = 10^4 \text{ s}^{-1}$ , the other frequency independent region is observed. Later on, we found that the value of  $K''/G''$  in this region is identical to the value of  $C_L$ .

Figure 5–13 shows the frequency dependence of  $(K^*(\omega) - C_L G^*(\omega))/(C_R - C_L)$  and  $(K^*(\omega) - C_R G^*(\omega))/(C_L - C_R)$  calculated using eq. (2–15) and eq. (2–16). Here, we assumed that the component function of the R mode agree with that for PC<sub>4</sub>-TFSI in bulk state. The vertically shift factor was estimated as 0.2. This value is reasonable because the value of  $c_{\text{TFSI-50}}/\rho_{\text{PC}_4\text{-TFSI}}$  is 0.3. The stress-optical coefficient for the L component for TFSI–50 is  $C_L = 1.2 \times 10^{-10} \text{ Pa}^{-1}$ , indicating that the L component is local motions of PC<sub>4</sub>-TFSI because the value is comparable to that for the Local motion of PC<sub>4</sub>-TFSI. Then, we determined the component function of  $G_G^*$  by the subtraction of  $G_R^*$  from  $(K^*(\omega) - C_L G^*(\omega))/(C_R - C_L)$ . By using determined  $G_R^*$ ,  $G_G^*$ ,  $C_R$ ,  $C_L$ , and  $C_G$ , we finally determined  $G_L^*$  through the eq. (2–16). Overall, as shown in Figure 5–14, we obtained the component functions where the relaxation time scale between polymers and solvents is separated. This time scale separation could be explained by the self-concentration model proposed by Lodge and McLeich.<sup>14</sup> In their model, polymers having large molar mass of repeating units are strongly self-concentrated.

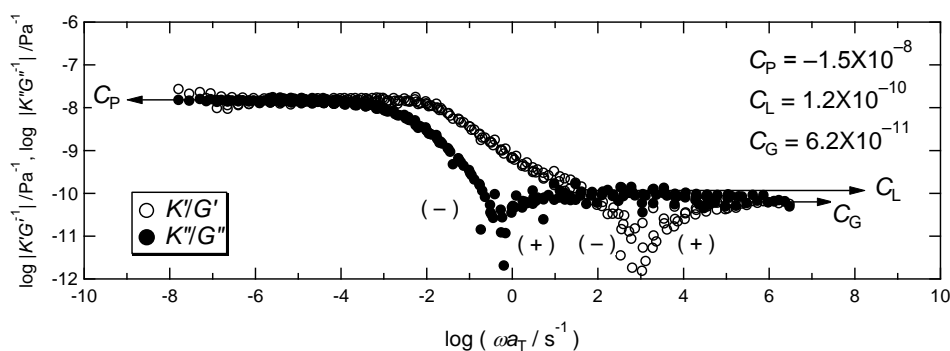


Figure 5–12. Frequency dependence of  $K'/G'$  and  $K''/G''$  for TFSI–50.

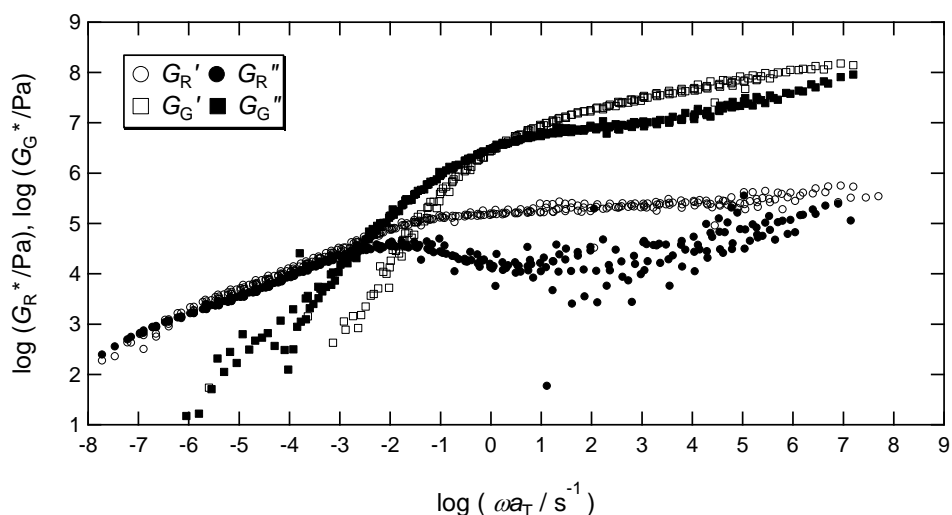


Figure 5–13. Component functions for TFSI–50 determined by two components MSOR.

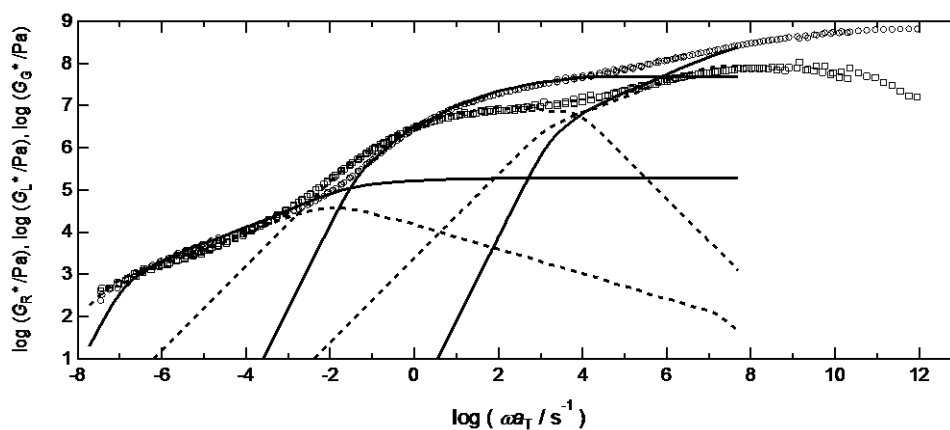


Figure 5–14. Three component functions determined by MSOR for TFSI–50.

## 5–4 Conclusion

We have conducted rheo-optical measurement on PC<sub>4</sub>-TFSI/OmimTFSI, PC<sub>4</sub>-BF<sub>4</sub>/BmimBF<sub>4</sub>, and PC<sub>4</sub>-Cl/BmimCl solutions to clarify the effect of the electrostatic interaction on viscoelastic properties, particularly the Rouse segment size and its concentration dependence. In dilute regime, the Rouse segment size is about five times as large as that in bulk state, similarly to the case of non-ionic polymer solutions such as PS in TCP. Furthermore, the concentration dependence of the Rouse segment size was similar to that for PS solutions. The

effect of the electrostatic interaction for the Rouse-Zimm modes was not observed in these system.

Applying the modified stress-optical rule to experimental data, we successfully estimated the local motion of polymer chains even for dilute solutions. Appearance of the local motion of polymer chains could be attributed to the relaxation time scale separation between polymers and solvents.

## 5-5 References

- (1) Boris, D. C.; Colby, R. H. *Macromolecules* **1998**, 31, 5746-5755.
- (2) Dobrynin, A. V.; Colby, R. H.; Rubinstein, M. *Macromolecules* **1995**, 28, 1859-1871.
- (3) Noda, I.; Takahashi, Y. *Berichte Der Bunsen-Gesellschaft-Physical Chemistry Chemical Physics* **1996**, 100, 696-702.
- (4) Rubinstein, M.; Colby, R. H.; Dobrynin, A. V. *Phys. Rev. Lett.* **1994**, 73, 2776-2779.
- (5) Takahashi, Y.; Hase, H.; Yamaguchi, M.; Noda, I. *J. Non-Cryst. Solids* **1994**, 172, 911-916.
- (6) Takahashi, Y.; Lio, S. J.; Matsumoto, N.; Noda, I. *Polym. Int.* **1996**, 40, 269-273.
- (7) Yamaguchi, M.; Wakutsu, M.; Takahashi, Y.; Noda, I. *Macromolecules* **1992**, 25, 470-474.
- (8) Yamaguchi, M.; Wakutsu, M.; Takahashi, Y.; Noda, I. *Macromolecules* **1992**, 25, 475-478.
- (9) Amelar, S.; Eastman, C. E.; Morris, R. L.; Smeltzly, M. A.; Lodge, T. P.; Vonmeerwall, E. D. *Macromolecules* **1991**, 24, 3505-3516.
- (10) Maeda, A.; Inoue, T.; Sato, T. *Macromolecules* **2013**, 46, 7118-7124.
- (11) Hutcheson, S. A.; McKenna, G. B. *J. Chem. Phys.* **2008**, 129.
- (12) Schroter, K.; Hutcheson, S. A.; Shi, X.; Mandanici, A.; McKenna, G. B. *J. Chem. Phys.* **2006**, 125.
- (13) Dzyuba, S. V.; Bartsch, R. A. *Chemphyschem* **2002**, 3, 161-+.
- (14) Lodge, T. P.; McLeish, T. C. B. *Macromolecules* **2000**, 33, 5278-5284.
- (15) Riande, E.; Markovitz, H.; Plazek, D. J.; Raghupathi, N. *J Polym Sci Pol Sym* **1975**, 405-430.
- (16) Inoue, T.; Osaki, K. *Macromolecules* **1996**, 29, 1595-1599.
- (17) Peterson, S. C.; Echeverria, I.; Hahn, S. F.; Strand, D. A.; Schrag, J. L. *J Polym Sci Pol Phys* **2001**, 39, 2860-2873.
- (18) Treloar, L. R. G. *Clarendon: Oxford* **1958**.

- (19) Inoue, T.; Uematsu, T.; Osaki, K. *Macromolecules* **2002**, 35, 820-826.
- (20) Larson, R. G. *Macromolecules* **2004**, 37, 5110-5114.
- (21) Tobolsky, A. V.; Aklonis, J. J. *J. Phys. Chem.* **1964**, 68, 1970-&.
- (22) Yoshizaki, T.; Yamakawa, H. *J. Chem. Phys.* **1988**, 88, 1313-1325.

---

## CHAPTER 6

### Summary

---

In this dissertation thesis, I developed the methodology to control the mechanical properties and the ionic conductivities of polymerized ionic liquids (PILs). Figure 6–1 shows the relationship between chemical structure, ionic conductivity and mechanical properties of poly(1-alkyl-3-vinylimidazolium)-based ionic liquids. I focused on the volume ratio,  $V_r$  ( $=V_a/V_c$ ), of an anion,  $V_a$ , and a cation,  $V_c$ . For the use of smaller counter anions, the high ionic conductivity was achieved while the temperature for hot press molding was increased due to the increase of  $T_g$ . For the use of relatively larger counter anions, on the other hand, the processability was improved due to the decrease of  $T_g$  while the ionic conductivity decreased. The relaxation process of polymerized ionic liquids was affected by the enhancement of intra-chain cooperativity with increasing ionic sizes of counterions. In particular, for the cases of PILs having ionic sizes of counterions larger than those of polyions, the segmental motion of polymers was highly restricted. The unique ordered structure like liquid crystals was also observed.

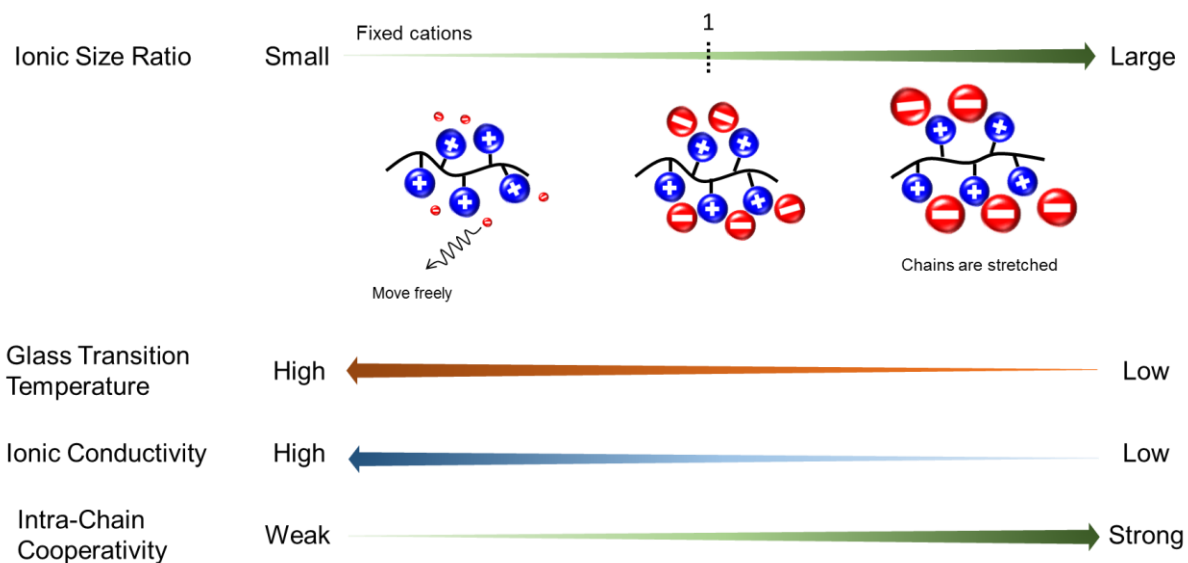


Figure 6–1. Summary of the relationship between chemical structure, ionic conductivity, and mechanical properties of PILs.

In Chapter 2, the linear viscoelastic responses (LVE) were investigated using five poly(1-butyl-3-vinylimidazolium)-based ionic liquids having various counter anions. The volume ratio,  $V_r$ , of an anion to a cation (monomer unit) were varied: PC<sub>4</sub>VIBF<sub>4</sub> ( $V_r = 0.32$ ), PC<sub>4</sub>VITfO ( $V_r = 0.55$ ), PC<sub>4</sub>VITFSI ( $V_r = 1$ ), PC<sub>4</sub>VICPFSI ( $V_r = 1.07$ ), PC<sub>4</sub>VINfO ( $V_r = 1.07$ ). The glass transition temperature tended to decrease with increasing the volume ratio,  $V_r$ . Moreover, the LVE spectra in the glass-to-rubber zone became broad with increasing the volume ratio,  $V_r$ . In order to analyze the LVE spectra in more detail, I applied the simultaneous measurements of the stress and birefringence in which the complex modulus,  $G^* = G' + iG''$ , and the complex strain-optical coefficient,  $K^* = K' + iK''$  were obtained. Based on the modified stress-optical rule analysis, the LVE spectra were successfully separated into two or three components, namely the glassy mode, the sub-Rouse mode, and the segmental reorientation mode. For PC<sub>4</sub>VIBF<sub>4</sub> and PC<sub>4</sub>VITfO with relatively low  $V_r$ , the glassy mode and the segmental reorientation mode were observed, similarly to the case of ordinary amorphous polymers. For PC<sub>4</sub>VITFSI, PC<sub>4</sub>VICPFSI, and PC<sub>4</sub>VINfO for which  $V_r$  is close to unity, on the other hand, the

sub-Rouse mode was observed between the glassy mode and the segmental reorientation mode. The sub-Rouse mode is often observed in polymer solutions where intra-chain interaction is dominant for local motions. The intra-chain cooperativity became strong with increasing the volume ratio,  $V_r$ .

In Chapter 3, the morphology and linear viscoelastic behavior were investigated using two poly(1-butyl-3-vinylimidazolium)-based ionic liquids with  $V_r$  larger than unity. The unique ordered structure was formed in the samples prepared by the hot press molding. Considering that the intra-chain cooperativity becomes strong with increasing the  $V_r$ , the polymer chains could be rigid like semi-flexible polymers. In such a discussion, the rod-like segments can form arrays. However, the film prepared by the solvent cast method did not show such the ordered structures. This is opposite to the prediction for ordinary semi-flexible polymers in which liquid crystal structures are formed in melt. The rigid chains tends to orient into the same direction to achieve a thermodynamically stable state. Therefore, further investigations are required to clarify the precise molecular mechanism to form the arrays. As for the characteristics of ordered structures, the strong restriction of segmental motion held its array over the glass transition temperature. The structural changes such as the structural growth were not observed. The mechanical strength was highly enhanced by four decades irrespective of the presence of ordered structures. In contrast, the change in magnitude of ionic conductivity was less than two decades. In many cases of solid-state single ion conductive polyelectrolytes, ionic conductivities and mechanical strengths are in trade-off relationship since ion motions are strongly correlate with the motions of polymer chains. In this context, our result provides one of the strategies to enhance mechanical properties of polymerized ionic liquids with keeping ionic conductivity high.

In Chapter 4, the relationship between morphology, ionic conductivity, and chemical structure of PILs was investigated using the linear viscoelastic measurements, dielectric

relaxation spectroscopy and X-ray scattering. A series of poly(1-alkyl-3-vinylimidazolium)-based ionic liquids was used in order to clarify the effects of alkyl chain lengths and ionic sizes of counter anions on ionic conductivities of PILs. The change in magnitude of dc ionic conductivity at the glass transition temperature was less than one order by changing the alkyl chain lengths, whereas the change was four orders by changing the counter anion species. Based on the electrode polarization analysis, I found that the mobility of conducting ions decreased with increasing the ionic sizes of counter anions. Smaller counter anions can move fast through the hopping mechanism in polymer matrix. Accordingly, the degree of decoupling between ion conduction and structural relaxation became higher with decreasing the ionic sizes of counter anions.

In Chapter 5, viscoelasticity and birefringence under oscillatory shear flow were measured for the solutions of polymerized ionic liquids in ionic liquids over a wide range of frequency from the flow to the glassy zone in order to clarify effects of the electrostatic interaction on the Rouse segment size and its concentration dependence. In dilute regime, the Rouse segment size is about five times as large as that in bulk state, similarly to the case of non-ionic polymers solutions such as PS in TCP. Furthermore, the concentration dependence of the Rouse segment size was similar to that for PS solutions. The effect of the electrostatic interaction for the Rouse-Zimm modes was not observed in these system. Applying the modified stress-optical rule to the experimental data, we successfully estimated the local motion of polymer chains even for dilute solutions. Appearance of the local motion of polymer chains could be attributed to the wide separation in their relaxation times between polymers and solvents.

### List of Publications:

1. “Dynamic Viscoelastic and Birefringence of Poly(Ionic Liquids) in the Vicinity of Glass Transition Zone”  
T. Inoue, **A. Matsumoto**, and K. Nakamura *Macromolecules* **2013**, 46, 6104 – 6109
2. “Detailed Analysis of Sub-Rouse Mode Observed in Polymerized Ionic Liquids Systems with Rheo-Optical Method”  
**A. Matsumoto** and T. Inoue *Nihon Reoroji Gakkaishi* **2014**, 42, 227 – 233
3. “Polymerized Ionic Liquids: Correlation of Ionic Conductivity with Nanoscale Morphology”  
C. Iacob, **A. Matsumoto**, M. Brennan, H. Liu, S. Paddison, O. Urakawa, T. Inoue, J. Sangoro, and J. Runt submitted to *ACS Macro Letters*
4. “Viscoelastic Properties and Local Dynamics of Polyelectrolyte/Ionic Liquid Solutions”  
**A. Matsumoto** and T. Inoue to be submitted
5. “Counter Ion-Induced Ordered Structure of a Polymerized Ionic Liquid in Bulk”  
**A. Matsumoto**, C. Iacob, O. Urakawa, J. Runt, and T. Inoue to be submitted
6. “Counterion Transporting Mechanism in Polymerized Ionic Liquids with Different Counter Anions and Side Chain Lengths”  
**A. Matsumoto**, C. Iacob, O. Urakawa, T. Inoue, and J. Runt to be submitted

### Related Paper

7. “Re-Examination of Terminal Relaxation Behavior for High Molecular Weight Ring Polystyrene Melts”  
Y. Doi, **A. Matsumoto**, T. Inoue, T. Iwamoto, A. Takano, Y. Matsushita, Y. Takahashi, and H. Watanabe submitted to *Macromolecules*